

PhD. 30186

# Spatial dynamics of *in vitro* viral infection

Tom J. Howat  
Trinity College



A dissertation submitted for the degree of Doctor of Philosophy at the  
University of Cambridge

August 2006

# Preface

This dissertation is the result of my own work and includes nothing which is the outcome of work done in collaboration except where specifically indicated in the text. No part of this dissertation has been submitted to any other university in application for a higher degree.

A handwritten signature in black ink, appearing to read 'Tom Howat', with a horizontal line underneath.

Tom Howat  
Trinity College  
August 2006

*To my parents*

(how *nice* you for)

# Acknowledgements

I've built up quite a collection of supervisors over the course of my research, and my greatest thanks goes to them: Bryan Grenfell, Julia Gog, and Paul Digard. Bryan, for always helping me to see the bigger picture; Julia, for drawing me into mathematical biology in the first place<sup>1</sup> (together with Jon Dawes and a Trinity College summer studentship); and Paul, for teaching an old mathmo new tricks. It's been a joy to work with you all.

The Gog née Grenfell group has been through a few changes since I first set out in September 2003, but to them all I owe my gratitude, for their support, encouragement, and endless supply of fun<sup>2</sup>: Andrew Conlan, Colin Russell, Ken Eames, Ellen Brooks Pollock, Jenny Crossan, Natalia Mantilla-Beniers, Nick Savill, Derek Smith, Terry Jones, Marc Baguelin, Olivier Restif, Sam Brown, Andy Fenton, Andrew Park, Stephen Cornell, Roberto Saenz, Alicia Murcia, and, of course, Spiderman. In this vein I feel compelled to mention our trusty piscine pals: Dr Schmookler, Svlad Cjelli, Dr Obichuckwura of Nigeria<sup>3</sup>, Prince Ludwig the Indestructible, Blinky, Dr Frank, Father Jack, Father Ted, and Father Dougal McGuire (deceased) – thanks guys, you were always there for me.

I have heartfelt thanks and respect (for their limitless patience) for Paul Digard and

---

<sup>1</sup>Despite my best efforts as an undergraduate, forces conspired to draw me at least part way back toward my family's traditional calling, medicine. No one, least of all me, would have anticipated that, after the Maths tripos, I'd end up studying the same things as my father [99].

<sup>2</sup>Rocketeering, squadmintablis, and sailing *Felicity* on a moonlit Cam being just three of the many highlights.

<sup>3</sup>Value 3 MILLION DOLLARS.

his lab: Sarah Noton, Debra Elton, Romy Dalton, Liz Medcalf, Ed Hutchison, Maria Amorim, and Eva Kreysa – how you draped a white lab coat over a mathematician and taught him to perform experiments without impaling himself on a Gilson tip, I'll never be able fathom.

I'd like to thank everyone Department of Zoology for looking after me during my research, and making it a great place to work. In particular Linda Wheatley for simply knowing *everything*, and Bill Amos (and Gill, Shelley, and Fraser) for relaxing breaks from college life.

Throughout Cambridge and beyond: I must thank Janet Daly at the Animal Health Trust and James Wood at the Vet School for readily answering all my equine questions; François Balloux in Genetics for useful discussion; John Rallison in DAMTP for invaluable insight on fluid flows; and Pietro Cicuta in the Cavendish, for introducing me to the complexities of surface tension and letting me loose on his pendant drop tensiometer. Further afield, my thanks also to Peter O'Hare and Cristina Barreca at the Marie Curie Research Institute for their comprehensive explanations of all things HSV. I'd like to give special thanks to John Rudge and Dominic Vella for their generous help with numerous fluid dynamic problems.

Across the Atlantic, I'd like to thank Cecile Viboud and Ellis McKenzie for hosting my visits to NIH, and the Penn State crowd – Bryan Grenfell and Catherine Williams, Eleca Dunham, Pete Hudson, Eddie Holmes, Sarah Perkins, Katia Koelle, Jamie Lloyd-Smith, Igor Volkov, Andy Wilson, Nita Bharti, and Matt Ferrari – for making my trips to the geographic centre of Pennsylvania memorable and enjoyable.

Thanks to my funding body, the Medical Research Council; and a special thanks to my college, Trinity, my home for seven years.

Lastly, to my parents, my sister, and to Andy: for helping all along the way, providing support and encouragement, and for generally being fantastic – thank you all.

This document was typeset using L<sup>A</sup>T<sub>E</sub>X2<sub>ε</sub>. Models were developed in Microsoft Visual

C++ .NET 2003. Graphs were plotted in Systat SigmaPlot 9.0. Diagrams were drawn in CorelDRAW 12. Bitmap manipulation was performed in Corel PHOTO-PAINT 12.

# Summary

Innate immunity is crucial in the early stages of resistance to novel viral infection. The family of cytokines known as the *interferons* (IFNs) form an essential component of this system: they are responsible for signalling that an infection is underway and for promoting an antiviral response in susceptible cells. Despite the importance of the IFNs in viral infections, many questions about the dynamics of IFN production and activity remain unanswered.

Addressing these questions forms the first half of this thesis. It begins with an introduction to innate immunity, and a review of existing research. Focus then falls upon a simple experimental system: the *in vitro* infection of cell monolayers by Herpes simplex virus and the resulting IFN response. A stochastic spatial model of viral infection and consequent IFN production and activity is constructed. Using this model, simulations of infections under varying initial conditions suggest the existence of critical doses, at which the qualitative behaviour of infection changes. Implications for IFN activity in *in vivo* infections are highlighted, as well as potential applications of the model, particularly in within-host modelling.

The data used to parameterize this model come from widely used experiments called plaque assays: infection spreads in cell monolayers *in vitro*, leaving regions of dead cells, known as *plaques*. The second half of the thesis considers the dynamics of plaque formation and, in particular, the phenomenon of *cometing*, where in plaques unexpectedly streak across monolayers forming patterns that resemble comets. Several theories behind comet formation have been proposed in the literature, though the underlying mechanism is not understood. A detailed investigation is carried out

here: previously voiced hypotheses are tested, and a method for controlling comet formation is developed; cometing is found to be a purely fluid dynamic phenomenon.

The thesis concludes with an overview of the results obtained, and a discussion of potential applications and future directions for research.

# Publications

**Modelling dynamics of the Type I Interferon response to in vitro viral infection.**

The work detailed in chapters 2–4 was published in *Journal of the Royal Society Interface* [100].

# Contents

<b>Preface</b>	<b>i</b>
<b>Acknowledgements</b>	<b>iii</b>
<b>Summary</b>	<b>vi</b>
<b>Publications</b>	<b>viii</b>
<b>Contents</b>	<b>ix</b>
<b>List of Figures</b>	<b>xiii</b>
<b>List of Tables</b>	<b>xv</b>
<b>1 Introduction</b>	<b>1</b>
1.1 Infectious disease . . . . .	1
1.1.1 The impact of disease throughout history . . . . .	1
1.1.2 Infectious disease research . . . . .	2
1.2 Immunity . . . . .	3
1.2.1 The innate immune system . . . . .	4
1.2.2 The interferons . . . . .	6
1.3 History of immune modelling . . . . .	8
1.3.1 Viral infections <i>in vivo</i> . . . . .	8
1.3.2 Cytokine signalling networks . . . . .	10
1.3.3 Spatial modelling . . . . .	10
1.3.4 Why study immune dynamics? . . . . .	11
1.4 Spatial disease spread . . . . .	12
1.4.1 Plaques and plaque assays . . . . .	13
1.4.2 Plaque assays as a window on IFN dynamics . . . . .	14
1.5 Prospectus for the thesis . . . . .	15

<b>2</b>	<b>Plaque dynamics of in vitro HSV infection</b>	<b>17</b>
2.1	Introduction . . . . .	17
2.1.1	Herpes simplex virus . . . . .	17
2.1.2	The experiments . . . . .	19
2.2	Data gathering and analysis . . . . .	23
2.2.1	Data analysis . . . . .	24
2.2.2	Data analysis II . . . . .	27
2.2.3	Summary . . . . .	31
<b>3</b>	<b>A stochastic model of in vitro HSV spread</b>	<b>32</b>
3.1	Introduction . . . . .	32
3.1.1	Rationale for a stochastic spatial model . . . . .	32
3.2	Model design . . . . .	33
3.2.1	Model schematics . . . . .	33
3.2.2	The virtual monolayer . . . . .	36
3.2.3	The time step . . . . .	38
3.2.4	Diffusion and interferon . . . . .	38
3.2.5	Scattering of virions on cytolysis . . . . .	39
3.2.6	Binding of virions and the action of IFN . . . . .	39
3.2.7	Underlying algorithms and equations . . . . .	40
3.2.8	Random numbers and the binomial distribution . . . . .	41
3.2.9	Implementation . . . . .	42
3.3	Parameterization . . . . .	42
3.3.1	Parameters . . . . .	42
3.3.2	Parameter fitting . . . . .	43
3.3.3	Fitting to the Vero data set . . . . .	43
3.3.4	Confidence intervals and regions . . . . .	44
3.3.5	Fitting to the MDBK data sets . . . . .	44
3.4	Discussion: quality of fit . . . . .	49
<b>4</b>	<b>Simulating virus-IFN-cell dynamics</b>	<b>50</b>
4.1	Introduction . . . . .	50
4.2	Results . . . . .	52
4.2.1	Total monolayer destruction . . . . .	52
4.2.2	Maximizing IFN- $\beta$ production . . . . .	55
4.2.3	Minimizing recovery time . . . . .	56
4.2.4	Priming of cells prior to infection . . . . .	58
4.3	Summary of qualitative plaque dynamics . . . . .	58
4.3.1	Recovery times and boundary lengths. . . . .	59
4.4	Scattering discs and boundary lengths . . . . .	62

4.5	Discussion and conclusions . . . . .	64
4.5.1	Behaviour of epithelial cell monolayers <i>in vivo</i> . . . . .	64
4.5.2	Priming cells <i>in vivo</i> . . . . .	65
4.5.3	Future work . . . . .	66
4.5.4	Understanding plaque assays . . . . .	68
<b>5</b>	<b>Comet formation in plaque assays of influenza</b>	<b>69</b>
5.1	Introduction . . . . .	69
5.1.1	Influenza . . . . .	70
5.1.2	Comets . . . . .	71
5.1.3	Comets and modelling . . . . .	72
5.1.4	Historical suggestions for comet aetiology . . . . .	72
5.1.5	Experimental materials and methods . . . . .	73
5.2	Properties of comets . . . . .	73
5.2.1	Direction and axisymmetry . . . . .	73
5.2.2	Extent of plaques . . . . .	74
5.2.3	Image analysis – circular plaques vs. comets . . . . .	76
5.3	Testing candidate mechanisms for comet formation . . . . .	80
5.3.1	Well base curvature . . . . .	80
5.3.2	Concentration gradients . . . . .	86
5.3.3	Environmental disturbance . . . . .	88
5.4	Conclusion . . . . .	91
<b>6</b>	<b>A fluid dynamic mechanism for comet formation</b>	<b>92</b>
6.1	Introduction . . . . .	92
6.1.1	Further evidence of radial flow . . . . .	93
6.1.2	Speed of the flow . . . . .	96
6.1.3	Assumptions, boundary conditions, and the flow profile . . . . .	96
6.1.4	Conclusions . . . . .	97
6.2	Investigating the flow . . . . .	97
6.2.1	Overlay depth . . . . .	97
6.2.2	Overlay viscosity . . . . .	98
6.2.3	Baffles . . . . .	101
6.2.4	Conclusion . . . . .	105
6.3	A mechanism for the flow . . . . .	105
6.3.1	Convection . . . . .	105
6.3.2	The Marangoni effect . . . . .	107
6.3.3	Varying surface tension . . . . .	109
6.3.4	Viscoelasticity in Langmuir monolayers . . . . .	113
6.3.5	Conclusions . . . . .	114

6.4	Possible gradients driving the flow . . . . .	115
6.4.1	Temperature gradients . . . . .	115
6.4.2	Surface tension gradients . . . . .	116
6.5	Discussion and conclusions . . . . .	118
6.5.1	Summary of experimental results . . . . .	118
6.5.2	Conclusion: the origin of comets . . . . .	119
6.5.3	Open questions . . . . .	119
6.5.4	Further experiments . . . . .	120
6.5.5	Implications for modelling . . . . .	121
6.5.6	Control of cometing . . . . .	122
<b>7</b>	<b>Discussion and conclusions</b>	<b>123</b>
7.1	Overview of thesis . . . . .	123
7.1.1	Motivation . . . . .	123
7.1.2	Experimental data . . . . .	124
7.1.3	Model development and simulation results . . . . .	124
7.1.4	Factors affecting plaque growth . . . . .	124
7.1.5	Comets: a fluid dynamic phenomenon . . . . .	125
7.2	General conclusions . . . . .	125
7.3	Limitations and future work . . . . .	126
7.3.1	Within-cell modelling . . . . .	127
7.3.2	The 'virtual' host . . . . .	128
<b>A</b>	<b>HSV data sets</b>	<b>130</b>
<b>B</b>	<b>Materials and methods for comet experiments</b>	<b>135</b>
B.1	Cells and viruses . . . . .	135
B.2	Plaque assays . . . . .	136
B.3	Other assays . . . . .	137
B.3.1	Infectious centres assays . . . . .	137
B.3.2	Supernatant assays . . . . .	137
B.3.3	Immunofluorescence assays . . . . .	137
B.3.4	Preparation of CMC . . . . .	138
B.3.5	Oswald viscometer . . . . .	138
	<b>Bibliography</b>	<b>140</b>

# List of Figures

1.1	Plaque assays as a window on IFN action. . . . .	14
2.1	Progression of HSV-1 infection in cell monolayers. . . . .	22
2.2	Data set from MDBK cells infected with 2500 pfu. . . . .	23
2.3	Selecting plaques for measurement. . . . .	24
2.4	Mean plaque area against time. . . . .	26
2.5	Image transformation technique for HSV data. . . . .	28
2.6	Counting of plaques in the MDBK 10 pfu plates. . . . .	29
2.7	Percentage plaque against time. . . . .	30
3.1	Progression of infection in the model. . . . .	34
3.2	Schematic of model execution. . . . .	35
3.3	Epithelial cells compared with a hexagonal lattice. . . . .	36
3.4	Connections and variables on the hexagonal lattice. . . . .	37
3.5	Parameter fitting to MDBK data sets. . . . .	46
3.6	Model fits to experimental data. . . . .	48
4.1	Graphical output from the model. . . . .	51
4.2	Model time series profiles. . . . .	53
4.3	Determining the critical dose $\nu_D$ . . . . .	54
4.4	Determining the critical dose $\nu_I$ . . . . .	55
4.5	Determining the critical dose $\nu_R$ . . . . .	57
4.6	Recovery time against boundary length. . . . .	61
4.7	Effective circumferences compared. . . . .	63
5.1	Circular plaques and comets. . . . .	71
5.2	Comets in a variety of dishes. . . . .	74
5.3	Microscopy of a comet. . . . .	75
5.4	Infectious centres and supernatant assay results. . . . .	76
5.5	Estimated titre from infectious centres and supernatant assays. . . . .	77
5.6	Image transformation technique for circular plaques vs. comets . . . . .	78

5.7	Image transformation results . . . . .	79
5.8	Variations in 6-well depth. . . . .	82
5.9	Tilting a 6-well cluster. . . . .	83
5.10	Tilted well base contours. . . . .	83
5.11	Results of tilting a 6-well during incubation. . . . .	84
5.12	Cover slips used to flatten well growth surfaces. . . . .	85
5.13	Pattern formation in bacterial colonies. . . . .	86
5.14	Axisymmetric standing waves. . . . .	89
5.15	Using a water bath to rule out environmental disturbance. . . . .	90
6.1	Comet tails. . . . .	93
6.2	Fluid dynamic mechanism for comet formation. . . . .	94
6.3	Mean plaque length against radial position. . . . .	95
6.4	Hypothetical comet-forming flow profile. . . . .	97
6.5	Results of varying overlay depth. . . . .	99
6.6	Hypothetical comet-forming flow profiles at different overlay depths. . . . .	100
6.7	Results of varying overlay viscosity. . . . .	102
6.8	Insertion of a baffle into the overlay. . . . .	103
6.9	Results of the baffle experiments. . . . .	104
6.10	Comparison: with and without baffle. . . . .	105
6.11	Comet formation in convective cells. . . . .	106
6.12	Convection currents caused by lateral heating. . . . .	107
6.13	Surface-tension driven flow. . . . .	108
6.14	Experimental setup for tensiometry. . . . .	110
6.15	Surface-tension measurements. . . . .	111
6.16	Mean plaque length against overlay surface tension. . . . .	112
6.17	The chemical structure of phosphatidylcholine. . . . .	113
A.1	Data set from Vero cells infected with 50 pfu. . . . .	131
A.2	Data set from MDBK cells infected with 10 pfu. . . . .	132
A.3	Data set from MDBK cells infected with 50 pfu. . . . .	133
A.4	Data set from MDBK cells infected with 500 pfu. . . . .	134
B.1	The Oswald viscometer. . . . .	139

## List of Tables

3.1	Model parameters and their estimates . . . . .	43
3.2	Results of parameterization to MDBK data sets. . . . .	46
4.1	Critical doses suggested by modelling results. . . . .	59
6.1	Parameters for surface tension gradient estimation. . . . .	116

## List of Tables

3.1	Model parameters and their estimates . . . . .	43
3.2	Results of parameterization to MDBK data sets. . . . .	46
4.1	Critical doses suggested by modelling results. . . . .	59
6.1	Parameters for surface tension gradient estimation. . . . .	116

# Chapter 1

## Introduction

### 1.1 Infectious disease

#### 1.1.1 The impact of disease throughout history

Throughout history, infectious disease has posed one of the greatest challenges to human survival. Documents from as far back as ancient Greece describe epidemics of smallpox, leprosy, and tuberculosis [203]: smallpox has since fallen to medical science, but tuberculosis causes increasing morbidity and mortality worldwide [54]. From the Black Death of the middle ages, through the great influenza pandemics of the last century, to the current threats posed by HIV and avian influenza, disease has evolved alongside our understanding of it and our capacity to contain it.

Whether the invading pathogen is a microparasite (for example, a virus or bacterium) or macroparasite (such as a helminth), it is the job of the host immune system to repel or destroy the invasion. The vertebrate immune system can be conceptually divided into two halves: arguably the better studied of these is the adaptive response, which mounts a slow-acting but highly specific defence against novel infections. Crucially, the adaptive immune system also attempts to 'remember' pathogens so that future infections by the same pathogen can be more quickly

overcome: vaccination works by stimulating the production of the immune cells and molecules which form this memory.

The other part of the immune system is the innate response: an immediate, non-specific defence against pathogen invasion. This thesis considers the early spatial dynamics of innate immune defence against viruses – a process which plays a pivotal role in combating novel viral infection.

### 1.1.2 Infectious disease research

Traditionally, research into infectious disease has been approached from a biological standpoint: microbiology and virology studying the pathogens themselves, immunology the immune system of the host, and epidemiology the patterns of infection incidence in the population. In the last century an increasing effort began to study these fields from a mathematical perspective as well. The interactions between pathogen and immune system, immune system and host, host and population, lead to dynamic processes at many scales – mathematical modelling provides useful tools and a framework to study these processes.

There is a long history of study of the dynamics of disease spread in a population. Daniel Bernoulli is often cited as being the founding father of mathematical biology, after publishing his study on the risk-benefit analysis of smallpox variolation<sup>1</sup> [26]. However, mathematical epidemiology as we understand it today arguably began with Hamer who in 1906 formulated a discrete-time mass-action model of measles epidemics in England [85]. Since then there has been an explosion in mathematical epidemiology (for example, the work of Anderson and May [5–8, 11, 12, 131]), both in measles [94] and in several other diseases. For example, influenza has been widely studied, from the multiple strain models of Andreasen *et al.* [13, 61], Gog and Swinton [79], and Dawes and Gog [46], to the strain evolution work of Gupta *et al.* [83], Lin *et al.* [124], Gog *et al.* [77, 78], and Boni *et al.* [35]. Influenza strain evolution has also been studied from a genetic standpoint, for example in the work

---

<sup>1</sup>That is, intentional exposure to smallpox – an early form of immunization.

of Daly *et al.* [45], Hay *et al.* [89], Plotkin *et al.* [172], and Smith *et al.* [187]. The population-level spread of malaria [84, 88, 116, 133, 135, 189], HIV [9, 10, 28, 63, 104], and rabies [4, 47, 110, 151, 188], as well as several other diseases, have also been the subject of mathematical modelling.

In the 1980s, a new pathogen, the human immunodeficiency virus, came to light. The ensuing pandemic impelled researchers to focus mathematical models on the immunodynamics of infection – the ‘battle’ between an invading pathogen and its host immune system (see section 1.3.1).

## 1.2 Immunity

Viral infections in hosts provoke a response from the immune system, which works in higher vertebrates both to suppress acute stages of infection, and establish a pathogen-specific immune state to deal with current and future infections. The specific response is developed and mounted by the adaptive immune system; in particular, the proliferation of T and B cells, and the release of immunoglobulins [106].

While the adaptive immune system is both fast and effective at targeting invasions by previously encountered pathogens, its role in host defence in the first days of novel infection is secondary to that of the innate immune system [141, 142]. The latter is non-specific and immediate, requiring neither prior experience of the invading virus, nor time for lymphocytes to undergo proliferation before mounting a response. Cells and proteins of the innate immune system are ever-present in a healthy host, and can respond to invading pathogens within the first minutes and hours of infection [140]. This system is a key process in preventing the establishment of new infections.

## 1.2.1 The innate immune system

The vertebrate innate immune response is mounted by a network of different white blood cells (*leukocytes*), effector molecules, and signalling molecules. They are all present in a healthy host at all times, so that they may be ready to deal with any pathogen the moment it invades.

### Cells

*Macrophages* reside in tissue, and can phagocytose non-self<sup>2</sup> (for example, bacteria) and virus-infected cells (as part of the adaptive immune response). On encountering microbes, macrophages secrete proteins that alter the physical properties of nearby cells (such as increasing the permeability of blood vessels), and others that induce the migration of *neutrophils* (one of three polymorphonuclear leukocytes, or granulocytes) to the site of infection from the blood supply, in the process known as *inflammation*. Macrophages and neutrophils are both examples of inflammatory cells [106].

*Mast cells* are thought to have roles in the defence against parasites, and the triggering of allergic responses [143], and also recruit the other two granulocytes, *eosinophils* (which defend against parasites, and whose function is dependent on the adaptive immune response) and *basophils* (whose function is believed to be similar to that of mast cells) [33].

*Dendritic cells* phagocytose non-self and infected cells, and also continually take up and monitor extracellular material in a process known as macropinocytosis. However, their primary role is one of surveillance: on detection of a pathogen (for example, bacterial or viral proteins), a dendritic cell matures into an *antigen-presenting cell*

---

<sup>2</sup>Broadly speaking, the immune system has one purpose: to distinguish between cells or proteins which are *self*, i.e. part of one's own body, and those which are *non-self*, i.e. foreign material such as invading pathogens. It then attempts to destroy, remove, or surround *non-self*. Autoimmune diseases arise when the immune system mistakenly identifies *self* as *non-self*. Conversely, pathogens which have evolved the ability to disguise themselves as *self* can often avoid provoking an immune response.

and migrates to a lymph node, where it activates pathogen-specific cells of the adaptive immune system [144]. In another example of innate-stimulated adaptive activity, some *interferon producing cells* differentiate into dendritic cells on viral infection and trigger the adaptive T cell-mediated response [109].

Finally, *natural killer (NK) cells*, while strictly *lymphocytes* (i.e. cells of the adaptive immune system) play an important role in innate immunity [27]. They are one of a number of lymphocyte types that lack the antigen-specific receptors normally characterising lymphocytes, and do not need to undergo clonal expansion before mounting an effective response. These are consequently referred to as innate-like lymphocytes. NK cells, which normally reside in lymphoid tissue, migrate to sites of infection by responding to chemical signals released by other cell types, and can recognise and kill many types of virus-infected cells.

### **Effector molecules**

In addition to its cellular response, innate immunity can also deploy a system of plasma proteins known as *complement*. Involved primarily with defence against bacteria, the complement system is a cascade of proteolytic reactions which take place on the surface of invading cells. These reactions have various important functions: they opsonise the pathogens to promote phagocytosis by macrophages and neutrophils; form membrane attack complexes that punch physical holes in and consequently destroy cells; and form proteins that contribute to the inflammatory response [22].

### **Cytokines**

*Cytokines* are an essential component of the immune system. They are a family of small soluble proteins secreted by a multitude of different cells (though largely those of the immune system itself). They can be loosely classified into one of four families: the *hematopoietins*, which include many of the *interleukins (ILs)*; the

*immunoglobulin superfamily*; the *tumour necrosis factor (TNF) family*; and the *interferons* [106]. Cytokines have many autocrine, paracrine, and endocrine effects<sup>3</sup>, such as stimulating other facets of the immune response [80, 126], inducing inflammation [2, 194], increasing body temperature [38, 97], or stimulating the adaptive response. They are responsible for many of the symptoms of tissue rejection [152], autoimmune disorders [199], and some viral infections (e.g. the 1997 avian influenza A H5N1 outbreak – see [197]).

Macrophages, dendritic cells, NK cells, as well as most other cells of the innate and adaptive immune system, secrete cytokines: to provoke inflammatory responses, to induce cell proliferation and migration, to promote or suppress other immune functions; in essence, to communicate with one another and coordinate the immune response. However, some cytokines play a direct role in cellular defences, particularly against viral infections.

### 1.2.2 The interferons

First identified in 1957 [102, 103], the interferons (IFNs) are perhaps the most important cytokines in the innate response to viral infection. They are classified into two types: IFN- $\alpha$  (a family of related proteins) and IFN- $\beta$  together form type I; IFN- $\gamma$  is the sole and unrelated type II interferon [106]. IFN- $\gamma$  is not produced as a direct result of viral infection, but is instead involved in the adaptive response [106]. Consequently, focus will be restricted to the type I IFNs.

IFN- $\alpha$  and IFN- $\beta$  are secreted by cells in response to viral infection, and promote an antiviral response in otherwise susceptible cells [111]. IFN- $\alpha$  secretion is restricted predominantly to leukocytes; in contrast, IFN- $\beta$  is produced by a wide variety of cells. For this reason, the dynamics of production and action of IFN- $\beta$  can be studied *in vitro* in experimentally simple situations.

---

<sup>3</sup>Autocrine effects are those induced by the cytokine in the secreting cell itself; paracrine effects are those induced in a localised region, near to the secreting cell; endocrine effects are those induced throughout the body.

When an IFN-capable cell is infected with a virus, it is believed that the presence of double-stranded RNA (dsRNA) in the cytoplasm, originating from either the viral genome itself or the process of viral replication, induces IFN- $\beta$  expression [105], though other mechanisms may play a role for different types of virus or cells (e.g. [118]). This pathway is complex and not fully understood [80]. IFN- $\beta$  is produced and secreted from the infected cell and then binds to the surfaces of neighbouring cells (as well as that of the producing cell itself). This induces the production of antiviral proteins, such as Mx and PKR (protein kinase regulated by RNA), through the JaK/STAT pathway [111, 192]. These proteins attempt to interfere with and degrade virus-associated proteins and structures, rendering the cells effectively antiviral [122, 182].

However, in the evolutionary arms race between invading viruses and the immune systems that try to protect against them, many viruses have evolved adaptations to counter these defences: for example, some strains of influenza A are able to suppress the induction of IFN  $\alpha/\beta$  via the NS1 gene [91, 202]; many viruses can inhibit the function of PKR [119]; herpes simplex virus is in most situations resistant to the antiviral action of IFN (see section 2.1.1); hepatitis C has been shown to evolve resistance to IFN- $\beta$  in cell culture [193].

### **Interferons in treatment**

Interferons were not used widely in treatment until 1980, when recombinant DNA techniques were used to engineer colonies of *E. coli* capable of producing human interferon [156], allowing them to be produced quickly and relatively cheaply for the first time. They have an increasingly broad role in the treatment of diseases. Even though IFN- $\beta$  is produced in response to viral infection, it has been found useful in therapy for a variety of non-virally mediated conditions: at least two subtypes of IFN- $\beta$  (1a and 1b) are used to treat relapsing-remitting courses of multiple sclerosis [165, 181]; IFN- $\beta$  has also been used to treat certain forms of cancer [214]. It is thought that the various anti-inflammatory and immunosuppressive properties of the IFNs lend themselves to this wide array of therapeutic uses [106].

As would be expected, IFNs are also employed for their antiviral effects. IFN- $\alpha$  has been used to treat hepatitis C infections [155] (often in combination with drugs e.g. ribavirin), though this sometimes leads to psychological side effects [49, 107, 174, 191, 207]. Recently, a more targeted approach has been successfully employed: IFN- $\alpha$  has been incorporated (via an adenovirus expressing the IFN- $\alpha$  gene) into a foot-and-mouth disease vaccine for swine [39, 147]. This vaccine provides immediate protection, as the IFN- $\alpha$  defends against infection until the porcine adaptive immune system has raised neutralising antibody to the FMD virus, bridging a gap that might otherwise allow an infection to take hold in the first days after inoculation. This technique has recently been replicated in cattle [163].

## 1.3 History of immune modelling

A great deal of research has been carried out on the biological components of immunity: many cells lines and cytokines have been classified, and their sources and primary actions identified (see section 1.2). However, much less well studied are the *dynamics* of immune activity, that is, the time-dependent behaviour of and interaction between the various agents in immunity. We can construct models of this interaction to better study these dynamics.

### 1.3.1 Viral infections in vivo

Where immunity has been modelled, focus has fallen largely on the adaptive immune system, and in particular how host adaptation to pathogen strains affects the evolution of the pathogen within a single host (e.g. [15–17, 71, 76]).

- Infection by human immunodeficiency virus (HIV) of populations of lymphocytes (T cells in particular) has been widely modelled [30, 41, 57, 93, 115, 136, 158, 159, 169, 170]. These have been used to explain the evolution of the virus [34, 137, 157, 205, 210]; to inform future drug therapy strate-

gies [67, 167, 168, 171, 206]; to study interaction or co-infection with other pathogens [113, 138]. However, many of these models do not include the antiviral action of the immune system: T cells are included only in their role as the susceptible cell population.

- The protozoa which cause malaria, members of the genus *plasmodium*, have an immensely complicated life cycle, with stages in both the mosquito vector and human host. These stages have been the focus of mathematical modelling to better understand this complexity [63, 95, 98, 134, 139, 186].
- Hepatitis C infections have been investigated with mathematical models, particularly in relation to how viral loads vary with different treatment regimens: e.g. the efficacy of IFN- $\alpha$ -2b [155] and ribavirin [50, 92]. In [44], the authors construct a model to explain how the observed viral load in patients varies as a result of a type I interferon response to infection.
- Infections of lymphocytic choriomeningitis virus (LCMV) in mice have been modelled; these models have been used to predict the outcome of experiments [31], inform vaccination strategy [29], and illustrate parameter estimation and model selection in immune modelling [19].
- The within-host modelling of influenza A began in 1976, with a study of infection of the murine respiratory tract [120]: a simple compartmental model was employed to examine the viral dynamics, but it lacked any terms incorporating immune activity. A series of three papers was published by Bocharov and Romanyukha in the early 1990s [32, 127, 128]: these were arguably the first to attempt to integrate innate immunity into a model of the host antiviral response. The last of these papers details a highly intricate within-host model for influenza, which includes IFN production, T and B cell proliferation, and antibodies. However, this model included 13 variables and required the estimation of 60 parameters, and its complexity perhaps undermines its wider applicability. Later work by other researchers has simplified this approach [18, 86].

### 1.3.2 Cytokine signalling networks

On a more abstract level, *cytokine signalling networks* have also been the subject of research: mathematical models have been constructed which aim to replicate the networks of feedback loops, activator-inhibitor systems, and delays by which cells of the immune system (and elsewhere) communicate [150, 166, 185, 204]. Biologically realistic models of this kind are nonlinear and often mathematically intractable [213], but help to raise additional questions and guide further experimental work. For example, one such model has been employed to suggest the mechanism by which helper T cells switch between states [212]; another has been used to study the NK- $\kappa$ B regulatory module [125].

### 1.3.3 Spatial modelling

While there has been much work on spatial modelling of disease spread throughout a host population (i.e. epidemiological modelling) [51, 53, 82, 112, 145, 151, 188, 195], a limited amount has been done at the within-host level, much of which has focused on the growth of bacteria.

- [117] and [114] describe individual-based models of bacterial colonies; the first was used to study growth synchrony<sup>4</sup>, and the second the success of *M. tuberculosis* as a human pathogen.
- Moving from bacterial colonies to viral infections, in [23] the authors describe a simple spatial lattice model of influenza A infection. While the model is able to replicate the viral loads seen in experimental data (which has no spatial structure), it does not include any specific aspects of host immunity (e.g. IFN).
- [69] presents a discrete spatial model of virus spread on a square grid, and includes the action of abstract 'immune effector cells'. However, the grids in

---

<sup>4</sup>Growth synchrony, in the context of colony growth, is a measure of how similar local patterns of growth are to one another within the colony.

this model are small ( $21 \times 21$ ), and the output is not parameterized to spatial data derived from laboratory experiments; in fact, the work explicitly highlights the need for data on spatial disease spread coupled with the concomitant modelling that makes use of it.

#### 1.3.4 Why study immune dynamics?

As we have seen above, models incorporating aspects of immunity have applications in a wide range of problems. Chief among them, perhaps, is in the development of more efficient drug therapy regimes. Mathematical models of virus-immunity interaction allow physicians to better answer questions like, 'How would treating my patient with drug X at times  $t_1$  and  $t_2$  affect the course of infection? What about treating at times  $t_3$  and  $t_4$  instead?'. Such models have been used to estimate the optimal course of HAART (highly-active anti-retroviral therapy) in HIV treatment [62, 96].

Models, like experiments, can also prompt further questions: on what time scales does IFN act? What is the half-life of IFN? What is required for maintenance of an existing IFN-mediated antiviral state? Relating specifically to the work undertaken here, we may quantitatively address questions of dose dependence: for example, how do the dynamics of infection change as the infecting dose is increased?

Another important application for immune modelling is in the improvement of within-host models; these in turn can be used to improve population-level epidemiological models (see, for example, [86]). These models, which are not touched upon in this work, are employed to inform vaccine deployment strategy at the local, national, and global levels. This furthers the aim of reducing the frequency and magnitude of epidemics and pandemics (and their associated mortality and morbidity) such as the infamous influenza pandemic of 1918.

## Spatial immune dynamics

The immune response to viral invasion is an inherently spatial problem: from the paracrine (i.e. local) effects of IFN which attempt to 'wall off' initial sites of infection with antiviral cells, to the recruitment of NKs and macrophages, the fundamentally heterogeneous nature of the host at all scales defines the immunodynamics. The arguments for use of spatial epidemic models set out in [52] apply equally well to models at the host level.

Early spatial dynamics of the innate response are particularly important when considering the establishment of emerging viruses: the ability of a new virus to establish itself in a host species will hinge on how successfully it can evade or overcome the defences mounted by the innate immune system.

In the next section we look at spatial disease spread, and in particular how best it can be interpreted through a synthesis of experimental data and mathematical models.

## 1.4 Spatial disease spread

While work has been done on both *in vivo* non-spatial modelling and spatial but immune-naïve modelling, we have identified a need for spatial virus-immunity modelling integrated directly with experimental data. Models of this kind allow us to study the virus-interferon interaction present in the innate response to viral infection. Crucially, spatial models allow us to study the *local* effects of IFN, and gauge how the antiviral action of IFN might impact the spread of infection in host tissue. These local effects can very clearly be seen in experiments known as *plaque assays*.

### 1.4.1 Plaques and plaque assays

In cell monolayers<sup>5</sup> *in vitro*, as well as epithelial monolayers *in vivo* (such as the surfaces of the respiratory system), an infection may kill cells as it spreads. The patches of dead cells left behind are known as *plaques*. In many *in vitro* systems, disease spread is restricted (by design) to local progression, by some property of either the environment or pathogen. In such cases, plaques grow outward from initial sites of infection, where the pathogen first came into contact with the monolayer.

For viruses that form plaques, doses used *in vitro* can be measured in *plaque forming units*, or *pfu*: for example, a cell monolayer inoculated with 100 pfu of virus should exhibit 100 individual plaques, corresponding to where each of the 100 viable virions began an infection<sup>6</sup>.

*Plaque assays* are used throughout the field of virology for a wide range of purposes: to determine the amount of infectivity in a sample (its titre, measured in pfu); to determine the infectiousness or viability of a particular strain; to gauge the rate of new virion production of a strain (a *supernatant assay*); to quantify the number of infected cells in a culture (an *infectious centres assay*); as well as diverse others. The central premises are that:

- i. after infection, incubation, and staining, the number of plaques visible is a measure of the concentration of viable (i.e. infectious) virus particles in the inoculum used;
- ii. the growth rate (or size) of the plaques is a measure of the rate at which infection progresses.

In this way, given a sample containing an unknown concentration of viable virus particles, a plaque assay can be used to determine this concentration. This tech-

---

<sup>5</sup>A monolayer is a sheet of cells one cell 'deep' – a two-dimensional irregular lattice with a cell at each lattice point.

<sup>6</sup>This situation is more complicated for multipartite viruses (where the virus genome is split amongst two or more virions) such as the gemini plant viruses: in this case, several virions must enter the same cell to ensure productive infection.

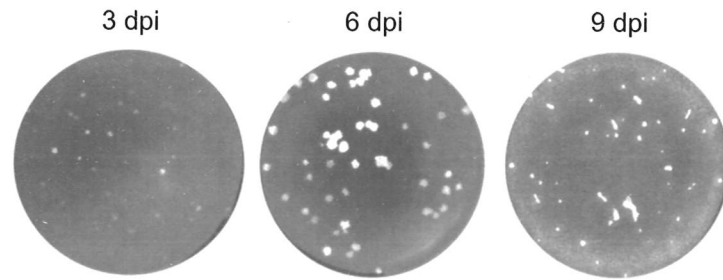


**Figure 1.1:** Plaque assays can be used to study the effects of IFN on virus spread. The images above are taken from plaque assays of Herpes simplex virus infections of epithelial cell monolayers at 3, 6, and 9 days post infection (dpi) – see chapter 2. Images courtesy of Cristina Barreca.

nique works best for low concentrations of viable virions, so that the possibility of plaques merging is reduced. Where it is suspected that high concentrations are being quantified, larger tissue cultures, or (more commonly) serial dilutions can be used.

More relevant here, though, is point ii.: by employing the right combination of virus and cell line, we can use plaque assays to study the rate of spread of viral infection moderated by the antiviral action of the IFN that its presence induces.

#### 1.4.2 Plaque assays as a window on IFN dynamics

Figure 1.1 shows three plaque assays of viral infections of epithelial cell monolayers at 3, 6, and 9 days post infection (dpi) [20, 21]. These pictures exemplify what is meant by ‘local effects’: the action of IFN secreted by infected cells renders susceptible cells antiviral, effectively ‘walling off’ the infection. Local effects like these are missed by non-spatial models, where the total mixing of susceptible and infected cells is assumed.

That plaque assays can readily capture this behaviour indicates that they are an excellent experimental tool for observing the early stages of the innate immune response (in this case, the IFN response to viral infection). A spatial model built to capture the dynamics of *in vitro* viral infection using plaque assays for parameteriza-

tion and comparison would therefore begin to fill the existing gap in virus-immunity spatial modelling research.

## 1.5 Prospectus for the thesis

Despite their importance, the spatiotemporal kinetics of virus-interferon interaction have not been explored via dynamic models integrated with longitudinal viral data. By modelling the dynamics of plaque formation, it is possible to learn more about the timescales involved in IFN-mediated antiviral behaviour. Questions relating to dose dependence can be explored. For example, how do the following key properties of the virus-IFN interaction vary with initial infective dose: the timescale of live infection; the kinetics of IFN production and duration of activity; and the severity of infection-induced pathology? In addition, how might exposing the cells to IFN prior to infection ('priming') affects plaque growth dynamics? Taking a broader view, the construction of spatial models of virus-IFN interaction may further the development of within-host models of viral infection.

### Prospectus

**Overview** This thesis is concerned with the spatial dynamics of *in vitro* viral infections, and falls into two distinct but related halves. The chief aim is to develop a spatial model of viral infection which includes the antiviral response induced by interferon secreted from infected cells; this work forms chapters two, three, and four, the first half of the thesis.

Plaque assays provide the data by which the spatial model is parameterized. However, the results obtained from plaque assays are not always exclusively dependent on the biological properties of the system of cells and pathogen under study. The phenomenon known as *cometing*, wherein plaques of influenza A infection form in unexpected shapes, is an excellent example. Under certain circumstances, normal

circular plaques form as a result of infection spread; in other (previously ill-defined) circumstances, the plaques streak across the monolayer, taking the appearance of comets. This phenomenon is investigated in chapters five and six, and these chapters constitute the second half of the thesis.

**Chapter 2** introduces the experimental data sets used for the development of the spatial model, and discusses how best the data should be converted from simple photographs into quantitative measurements of virus spread.

**Chapter 3** covers the design, implementation, parameterization, and results of the model. Firstly, the various forms the model could take are discussed. The chosen type is developed, parameterized, and compared against the experimental data presented in chapter 2.

**Chapter 4** then details the use of the model to simulate infections at a wide range of doses; the results suggest the existence of critical doses at which the qualitative behaviour of infection change. The biological implications of these results are discussed.

**Chapter 5** introduces a different system (influenza A infection of epithelial cell monolayers) in which, it seems, non-biological factors affect the spread of virus (that is, the formation of plaques). Existing explanations for so-called comet formation are discussed and tested. A fluid dynamic hypothesis for the mechanism behind comet formation is formulated.

**Chapter 6** details a series of experiments performed to test the fluid dynamic hypothesis. The results are summarized and conclusions drawn: while the mechanism responsible for comet formation is found to be fluid dynamic, the driving force behind the comet-forming flow is not precisely determined. The implications that this has for experimentalists are considered, as well as for spatial models of the kind developed in chapter 3.

**Chapter 7** presents a final discussion of the results obtained in the thesis, the limitations of the work undertaken, and highlights areas for future research.

## Chapter 2

# Plaque dynamics of in vitro HSV infection

### 2.1 Introduction

This chapter introduces the experimental system that provides the spatial viral dynamics data for the model: Herpes simplex virus infecting a line of epithelial cells known as MDBKs (Madin-Darby bovine kidney cells). The problem of data analysis is then considered: how best can images of plaque assays be converted into quantitative plaque growth data? Possible methods and their difficulties are identified, and an appropriate analysis is chosen. Chapter 3 then uses this data to construct, parameterize, and test the model.

#### 2.1.1 Herpes simplex virus

Herpes simplex viruses (HSV) are among the most widely and intensively studied of all viruses. Following the development of practical plaque assays for HSV in the early 1960s, they have been used as models to investigate many aspects of virology and cell biology, from virion assembly to membrane structure [179]. In 1962, Schneeweiss

## Chapter 2

# Plaque dynamics of in vitro HSV infection

### 2.1 Introduction

This chapter introduces the experimental system that provides the spatial viral dynamics data for the model: Herpes simplex virus infecting a line of epithelial cells known as MDBKs (Madin-Darby bovine kidney cells). The problem of data analysis is then considered: how best can images of plaque assays be converted into quantitative plaque growth data? Possible methods and their difficulties are identified, and an appropriate analysis is chosen. Chapter 3 then uses this data to construct, parameterize, and test the model.

#### 2.1.1 Herpes simplex virus

Herpes simplex viruses (HSV) are among the most widely and intensively studied of all viruses. Following the development of practical plaque assays for HSV in the early 1960s, they have been used as models to investigate many aspects of virology and cell biology, from virion assembly to membrane structure [179]. In 1962, Schneeweiss

first identified the two subtypes now known as type 1 and 2 [178, 184]. The HSV genome is roughly 152 kbp (kilo base pairs) [132], and there are only relatively small differences between the genomes of the two subtypes. The focus of the modelling work undertaken here will fall on the dynamics of type I HSV (HSV-1) infection.

### **Anatomy of a virion**

Inside a virion, the genome is packaged toroidally [70] inside the *core*, which is surrounded by an icosadeltahedral capsid. This is contained in an amorphous tegument (or covering), which itself is wrapped in a spiked outer envelope [179]. This envelope exhibits a wide range of proteins, which permits the virions to bind to a correspondingly wide variety of cell types. When binding occurs, the envelope rapidly fuses with the cell membrane; at this point the capsid, containing the viral DNA, is transported to the nucleus, where transcription, replication, and virion assembly takes place.

### **Infection of a cell**

Infection results in major changes to the host cell's structure and biochemistry. Particularly relevant to this work is that HSV alters certain characteristics of an infected cell so that *reinfection* is impossible – that is, once successfully infected, additional virions can not bind to the cell surface [198]. Acute wildtype<sup>1</sup> HSV infection of a cell invariably results in cell death.

HSV is a lytic virus<sup>2</sup>: the majority of progeny virions are released on virus-induced cell death roughly 12–24 hours after fusion of the virion to the cell membrane [21]. That said, some virions may leave through the cell membrane and infect neighbouring cells prior to lysis. Like most viral infections, many of the newly formed virions will be defective: incapable in some way of initiating productive infection in a susceptible

---

<sup>1</sup>A strain which has not been altered in the laboratory is said to be *wildtype*.

<sup>2</sup>This is in contrast to, say, HIV: new HIV virions bud off from infected cells throughout the course of productive infection.

cell. The number of viable (non-defective) virus particles released on cytolysis is referred to as the *burst size*. For HSV-1, the burst size has been estimated to be around 100 [160,176].

## **HSV and IFN**

HSV-1 is generally resistant to IFN-mediated immune responses [123]: the genome codes for proteins, such as ICP0 [87,148], which interfere with either the induction or action of type I IFN. However, the virus is sensitive to the IFN response in certain cell lines, such as MDBK cells [73]. It is not known precisely how HSV provokes an IFN- $\beta$  response in MDBK cells. Many viral RNAs are synthesized during HSV infection, and they may be responsible [161]; various proteins on the virion envelope have also been implicated [14].

The exact nature of IFN induction by HSV-1 in MDBK cells aside, it has been shown that in *in vitro* monolayers of these cells, the production of IFN- $\beta$  inhibits the spread of HSV-1 infection [21]. This inhibition is brought about by the transition of as yet uninfected, otherwise susceptible cells to an antiviral state, through in-cell synthesis of antiviral proteins (see section 1.2.2).

### **2.1.2 The experiments**

Peter O'Hare and colleagues at the Marie Curie Research Institute performed experiments to quantify the growth of HSV plaques in two different cell lines [21]. In these experiments, a viscous overlay containing neutralising antibody was used to inhibit long-range diffusion of infectious virions. Use of such an overlay allows infection to progress cell-to-cell only, so that plaques of lysed cells grow smoothly outward from the initial site of infection.

## **Background: performing a plaque assay**

A general introduction to plaque assays was given in section 1.4.1. Protocols for plaque assays vary between laboratories, and with the type of cell and strain of virus being used. However, all plaque assays follow a broadly similar procedure.

Cells of the required type<sup>3</sup> are seeded in a tissue culture dish or well, and medium is added to provide nutrients and protection. They are usually incubated overnight, or until *confluent* (that is, completely covering the base of the well). The original medium is removed and the cells inoculated with medium containing the virus. If the plaque assay is being performed to determine the pfu of the inoculum, a serial dilution may be performed: repeatedly diluting 10-fold the concentration of the inoculum in medium. In this way, the resulting plaques may be more easily counted, and the pfu more accurately estimated.

After allowing the infection to take hold (i.e. the first generation of infections to begin), the inoculating medium is removed, and fresh medium, often mixed with a viscous substance that suppresses diffusion of virions, is added – this mixture is termed the overlay. The wells are returned to the incubator and left for a specified number of days, long enough for any plaques to become visible with the naked eye. After this time, the overlay is removed, and the monolayers washed and fixed with formaldehyde. This kills the cells and halts the infection. The monolayers are then rinsed and stained for the substances being studied (cells, virions, nucleoprotein, etc.). Staining makes the plaques show up more clearly, either under natural lighting or under other frequencies (usually ultra-violet). In this state, the monolayers are totally inert and dry, and can be kept for several days.

The plaques can then be counted and, since the dilutions and volumes used are known, the concentration of viable virus particles in the inoculum can be estimated.

---

<sup>3</sup>Each virus type can usually only infect a specific set of cell lines.

## Overview of experimental results

In cell lines without an IFN response to infection (in this case, Vero cells<sup>4</sup> [48, 56, 177]), infection spreads unchecked until the entire monolayer has been destroyed (figure 2.1a,b). In contrast, in MDBK cells, the production of IFN- $\beta$  in response to the intracellular presence of virus acts to promote an antiviral response which, when established, blocks further spread, and in fact allows the population to recover and undergo regrowth, leading to a reduction in plaque size (figure 2.1c,d).

This series of experiments provides an excellent starting point for the study of the dynamic interplay between virus spread and IFN production: a negative feedback loop where increased infection yields increased suppression of infection.

---

<sup>4</sup>Vero cells are epithelial cells originating from the kidney of the African green monkey.

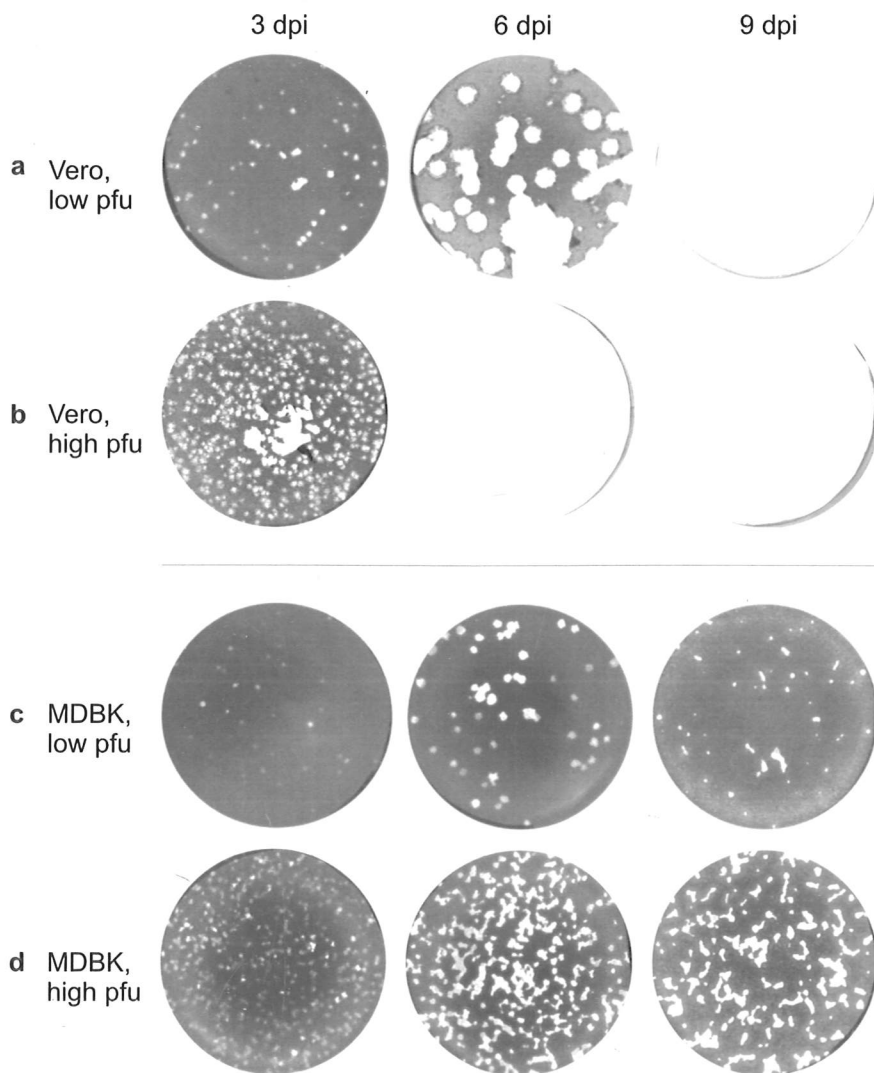


**Figure 2.1:** Progression of HSV-1 infection in cell monolayers. In **a** and **b**, Vero cells, which do not possess an IFN- $\beta$  response to infection, and so are unable to establish an antiviral state, are destroyed by infection, leaving a plaque of dead cells (white). In **c** and **d**, MDBK cells, which begin to secrete IFN- $\beta$  on infection, are able to slow, stop, and reverse the course of infection. In both cell types, inoculating with a comparatively high pfu results in greater plaque coverage than inoculating with a lower pfu. The process of fixing and staining necessarily kills the monolayer, so that the above data were obtained from 12 separate plates, each inoculated and incubated for the required number of days.

## 2.2 Data gathering and analysis

Vero cell monolayers were inoculated with 50 pfu of a strain of wildtype HSV-1; MDBK cell monolayers were inoculated with 10, 50, 500, and 2500 pfu. The data were gathered at 1 – 6 days post-infection (dpi) by fixing and staining the monolayers (so that lysed cells show up white), then photographing the plates. Figure 2.2 shows the resulting data set for the 2500 pfu infection of MDBK cells. Data sets for the remaining experiments are given in appendix A on page 130.

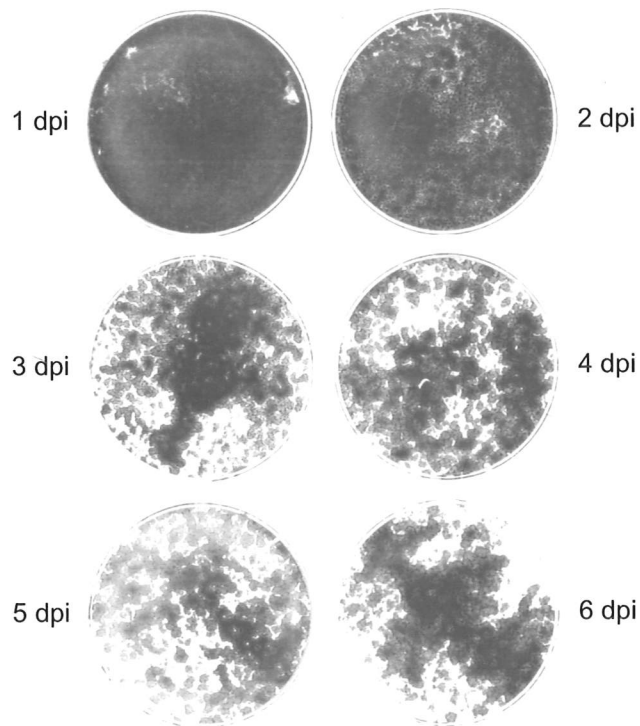


**Figure 2.2:** Data set from MDBK cells infected with 2500 pfu. Each photograph is of a different infection, left for the corresponding number of days before fixing and staining. Clearly visible is the spread of infection during the first few days (shown by the increasingly large white areas). Less clear is the halting of infection and monolayer regrowth that takes place after day 4: a quantitative method for evaluation of plaque coverage must be employed before this becomes obvious.

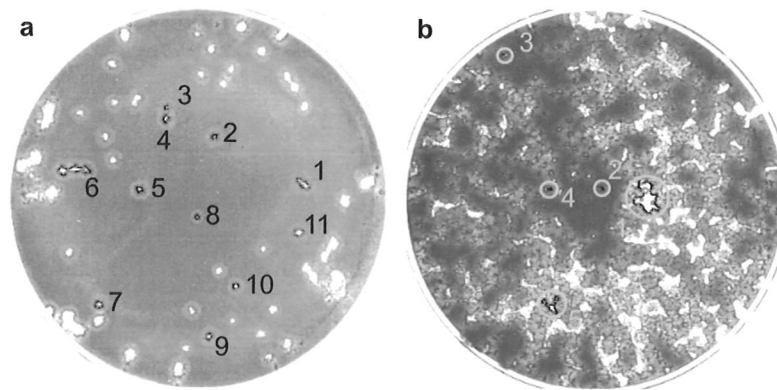


**Figure 2.3:** Selecting plaques for area measurement. Discounting merged plaques, while relatively simple at low pfu (**a**), becomes increasingly difficult as the pfu increases (**b**). Plaques 1 and 6 in **a**, and 1 and 5 in **b**, are most likely the result of merges, and so their areas should be discounted. (This figure is intended to illustrate the process; the images shown are not output of the image recognition software, which would have picked out many more plaques in each case.)

### 2.2.1 Data analysis

Now furnished with a set of photographs of the progress of infection under these various conditions, it remains to translate these images into data which quantitatively describe the plaque growth dynamics. The problem presented in this translation is the irregularity of plaques – of shape, of size, and of placing.

One way to quantify plaque growth might be to compute the average area the plaques in a dish. A difficulty with this approach is that we must decide whether each plaque is the result of a single initial point of infection, or the result of two or more plaques having merged together (figure 2.3). Since it is the growth rate of plaques that is of interest, apparently individual plaques that are in fact artificially large owing to a merging of several smaller ones must be discounted.

The image recognition software *Quantity One* (Bio-Rad, CA) can search for and highlight contiguous regions in bitmapped images. In this case, the contiguous regions being identified are the white or near-white regions of plaque in the photographs of the monolayers. The areas of each of the identified regions can be computed by the software, which counts pixels and makes use of a physical scale

(such as the width in mm that the source photograph spans). The user must then, for each plaque identified, make the determination as to whether it is the result of a merging and, if so, exclude it from the mean plaque area calculation.

Once plaques have been selected for each dose, and each day post-infection, the software computes their areas, yielding time courses of mean plaque area against time. These data are shown in figure 2.4 on the following page. The graph clearly illustrates the unrestricted growth of plaques in Vero cells (lacking an IFN- $\beta$  response to viral infection).

**Dependence of plaque size on dose.** The graph also shows that for MDBK cells, as dose increases, the growth rate of plaques, as well as the maximum attained area, decreases. There is a ready explanation for this: as the dose increases, so too does the number of infected cells for a given time. Since each infected cell is releasing IFN- $\beta$ , this should result in higher IFN- $\beta$  concentrations in the system, and hence a greater suppression of infection (i.e. plaque formation).

The clear regrowth of monolayer (and shrinking of plaques) reported in the literature [21] and depicted in figure 2.1 on page 22 is not wholly reflected in this analysis: only the 50 pfu and 2500 pfu data appear to show monolayer recovery. In addition, the rapid shrinking of the 50 pfu mean plaque area between the 5th and 6th days seems unlikely on biological grounds. We must bear in mind that each data point is taken from a separate infection course (since, as previously mentioned, fixing and staining prior to photography necessarily kills the cells and halts the infection), but even allowing for that fact it is improbable that the cell division is sufficiently rapid for the monolayer to reduce plaque coverage from the 5th day peak to 2nd day levels in a single 24 hour period.

The quantitative data yielded by this method *may* be an accurate reflection of the underlying data. However, it may be tainted by artefacts introduced in the procedure, particularly relating to plaque selection. By insisting that the plaques measured not be the result of a merging of two or more plaques (each centred on its own initial site of infection), one naturally selects for smaller plaques; and since

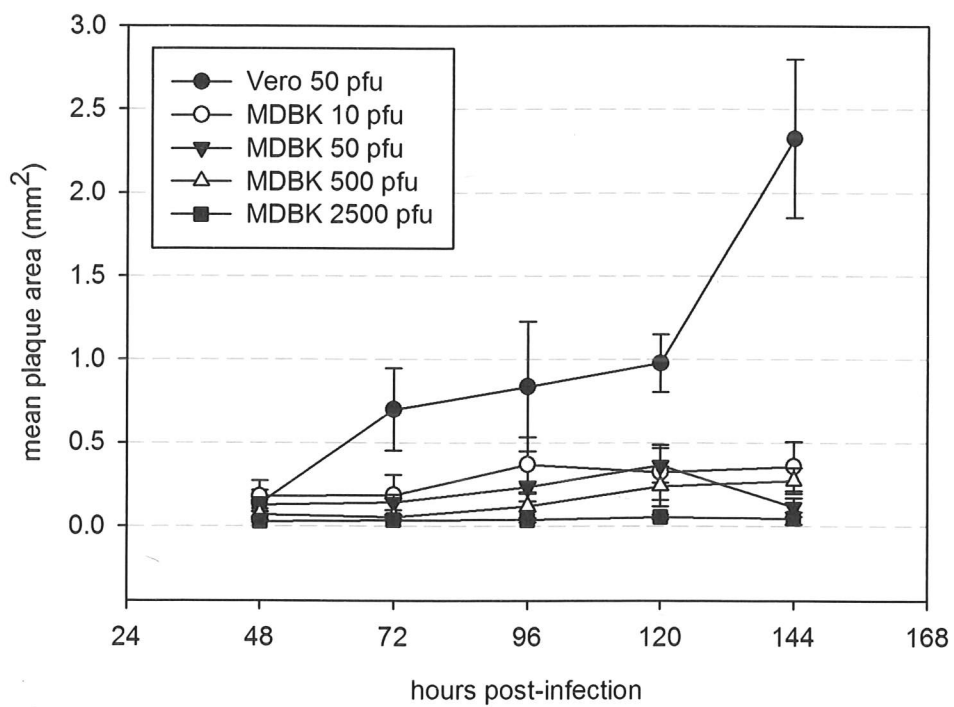


**Figure 2.4:** Mean plaque area against time, calculated by image recognition software. Evident here is the unrestricted growth of plaques in Vero cells, contrasting with the much reduced growth rate in MDBK cells, owing to the antiviral effects of IFN- $\beta$ .

the judgement that an apparent plaque is the result of a merging is subjective, an additional layer of potential inaccuracy is introduced.

### **2.2.2 Data analysis II**

To attempt to rule out analysis artefacts in the data, we can employ a second method to quantify plaque growth dynamics. Here, for each plate photograph, the percentage of the area of the monolayer covered in plaque (henceforth 'percentage plaque'), is calculated. The inoculum's pfu (its ability to form plaques) is a statistical average of the number of plaques that would form should the experiment be repeated many times over; the observed number of plaques will vary somewhat about this average. For large pfu, this variation is unimportant, but for smaller inocula (such as the 10 pfu and 50 pfu experiments), the percentage plaque must be normalized against the actual number of plaques evident. Of course, this counting of plaques introduces the same subjectivity encountered in the first analysis; however, as it is only necessary to perform this normalization at low pfu (where the variation in plaque number is of significant size compared with the mean), at which it is easier to identify individual plaques (even when they have merged), this method is less susceptible to error.

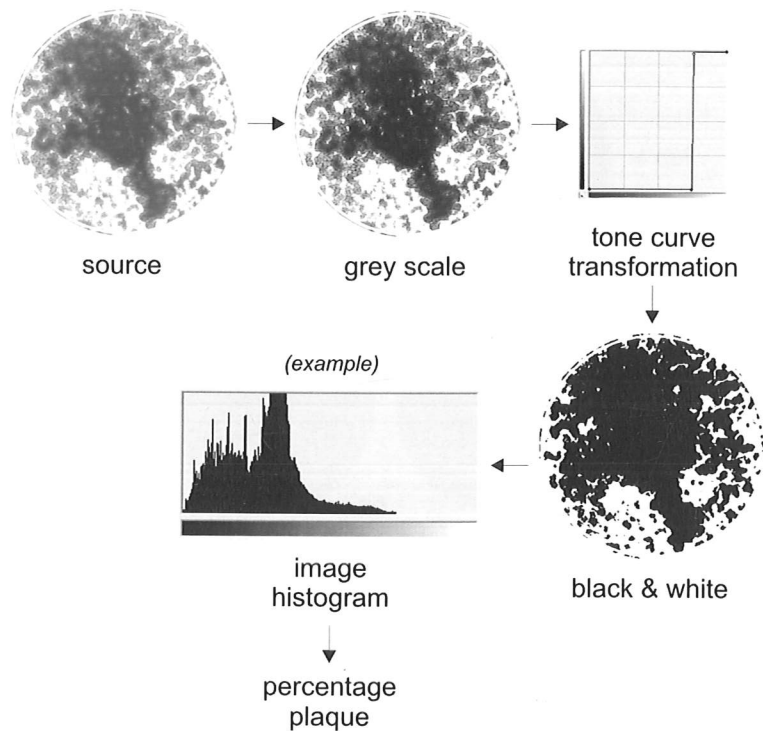


**Figure 2.5:** Image transformation technique employed to measure percentage plaque coverage in photographs of plaque assays. After converting from full colour to greyscale, the tone curve transformation defines a mapping between initial and final pixel colours: to determine the final colour of a pixel in the image, find its initial colour on the x axis and travel upward until the transformation line is intersected – the y coordinate of the point of intersection gives the final colour. The purpose of the depicted transformation is to map all greys darker than a given threshold to black, and everything else to white. By inspecting high magnification images of plaques during this process, the correct threshold can be estimated. The percentage of white pixels (i.e. the percentage plaque) can then be read from the image histogram. (The image histogram displayed is an example, and does not correlate with the images shown.)

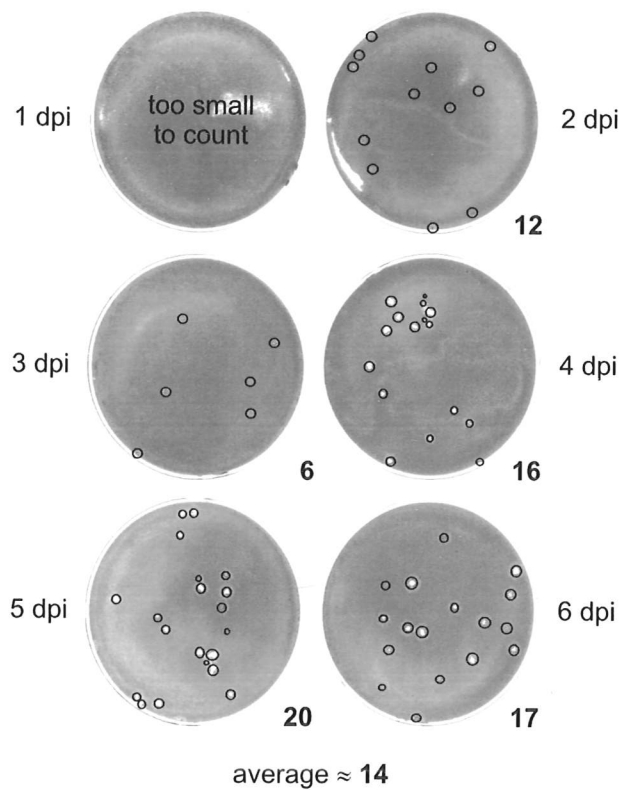


**Figure 2.6:** Counting plaques in the MDBK 10 pfu plates. Following image transformation and calculation of percentage plaque, the percentages are scaled to the average of 14 pfu.

Calculating the percentage plaque by hand for a monolayer becomes very difficult as the inoculum pfu increases. Instead, the photographs are passed through several image filters; following this, areas of plaque show up white, and everything else is rendered black (figure 2.5 on the preceding page). The percentage plaque, now simply percentage of white pixels in the image, can then be simply calculated from the image histogram. For the lower pfu experiments, the number of plaques observed at each day post-infection are then counted, so that the percentage plaque values can be normalised (figure 2.6). For example, in the MDBK 10 pfu data set (shown), the average number of plaques seen is 14 and the number seen in the 5 dpi plate is 20, so that the percentage plaque for 5 dpi will be scaled by  $\frac{14}{20}$ .

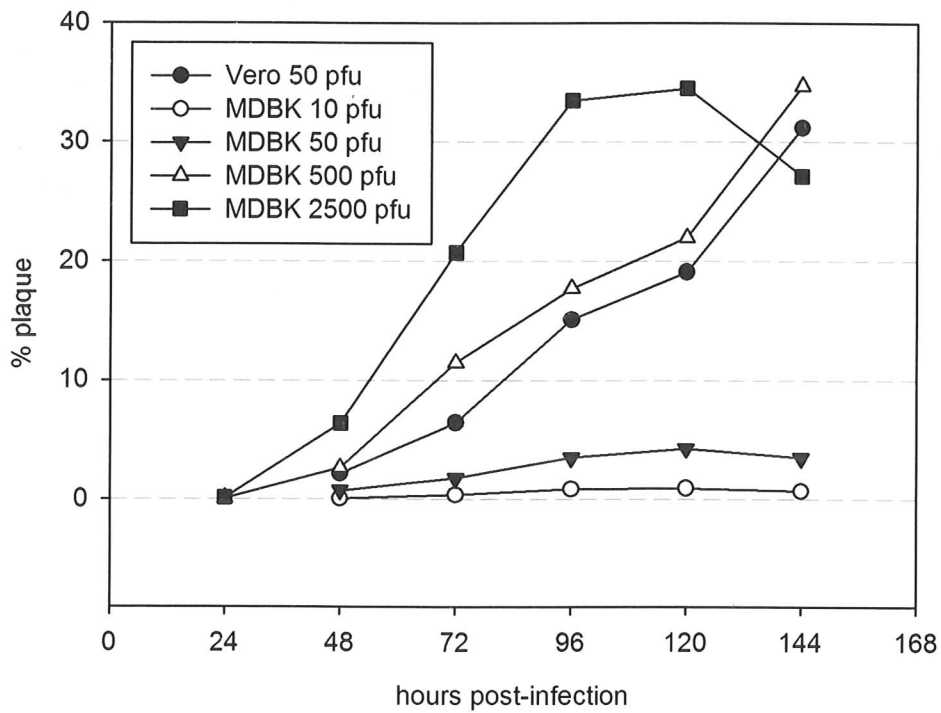


**Figure 2.7:** % plaque against time for the Vero and MDBK experiments. Evident again is the unrestricted growth of plaque coverage in Vero cells, which contrasts with the much reduced growth rate in MDBK cells.

After transformation, the data take the form of a series of monolayer plaque percentages, for the Vero experiment at 50 pfu, and the MDBK experiments at 10 pfu, 50 pfu, 500 pfu, and 2500 pfu (figure 2.7).

### 2.2.3 Summary

In both analyses, the unrestricted growth of plaques in Vero cells is easily seen in the data. In the second, the data for MDBK 10, 50, and 2500 pfu cases show quantitatively the antiviral effects of the IFN response to HSV infection that MDBK cells possess (observed experimentally [21]). Initially, the percentage plaque increases as the infection takes hold; subsequently, plaque growth slows as the increasing IFN concentration impedes new infection. It stops entirely once the antiviral state is reached at around 5 dpi; regrowth of the monolayer then takes over, and the plaques shrink (evidenced as a decrease in percentage plaque).

The data for the MDBK 500 pfu infection appear anomalous, since although plaque growth appears to slow between the 4th and 5th dpi, the data point for the 6th day shows an unexpectedly high percentage plaque. This is perhaps due to a spurious experimental outcome. In light of this, the 6 dpi data point was not included during parameterization of the model. It may be, however, that this result is not anomalous, but rather indicative of another course that HSV infection may take in this system; we return to this point in the discussion in the following chapter.

Since this second method is less prone to artefacts as a result of subjective judgements made about the merging of plaques, and because it quantitatively shows the monolayer regrowth in MDBK cells already published [21], we shall use this analysis for model parameterization.

Now that we have a data set describing plaque growth dynamics in MDBK and Vero cells (i.e. with and without IFN), we may begin the construction of a model to capture this behaviour. The following chapter discusses the possible types of models that may be developed to study this problem, before setting out the design, implementation, and parameterization of the type chosen.

### 2.2.3 Summary

In both analyses, the unrestricted growth of plaques in Vero cells is easily seen in the data. In the second, the data for MDBK 10, 50, and 2500 pfu cases show quantitatively the antiviral effects of the IFN response to HSV infection that MDBK cells possess (observed experimentally [21]). Initially, the percentage plaque increases as the infection takes hold; subsequently, plaque growth slows as the increasing IFN concentration impedes new infection. It stops entirely once the antiviral state is reached at around 5 dpi; regrowth of the monolayer then takes over, and the plaques shrink (evidenced as a decrease in percentage plaque).

The data for the MDBK 500 pfu infection appear anomalous, since although plaque growth appears to slow between the 4th and 5th dpi, the data point for the 6th day shows an unexpectedly high percentage plaque. This is perhaps due to a spurious experimental outcome. In light of this, the 6 dpi data point was not included during parameterization of the model. It may be, however, that this result is not anomalous, but rather indicative of another course that HSV infection may take in this system; we return to this point in the discussion in the following chapter.

Since this second method is less prone to artefacts as a result of subjective judgements made about the merging of plaques, and because it quantitatively shows the monolayer regrowth in MDBK cells already published [21], we shall use this analysis for model parameterization.

Now that we have a data set describing plaque growth dynamics in MDBK and Vero cells (i.e. with and without IFN), we may begin the construction of a model to capture this behaviour. The following chapter discusses the possible types of models that may be developed to study this problem, before setting out the design, implementation, and parameterization of the type chosen.

## Chapter 3

# A stochastic model of *in vitro* HSV spread

### 3.1 Introduction

In the previous chapter we obtained a quantitative description of *in vitro* plaque growth dynamics in Vero and MDBK cells at various initial doses for up to 6 days post infection. In this chapter we discuss the types of model that might capture the observed dynamics, then go on to construct the type chosen. The model is parameterized to the data and then used to answer questions about dose dependence and cell priming by IFN before infection. Infections are simulated at a wide range of initial doses. Key results and their biological implications are discussed. Additional applications of the model and directions for future development are highlighted.

#### 3.1.1 Rationale for a stochastic spatial model

The cell-to-cell spread of a viral infection and concomitant plaque formation in a tissue culture is an inherently spatial problem. Therefore, if one is to construct a model of the system, one could argue that it should in the first instance be spatial

– it should capture the spatial heterogeneity of infection, and the patterns which it creates.

The length scale of the experiments ( $\sim 3$  cm), relatively small number of cells ( $\sim 10^6$ ) and virions ( $\sim 10^8$ ), cell-to-cell spread of infection, and the small number of infection events which take place (particularly at low pfu and during the early stages of infection) suggest that we begin with an individual-based spatially-explicit stochastic model [53]. The fact that a tissue culture is effectively a two dimensional sheet of cells lends it perfectly to being modelled by an array of objects arranged and interconnected in the same way.

We could instead proceed with an analytic spatial diffusion model, or model the different states of cells, the virions, and the IFN as fields or fluids which evolve or flow with time (see, for example, [42, 72, 151]). However, this would introduce an inappropriate approximation: each cell is a discrete entity, and the stochastic events (infection, lysis, etc.) which take place at the cellular length scale can not be overlooked [52]. We return to this point in the discussion in the next chapter.

An individual-based spatial model constructed to simulate this system functions, in effect, as a 'virtual' tissue culture: each cell *in vitro* is represented by a virtual one *in silico*, which can move between the same states (such as healthy, infected, or lysed) as time progresses.

## 3.2 Model design

### 3.2.1 Model schematics

A diagram showing how an infection progresses in the virtual monolayer is shown in figure 3.1 on the next page. A schematic of model execution can be seen in figure 3.2 on page 35. The remainder of this section explains individual aspects of the model.

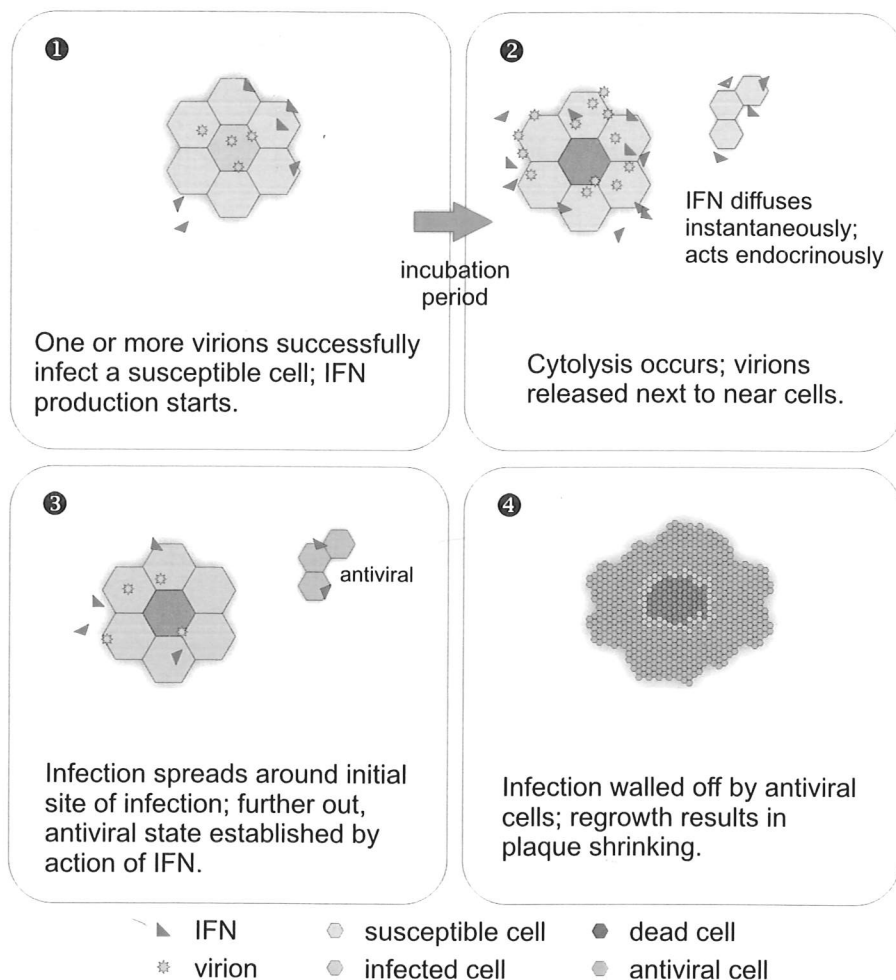


**Figure 3.1:** Progression of infection in the model. ① Virions successfully infect susceptible cells with probability  $\rho$ , which decreases monotonically with increasing IFN concentration (thus capturing the IFN-mediated suppression of infection). On infection, IFN production is begun; actual secretion starts after a delay of between 4-6 hours. ② The incubation period for infection is around 12 hours, after which cytolysis occurs with a viable virion burst size normally distributed about 100; viable virions are scattered to neighbouring cells according to the previously determined neighbour weightings. IFN secreted by infected cells acts in an endocrine manner (i.e. globally) to reduce the probability of successful infection,  $\rho$ , and to initiate an antiviral state in uninfected cells. ③ Virions released at cytolysis go on to infect neighbouring susceptible cells. Away from infection, IFN brings about an antiviral state in susceptible cells after a time  $\tau$ . ④ All susceptible cells have entered an antiviral state, resulting in a cease of the spread of infection. Cell monolayer regrowth takes place as cells divide.

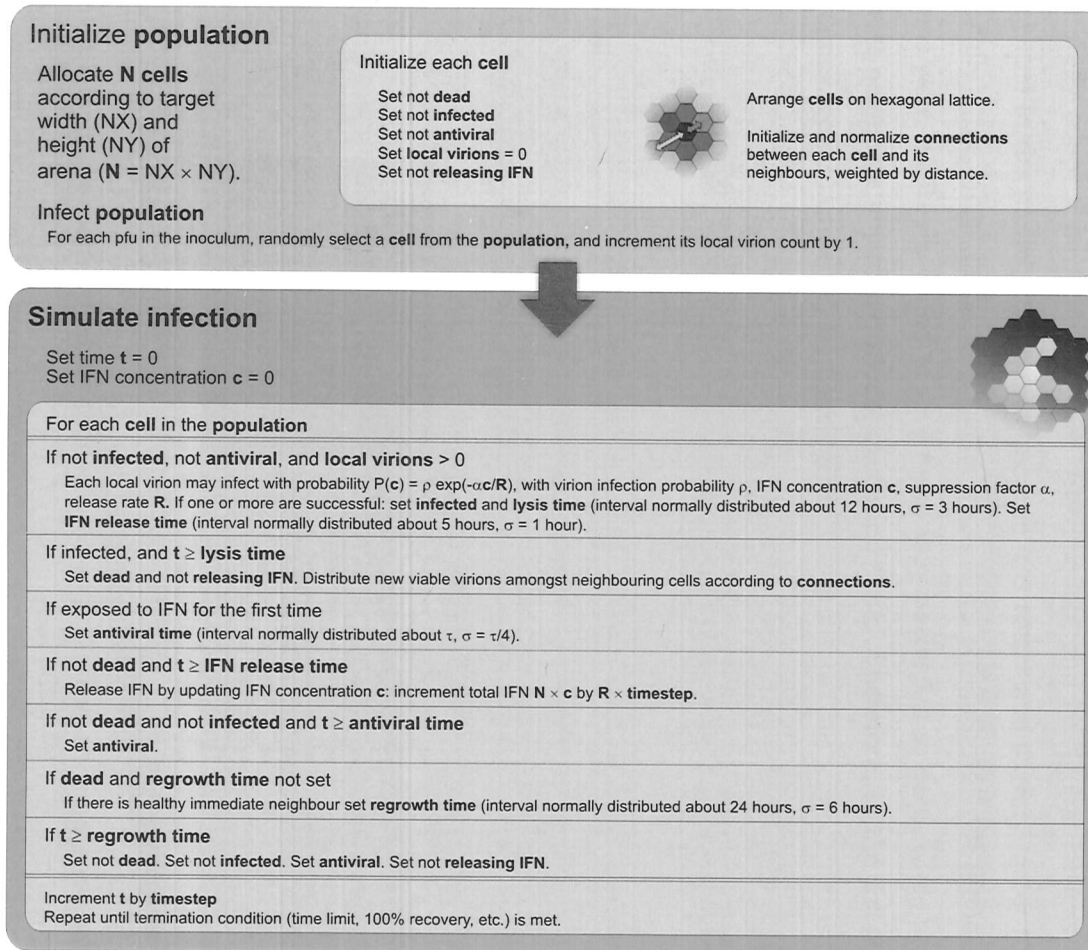


**Figure 3.2:** Schematic of model execution. Execution begins with allocation and initialisation of the cell objects, including the establishment of inter-cell connections which define the geometry of the virtual monolayer (in this case, a hexagonal array). The monolayer is then infected, by randomly depositing a viable virion for each unit of pfu in the inoculum. Time and IFN concentration are set to zero, then the model iterates through each cell, updating the state of each according to the model equations and parameters. Extracellular virion counts are cached, so that new virions released by a cell do not infect neighbouring cells in the same iteration. Model execution stops once the specified termination condition has been fulfilled. This is usually a time limit, but may also be specified by percentage plaque, IFN concentration, or any other model variable.

### 3.2.2 The virtual monolayer

How, then, should these cell objects be arranged to best reflect a real monolayer? And how should they be connected?

Perhaps the simplest way to cover a flat two-dimensional region is to use a set of squares placed on a square lattice. However, figure 3.3 suggests that a hexagonal lattice might better reflect the layout. In fact, the formation of epithelial cell monolayers has been studied using dynamic models: in [153], the authors prove that a set of cells growing, dividing, and spreading to fill a region (as epithelial cells do) will naturally adopt a hexagonal layout. Both square and hexagonal lattices were implemented in the model, the former because it is easier and slightly faster (computationally), the latter because it better represents an epithelial cell monolayer. Hexagons were eventually found to give marginally better fits to data, while having an almost negligible impact on model execution time. Therefore, in the following, only the hexagonal lattice will be considered.

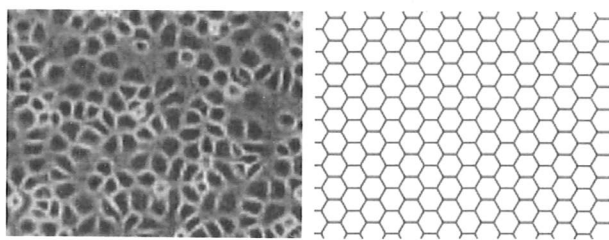


**Figure 3.3:** Epithelial cells compared with a hexagonal lattice. The arrangement of cells in a confluent MDCK cell monolayer (left) can be approximated with a hexagonal lattice. In the photograph, the more prominent spherical-looking cells have either recently divided (epithelial cells undergoing division generally revert to a spherical form before doing so) or have been forced above the monolayer through lack of space.

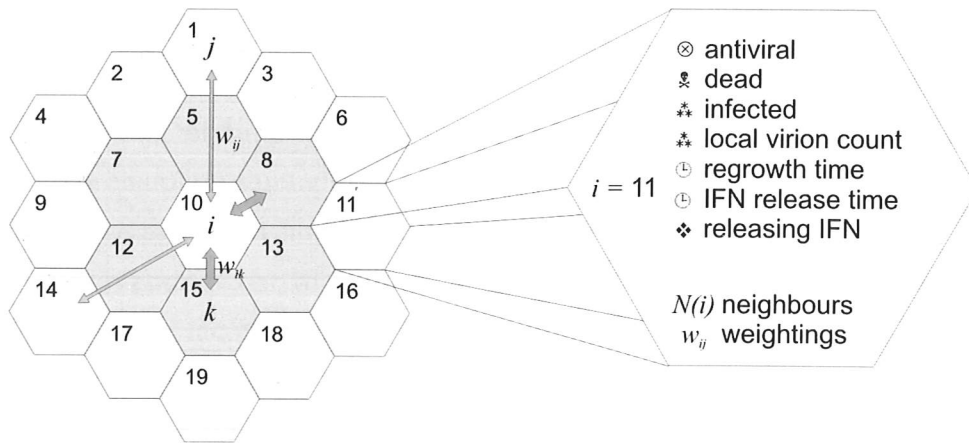


**Figure 3.4:** Connections and variables on the hexagonal lattice. Each cell object, represented by a hexagon, contains variables which record its state and connections to neighbouring cells.

The state of the virtual monolayer is stored in a large array of cell objects. Each cell  $C_i$  stores a list of other cells,  $N(i)$ , that are its 'neighbours', as well as variables which track the state of the cell (figure 3.4). It is to these neighbours that virions may be scattered on cytolysis. Neighbours are not only the adjacent hexagons on the lattice: they can be up to two hexagons distant, allowing both for the possibility that virions released on lysis may drift a short distance (the viscous overlay prevents longer range motion), and also for cells to have more than 6 neighbours. The connections  $w_{ij}$  between neighbours are weighted by distance, falling off in magnitude as  $\frac{1}{r^2}$ . The weights are normalised so that for each  $i$ ,

$$\sum_j w_{ij} = 1$$

Initially, to better approximate the heterogeneity in cell distribution in live monolayers, the addition of random variation to these weightings was investigated: weightings were multiplied by random variables taken from various distributions on the interval  $[0, 1]$ . However, this addition was found to have no qualitative effect on model behaviour. Therefore, the regular lattice, with weightings depending only on separation distance, was used throughout subsequent work.

### 3.2.3 The time step

The discretising of time is an inevitability when modelling: no variable can be tracked continuously throughout the evolution of a system. Instead, it must suffice to evolve the system in finite steps. Reducing the length of the time step brings the approximation closer to the continuous reality, affording greater accuracy, but at the expense of increased run time. In general, a miniscule time step would reflect the real world more clearly, but would take too long, or cost too much, to run on a computer. The trick, then, is to balance the demands of accuracy against the demands of expediency [173].

In this system, most timescales are of the order of hours: the incubation period of HSV-1 is roughly 12 hours; the division time of MDBK cells is, on average, 24 hours; the delay between virus exposure and IFN production is 4-6 hours [21]. The time step must therefore be smaller than 4 hours. On the other hand, there are no processes being modelled that occur on a timescale of less than 1 hour. This gives us a lower bound on the time step.

Since the model is parameterized using experimental data from up to 6 dpi, each run can be expected to simulate up to at least 120 hours of virtual monolayer time. Since simulations of 120 hour (and longer) infections with a time step of 1 hour completed in an acceptable time on the computer systems available, this time step was adopted throughout the work.

### 3.2.4 Diffusion and interferon

When compared with HSV-1 virions, IFN molecules are very small. For example, IFN- $\beta$  proteins have (approximate) molecular weights ranging from 18 kD up to 38 kD [36], i.e.  $3.0 - 6.3 \times 10^{-24}$  kg; all types are made up of around 170 amino acids [106]. In contrast HSV-1's genome alone has 152,260 base pairs [132], and each virion has a dry weight of around  $1.33 \times 10^{-18}$  kg [179] – around two hundred thousand times heavier.

This marked difference in size means that, while the viscous overlay used to suppress long range diffusion (i.e. across the tissue culture dish) of HSV-1 virions does succeed in this aim, IFN- $\beta$  molecules may still diffuse quite quickly. In fact, in this model it is assumed that IFN diffusion proceeds at a sufficient rate to equilibrate IFN concentration within a single time step<sup>1</sup>. This means that the IFN concentration can be considered homogeneous in the virtual monolayer, and needs only to be evolved at the global level.

### 3.2.5 Scattering of virions on cytolysis

Virions are the only local extracellular quantity tracked in this model. Each position in the lattice has a variable storing the number of local virions, which are present immediately outside the cell, on the cell surface or in the extracellular medium.

During infection, virions are sufficiently small in number that it is feasible to consider them in the model as discrete entities (as they are in reality). A burst of 100 virions on lysis of an infected cell in the virtual monolayer will result in a net increase of 100 virions in the local virion count for the corresponding lattice position; these new virions are then scattered to the cell's neighbours, proportionally by weighting. Changes in local virion counts are cached and applied at the end of each time step.

### 3.2.6 Binding of virions and the action of IFN

During a time step, virions present in the medium around a cell may bind to and attempt to infect it, provided it is alive and uninfected<sup>2</sup>. Infection (during a time step) occurs with probability  $\rho$ . The number of successful infections staged by  $N$  virions can therefore be sampled from the binomial distribution for  $N$  trials each with probability of success  $\rho$ .

---

<sup>1</sup>Of course, this assumption is dependent on the chosen time step of 1 hour; were smaller time steps to be considered, IFN diffusion might not be accurately described by such simplification.

<sup>2</sup>On infection of a cell, HSV-1 inhibits successful binding of additional virions to its surface – see section 2.1.1.

The antiviral action of IFN- $\beta$  is included here by multiplying this probability  $\rho$  by a suppression factor,  $\exp\left(-\frac{\alpha C}{R}\right)$ , where  $C$  is the IFN concentration,  $R$  is the IFN release rate for a cell (which, given we are free to choose the units of IFN, can be set to 1), and  $\alpha$  is the parameter dictating the magnitude of infection suppression by IFN. For a cell which is antiviral,  $\rho = 0$ . When virions bind to the cell surface, they leave the extracellular medium, and so the local virion count is reduced accordingly. The time at which IFN release begins is set (this is normally distributed about 5 hours, standard deviation  $\sigma = 1$  hour) [21]. On infection the time-to-lysis for the cell is set – this incubation period is normally distributed about 12 hours ( $\sigma = 3$  hours).

IFN also acts to bring about an antiviral state in susceptible cells. The average time taken for a cell to establish this state, after first exposure to IFN, is another parameter of the system: the hours-to-antiviral,  $\tau$ . While it is possible that this time is dependent on the IFN concentration (in some perhaps highly complex way; for example, dependent on initial concentration, or a time-integral of concentration), for the purposes of the model it is assumed that the time taken is independent of IFN concentration. This contrasts with the concentration dependent manner in which IFN is assumed to suppress viral infection, which is captured in the IFN suppression factor  $\alpha$ .

### 3.2.7 Underlying algorithms and equations

Like many individual-based computational models (e.g. cellular automata), the model state evolves according to procedural code rather than a set of equations. As an example, the following code, executed for each cell in each time step, defines precisely how cells move from an uninfected to an infected state – this corresponds to the first loop step in the *Simulate infection* box in figure 3.2.

```

1  if Cell->IsAlive and not Cell->Infected then
2       $\Delta$ Virions = BinomialSample( Cell->LocalVirions,
3           $\rho \times \text{Exp}(-\alpha \times \text{IFNConcentration})$  )

```

The antiviral action of IFN- $\beta$  is included here by multiplying this probability  $\rho$  by a suppression factor,  $\exp\left(-\frac{\alpha C}{R}\right)$ , where  $C$  is the IFN concentration,  $R$  is the IFN release rate for a cell (which, given we are free to choose the units of IFN, can be set to 1), and  $\alpha$  is the parameter dictating the magnitude of infection suppression by IFN. For a cell which is antiviral,  $\rho = 0$ . When virions bind to the cell surface, they leave the extracellular medium, and so the local virion count is reduced accordingly. The time at which IFN release begins is set (this is normally distributed about 5 hours, standard deviation  $\sigma = 1$  hour) [21]. On infection the time-to-lysis for the cell is set – this incubation period is normally distributed about 12 hours ( $\sigma = 3$  hours).

IFN also acts to bring about an antiviral state in susceptible cells. The average time taken for a cell to establish this state, after first exposure to IFN, is another parameter of the system: the hours-to-antiviral,  $\tau$ . While it is possible that this time is dependent on the IFN concentration (in some perhaps highly complex way; for example, dependent on initial concentration, or a time-integral of concentration), for the purposes of the model it is assumed that the time taken is independent of IFN concentration. This contrasts with the concentration dependent manner in which IFN is assumed to suppress viral infection, which is captured in the IFN suppression factor  $\alpha$ .

### 3.2.7 Underlying algorithms and equations

Like many individual-based computational models (e.g. cellular automata), the model state evolves according to procedural code rather than a set of equations. As an example, the following code, executed for each cell in each time step, defines precisely how cells move from an uninfected to an infected state – this corresponds to the first loop step in the *Simulate infection* box in figure 3.2.

```
1 if Cell->IsAlive and not Cell->Infected then
2      $\Delta$ Virions = BinomialSample( Cell->LocalVirions,
3      $\rho \times \text{Exp}(-\alpha \times \text{IFNConcentration})$  )
```

```

4     if  $\Delta$ Virions > 0 then
5         Cell->Infected = true
6         Cell->LocalVirions -=  $\Delta$ Virions
7         SetLysisTime(Cell)
8         SetIFNReleaseTime(Cell)
9     end if
10 end if

```

On line 2 in the above, the function `BinomialSample( n, p )` samples from the binomial distribution, returning a number of successes in  $n$  trials, each with probability of success  $p$ .

On line 3, we see the infection-suppressing property of IFN acting through the IFN suppression factor  $\alpha$  in the form of an exponential. Initially, since no data existed to suggest a specific functional form  $F(C)$  for this action, and the conditions on its properties are weak ( $F(0) = 1$ ,  $F(C) \geq 0$ ,  $F'(C) \leq 0$  for all  $C$ ), several different forms were investigated. Those that introduced extra parameters into the model (e.g. a threshold value for the IFN concentration  $C$ ) were rejected for simplicity. It was found that the qualitative model behaviour was not sensitive to the choice of form for  $F(C)$ : for example, using  $F(C) = \left(1 + \left(\frac{\alpha C}{R}\right)^2\right)^{-1}$  in place of  $F(C) = \exp\left(-\frac{\alpha C}{R}\right)$  results only in different values for the fitted parameters.

As we saw in section 3.2.2, neighbours of a given hexagon on the lattice can be up to two hexagons distant. This maximum distance  $L$  was varied during model development: up to  $L = 2$ , resulting parameter fits varied but qualitative model behaviour remained the same; for  $L \geq 3$ , the model became increasingly sensitive to the infection probability  $\rho$  (the transition from extremely limited plaque growth to excessively fast plaque growth occurred over an ever-decreasing range).

### 3.2.8 Random numbers and the binomial distribution

Stochastic simulations necessarily require a fast and reliable method for generating pseudo-random numbers. Owing to its speed, quality of output, and ease of

implementation, the *Mersenne Twister* algorithm was employed [129]. From this, uniformly distributed (pseudo-)random numbers on  $[0, 1]$  can be generated, and from them normally distributed ones (with any given mean and standard deviation). To sample efficiently from the binomial distribution, the *rejection method* was employed, as described in [173].

### 3.2.9 Implementation

The model was implemented in C++ and compiled to run on several different platforms.

## 3.3 Parameterization

### 3.3.1 Parameters

The parameters determining model behaviour are summarized in table 3.1 on the next page. Many parameters values can be taken from the literature as a first approximation [21, 160]: viral burst size = 100; incubation period = 12 hours; cell division time = 24 hours; and IFN secretion delay (the time between stimulation by viral infection and first secretion of IFN) = 5 hours. By choice of units of IFN, the IFN secretion rate can be scaled to 1.

The three unknown parameters in the model are the virion infection probability  $\rho$ ; the IFN suppression factor  $\alpha$ , a summary parameter which encompasses the ways in which IFN impedes infection (and so effectively reduces  $\rho$ ); and the hours-to-antiviral  $\tau$ , the average time taken for an uninfected but IFN-exposed cell to reach an IFN-mediated antiviral state. These free parameters must be estimated by fitting the model to the experimental data.

<i>name</i>	<i>estimate</i>	<i>source</i>
burst size	100 virions	[160]
cell division time	24 hours	[21]
hours to antiviral	$\tau$	<i>free parameter</i>
IFN secretion delay	5 hours	[21]
IFN release rate	1 unit/hour	by choice of units
IFN suppression factor	$\alpha$	<i>free parameter</i>
incubation period	12 hours	[21]
virion infection probability	$\rho \in [0, 1]$	<i>free parameter</i>

**Table 3.1:** Model parameters and their estimates

### 3.3.2 Parameter fitting

The data consist of a series of percentages, each describing the extent of plaque coverage in a monolayer at differing days post-infection. In the model, infections at the relevant pfu can be simulated to the required dpi, and the percentage plaque in the virtual monolayer compared with the data.

Unknown parameters were estimated by nonlinear least squares<sup>3</sup>: the parameters are chosen so that the squared distance between the mean of an ensemble of model realizations and the experimental data is minimized.

### 3.3.3 Fitting to the Vero data set

When fitting to the Vero data set, only one of the three unknown parameters,  $\rho$ , must be estimated (since the other two,  $\alpha$  and  $\tau$ , relate to IFN activity, which is not relevant in IFN-incapable Vero cells).

The  $\rho$  parameter space  $[0, 1]$  was searched: the squared distances between model outputs and experimental data were computed. Smaller values of this squared distance indicate that the model more closely fits the experimental data. Minimising

<sup>3</sup>While more sophisticated estimation techniques exist, such as maximum likelihood estimation, the forgiving shape of the objective function surface and the closeness of fit justifies the use of this method *a posteriori* [64].

this resulted in a virion infection probability (in Vero cells) of  $\rho = 0.8$ .

### 3.3.4 Confidence intervals and regions

When fitting parameters to data, it is possible to calculate confidence intervals and regions for the estimates. Suppose  $p$  parameters are being fit to  $n$  data points in a model. Let  $S(\theta)$ , a surface in  $(p + 1)$ -space, be the squared distance of the model output from the experimental data, where  $\theta$  is a  $p$ -vector of the parameters. Let  $S(\hat{\theta})$  be the observed minimum value of  $S(\theta)$ , occurring at  $\theta = \hat{\theta}$ . We can then use the  $F$  distribution to calculate the 95% confidence contour  $S(\tilde{\theta})$  about  $S(\hat{\theta})$ , and therefore a confidence region in  $p$ -space for  $\hat{\theta}$  [58]:

$$\frac{\left(\frac{S(\tilde{\theta}) - S(\hat{\theta})}{p}\right)}{\frac{S(\hat{\theta})}{n-p}} = F_{\text{inv}}(p, n - p, 0.05)$$

Here,  $F_{\text{inv}}(p, n - p, 0.05)$  is the inverse of the cumulative distribution function for the  $F$  distribution with numerator degrees of freedom  $p$  and denominator degrees of freedom  $n - p$ , evaluated at the probability 0.05 (yielding a 95% confidence interval). Rearranging this expression gives a value for  $S(\tilde{\theta})$ .

This technique was applied to the Vero parameter fit (where the number of parameters  $p = 1$  and the number of data points  $n = 6$ , one for each day post-infection), giving a 95% confidence interval about  $\rho = 0.8$  of (0.74, 0.87).

### 3.3.5 Fitting to the MDBK data sets

Following successful parameterization of the model to IFN-free (Vero) experiments, it remains to parameterise the model to the MDBK data. Since MDBK cells and Vero cells are different cell lines, from different animals and with different properties, it is also necessary to re-estimate the value of the virion infection probability  $\rho$ .

There are four sets of data available ( $n = 23$  points in all, the 6 dpi measurement from the MDBK 500 experiment having been discounted) and  $p = 3$  parameters ( $\rho$ ,  $\alpha$ , and  $\tau$ ) to estimate. The challenge here is to parameterize using all four data sets simultaneously, choosing a single set of parameter values for which the model accurately reflects the data at each of the four doses – this would indicate that the model has successfully captured the dose dependence in the system.

With three parameters to estimate concurrently, parameter fitting becomes more complicated. It is difficult to produce three dimensional volume plots that can display a 4th dimension of information (in this case, model distance from experimental data). While it would in theory be possible to implement an algorithm to search the parameter space, such as the simplex method described by Nelder and Mead [154], the stochasticity in the model means that convergence would be difficult to achieve without an exceptionally high number of realisations, which would in turn lead to excessively long run times.

A more simple iterative approach was employed: fix one parameter, vary the other two (creating a 2D objective function surface plot), choose parameters to minimize distance, then fix one of them and vary the other two. While there is no guarantee that this method will converge to the global minimum, it appears to in practice and does in this case provide a practical and easily implemented method for parameterization.

At each iteration, the normalized squared distances from each of the four sets were summed, and this plotted against the two parameters: figure 3.5 on the following page shows the final step in this process. The roughly elliptical confidence region shown in **b** allows us to compute the confidence intervals for the parameter estimates. The minimum total distance between model output and experimental data for  $\rho$  against  $\alpha$  is  $S(\hat{\theta}) \approx 0.023$  (marked  $\times$  in figure 3.5**b**). The 95% confidence

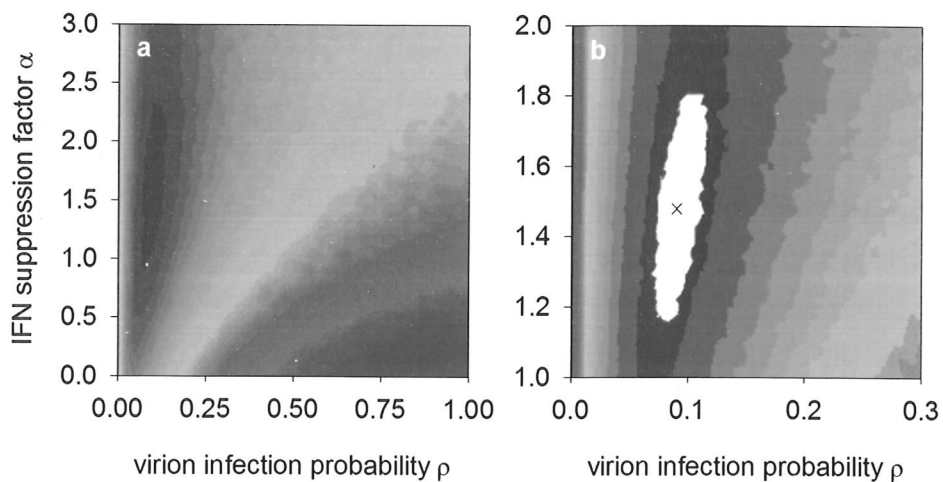


**Figure 3.5:** Parameter fitting to MDBK data sets. Sum of squared distance of model predictions for the four data sets. The distances are displayed as colours: dark reds (good fits) to dark blues (poor fits). Only one of the three possible pairs of parameters ( $\rho$  against  $\alpha$ ) is shown here as an example. The objective function surface for varying  $\rho$  and  $\alpha$  is shown in **a**, and with the computed confidence region in **b**.

<i>parameter</i>	<i>value</i>	<i>95% CI</i>
hours to antiviral $\tau$	95 hours	(88, 101)
IFN suppression factor $\alpha$	1.5	(1.1, 1.9)
virion infection probability $\rho$	0.09	(0.07, 0.11)

**Table 3.2:** Results of parameterization to MDBK data sets.

region contour is therefore:

$$\frac{\left(\frac{S(\tilde{\theta}) - 0.022758}{3}\right)}{\frac{S(\hat{\theta})}{23-3}} = F_{\text{inv}}(3, 23 - 3, 0.05) \approx 3.4668$$

$$\Rightarrow S(\tilde{\theta}) \approx 0.030272$$

The parameter estimates and confidence intervals obtained from this method are shown in table 3.2.

### The parameter estimates

The considerably lower value of  $\rho$  for MDBK cells suggests that they are less susceptible to infection by HSV-1 than Vero cells. However, it may also reflect the suppressive effect that the presence of an IFN response has from the early stages of infection. The time to reach an antiviral state of  $\tau = 95$  hours is relatively long; in an infection *in vivo*, the adaptive response would most likely be acting to suppress the infection by this time [106]. However, this value reflects the time at which plaque shrinking is witnessed in the MDBK data. The IFN suppression factor  $\alpha$  is a purely abstract parameter, to which it is difficult to ascribe any specific biological significance.

After parameterization, the final fits to experimental data are shown in figure 3.6 on the following page.

### Robustness of model output to parameter values

During parameter fitting, the values of the fixed parameters (taken from the literature – see table 3.1) were varied to gauge the sensitivity of the model to these inputs. For each of the five fixed parameters, small variations in their values (for example, increasing the virion burst size from 100 to 200 virions) prior to parameter fitting resulted in changes to the values of fitted parameters ( $\alpha$ ,  $\rho$ , and  $\tau$ ) but no qualitative change in model behaviour.

- Increasing the burst size slightly has the effect of reducing the fitted value of the virion infection probability  $\rho$  – since more infectious particles are available to infect cells, the probability of successful infection for each must be reduced to recapture the observed plaque growth rates.
- Varying the cell division time affects the rate at which monolayer regrowth (i.e. plaque shrinkage) occurs upon the establishment of an antiviral state.
- Increasing the IFN secretion delay works to reduce the overall concentration

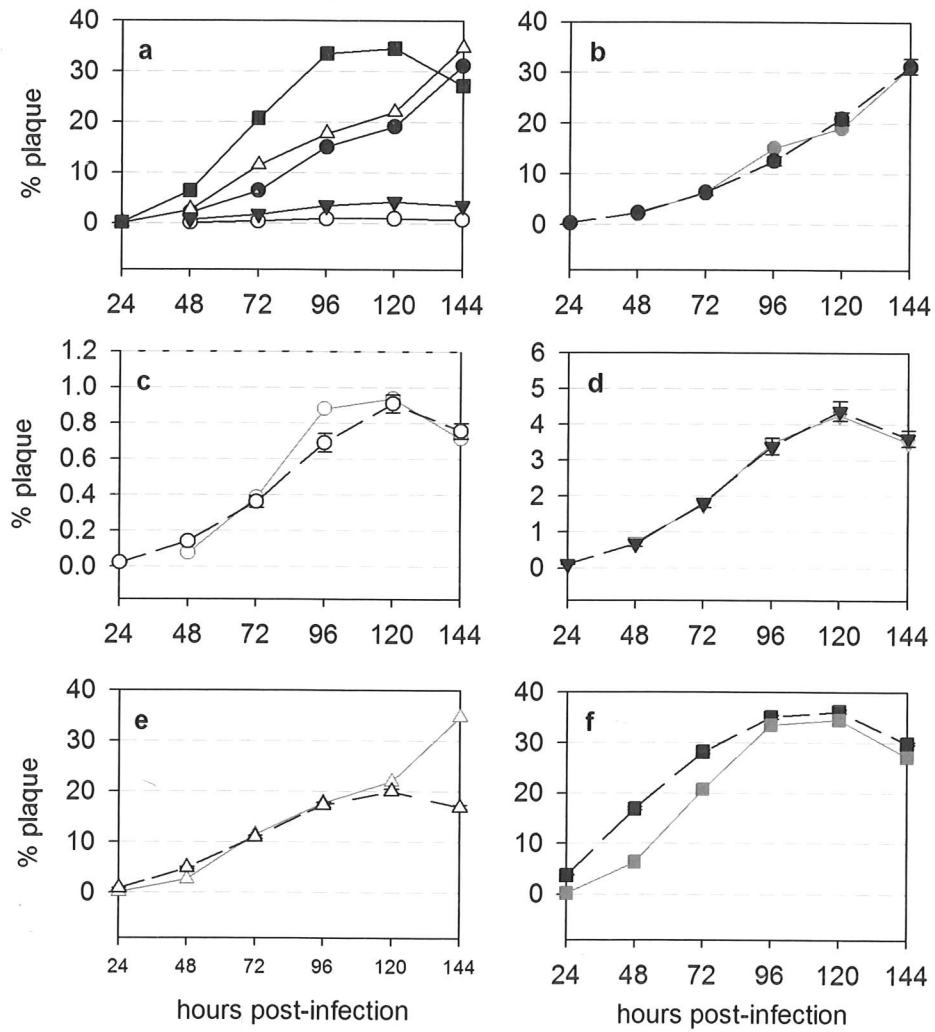


**Figure 3.6:** Experimental data (solid lines) compared with results of parameter fitting (dashed lines). **a** All data, and model predictions for **b** Vero 50 pfu (●), **c** MDBK 10 pfu (○), **d** MDBK 50 pfu (▼), **e** MDBK 500 pfu (△), and **f** MDBK 2500 pfu (■). The last experimental data point in **e** diverges greatly from the model prediction – see section 2.2.3. Model output was averaged over 20 realizations.

of IFN present in an infection, and so has the effect of decreasing the fitted value of the hours to antiviral  $\tau$ , and increasing that of the IFN suppression factor  $\alpha$ .

- The IFN release rate was set to 1 by choice of units.
- Increasing the viral incubation period acts to reduce the growth rate of plaques, leading to an increased fitted value for the virion infection probability.

Similarly, changing the values of any of the parameters after fitting did not result in qualitative changes in model behaviour.

### 3.4 Discussion: quality of fit

The fits in figure 3.6 on the previous page show that this stochastic model is able to capture the dependence of plaque formation dynamics on the dose in the inoculum. Not only are the magnitudes of the peak percentage plaques correct (aside from the anomalous result in the MDBK 500 pfu data), but the recovery rates and times are accurately reflected as well. Comparing the four MDBK fits with one another, it seems that **f** (MDBK 2500 pfu) is the least good. It is not clear why this is the case: it may reflect the difficulty in capturing dose dependence (fitting the same parameter set to four separate pieces of data obtained under different initial conditions), or it may be that the quoted pfu of 2500 is an overestimate of actual inoculum pfu used in the experiments.

In the next chapter, this model acts as the 'virtual' tissue culture dish suggested in the introduction, allowing us to investigate many different initial conditions and make predictions *in silico* about the outcome of experiments *in vitro*.

## Chapter 4

# Simulating virus-IFN-cell dynamics

### 4.1 Introduction

In the last chapter we constructed a stochastic model of *in vitro* HSV infection. Now parameterized, this model can be used to simulate experiments. Figure 4.1 on the following page shows an example of graphical output from an *in silico* infection. In addition, three animations of simulated infections are provided on the CD accompanying this thesis; please see the `readme.txt` file in the root folder for more information.

In chapter 1 we examined the motivation behind immune system modelling. Faced now with a parameterized model of the virus-IFN-cell dynamics in *in vitro* HSV infection, there are several questions we can ask of it.

- Do the course, characteristics, and outcome of infection change qualitatively with dose? If so, in what ways? Can we ascribe biological reasons to the observed effects?
- IFN has already been employed as pre-infection or pre-exposure antiviral treatment (e.g. in the recent work of Grubman and colleagues [39, 147, 163]), and is used as a therapy for other infections, both viral and non-viral (see section

## Chapter 4

# Simulating virus-IFN-cell dynamics

### 4.1 Introduction

In the last chapter we constructed a stochastic model of *in vitro* HSV infection. Now parameterized, this model can be used to simulate experiments. Figure 4.1 on the following page shows an example of graphical output from an *in silico* infection. In addition, three animations of simulated infections are provided on the CD accompanying this thesis; please see the `readme.txt` file in the root folder for more information.

In chapter 1 we examined the motivation behind immune system modelling. Faced now with a parameterized model of the virus-IFN-cell dynamics in *in vitro* HSV infection, there are several questions we can ask of it.

- Do the course, characteristics, and outcome of infection change qualitatively with dose? If so, in what ways? Can we ascribe biological reasons to the observed effects?
- IFN has already been employed as pre-infection or pre-exposure antiviral treatment (e.g. in the recent work of Grubman and colleagues [39, 147, 163]), and is used as a therapy for other infections, both viral and non-viral (see section

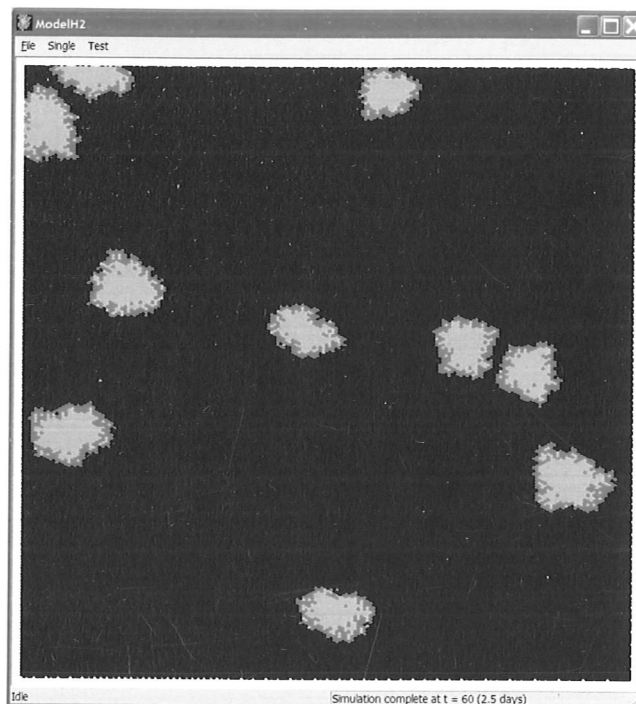


**Figure 4.1:** Graphical output from the model. This shows a  $200 \times 200$  hexagonal MDBK-like cell area, infected with 10 pfu of inoculum and left for 60 hours. These plaques appear much larger than those in the photographs at similar times post-infection (figure 2.1 on page 22) because in reality the cell monolayers contain between  $2.0 - 3.0 \times 10^6$  cells [21], so that this window represents less than a 60th of the total monolayer area.

1.2.2). It is important to have a conceptual understanding of how and when IFN pre-treatment or therapy might work in other cases. We begin to address this issue by simulating cell priming by IFN and comparing the results with the outcomes of analogous laboratory experiments (for *in vitro* HSV infection).

In this chapter we address these questions, discuss the results and biological implications, and highlight directions for future research.

## 4.2 Results

To investigate dose dependence, 'virtual' plates were inoculated with varying doses  $\nu$  from  $10^1$  to  $10^7$  pfu. Infections were run through to 400 hours, recording percentage plaque, IFN concentration, and virion production every 2 hours (figure 4.2 on the next page). The results suggest that the qualitative dynamics of the infection change across the following three critical threshold doses.

### 4.2.1 Total monolayer destruction

The IFN-mediated antiviral state takes time to be established throughout the monolayer. Provided the infection has not destroyed all cells by this time, antiviral cells should remain; these can go on to divide and re-establish the monolayer. Hence there exists a critical dose, below which antiviral effects take hold before total destruction, and above which destruction occurs before an antiviral state is reached. Running the model for sufficiently long (beyond any point at which an antiviral state might be achieved) allows us to determine the eventual state of the monolayer. If, by this time, plaque coverage is 100%, then recovery can never take place; if not, regrowth is underway and monolayer recovery will follow. Figure 4.3 on page 54 shows the percentage plaque at  $t = 400$  hours plotted against dose. From this it can be deduced that the critical dose for total monolayer destruction is  $\nu_D \approx 2.2 \times 10^6$  pfu, or roughly 0.9 pfu/cell.

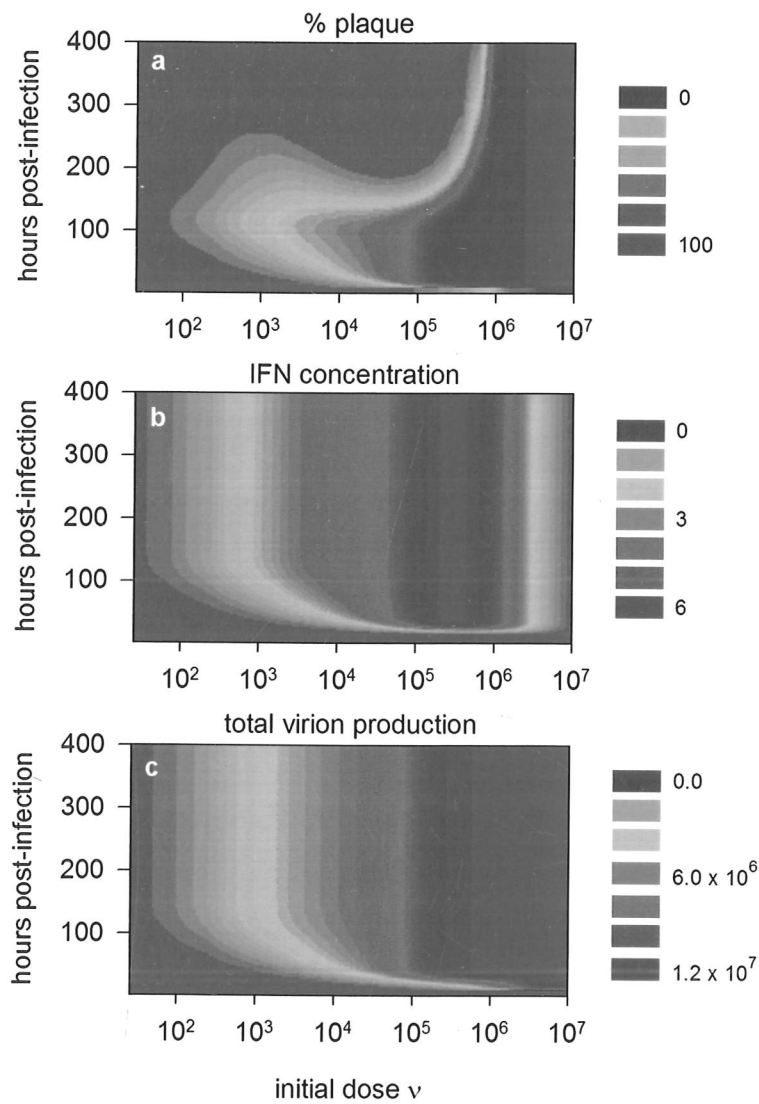


**Figure 4.2:** Model time series profiles at doses  $\nu$  from  $10^1$  to  $10^7$  pfu: **a** % plaque; **b** IFN concentration; **c** total virion production. Model output was averaged over 50 realizations.

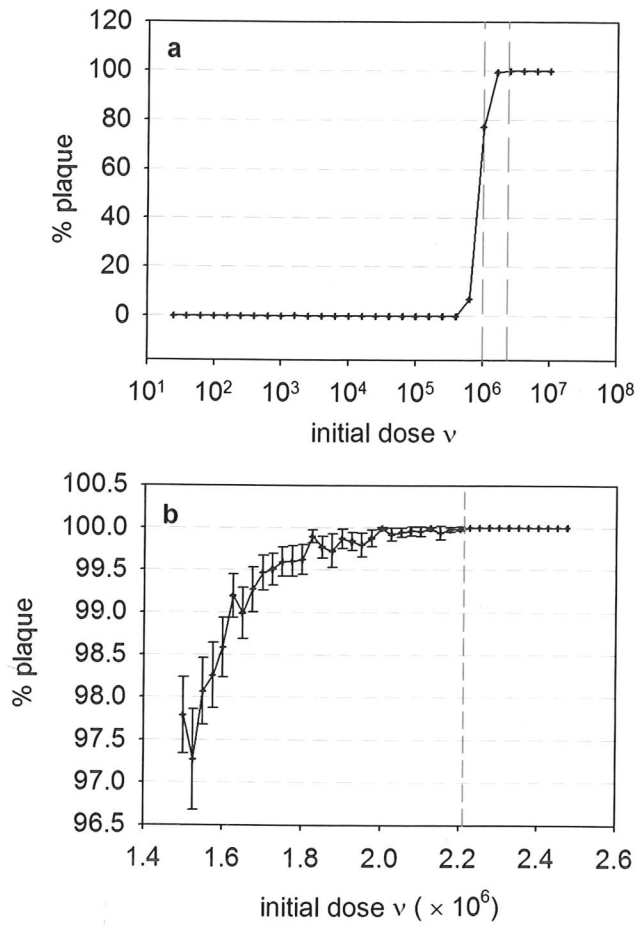


**Figure 4.3:** Determining the critical dose  $\nu_D$  for total monolayer destruction. Percentage plaque at  $t = 400$  hours post-infection with **a**  $10^1 - 10^7$  pfu; **b**  $10^6 - 3 \times 10^6$  pfu. The critical dose  $\nu_D \approx 2.2 \times 10^6$  pfu is marked in **b**.

### 4.2.2 Maximizing IFN- $\beta$ production

Figure 4.2b shows an apparent unimodal relationship between IFN production and dose, and the existence of a second critical dose for maximal IFN- $\beta$  production. IFN concentration at the end of infection was plotted against dose (figure 4.4), from which the critical dose for maximal IFN- $\beta$  production of  $\nu_i \approx 3.2 \times 10^5$  pfu (or roughly 0.1 pfu/cell) can be estimated. The existence and value of this critical dose is discussed further in section 4.3 on page 58.

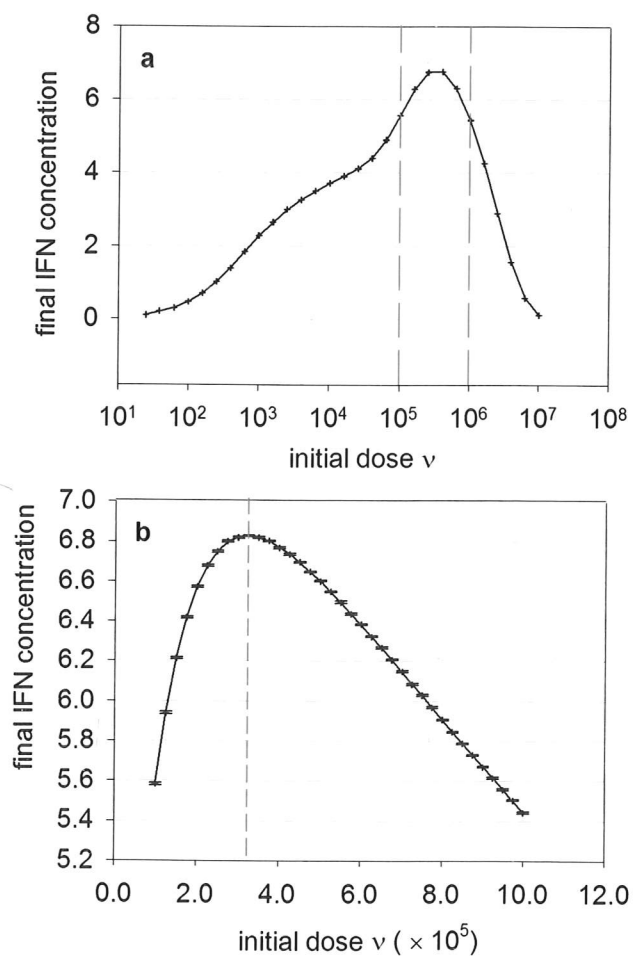


**Figure 4.4:** Determining the critical dose  $\nu_i$  for maximal IFN- $\beta$  production. IFN concentration at  $t = 400$  hours post-infection for **a**  $10^1 - 10^7$  pfu; **b**  $10^5 - 10^6$  pfu. The critical dose  $\nu_i \approx 3.2 \times 10^5$  pfu is marked in **b**.

### 4.2.3 Minimizing recovery time

For the purposes of modelling, the recovery time is taken to mean the time at which total regrowth is completed (i.e. the time taken for all hexagons in the lattice to once again contain a live healthy 'cell'). The recovery time for doses from  $10^1$  to  $10^7$  pfu was calculated and plotted (figure 4.5 on the next page), as well as the time and magnitude of percentage plaque peak (that is, the highest value of the percentage of the monolayer covered with dead cells throughout infection). The non-monotonicity of recovery against dose suggested by the slightly upturned leftward protuberance of lighter colours into the darker region in figure 4.2a is clearly visible. In the cases where 100% plaque (i.e. total monolayer destruction) is achieved, regrowth is not possible (as there are no living cells to re-seed the plate), and so the algorithm used to find the recovery time terminates after  $t = 480$  hours. The critical dose for minimal recovery time was found to be  $\nu_R \approx 5.0 \times 10^4$  pfu, or 0.02 pfu/cell.

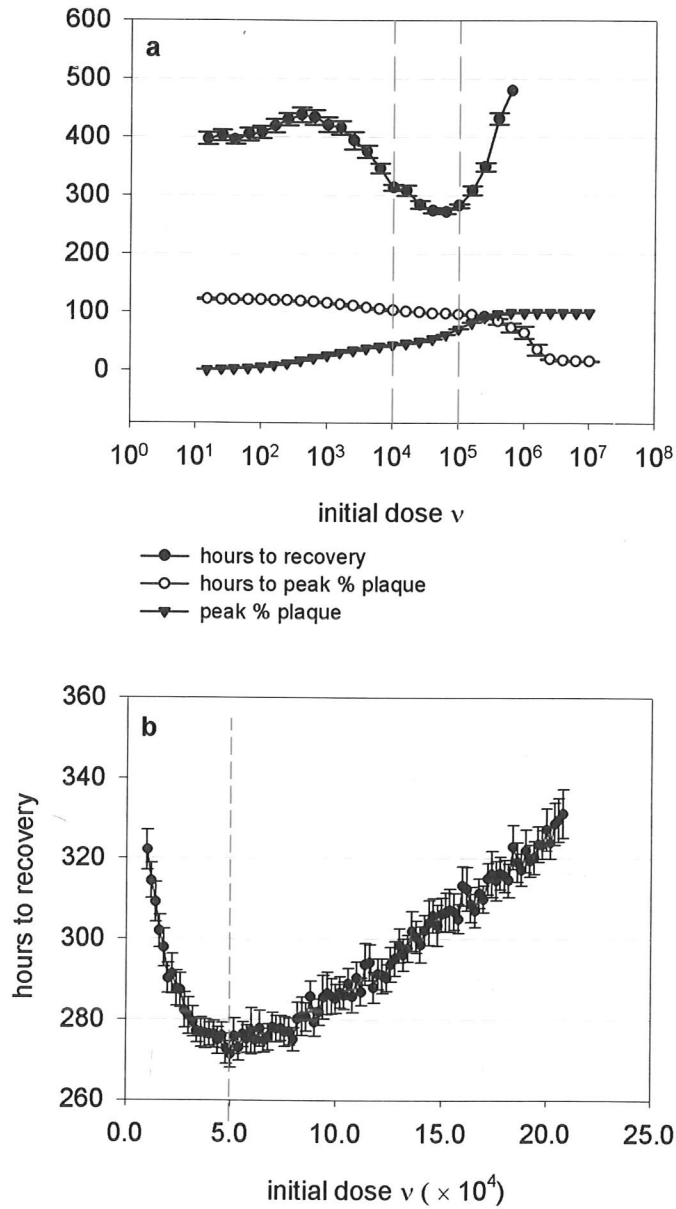


**Figure 4.5:** Determining the dose  $\nu_R$  for minimal recovery time. Time to recovery and time and magnitude of the peak in percentage plaque after infection with **a**  $10^1 - 10^7$  pfu; **b**  $10^4 - 2 \times 10^5$  pfu. The critical dose  $\nu_R \approx 5.0 \times 10^4$  pfu is marked in **b**.

#### 4.2.4 Priming of cells prior to infection

During infections in hosts, cells may be primed with IFN (produced in infected regions elsewhere in the body), prior to exposure to the virus itself. In vitro experiments confirm that monolayers treated with IFN show increased resistance to viral infection [21]. Naïve MDBK cells treated for 12 hours with medium (shown to contain IFN- $\beta$ ) harvested at 3 dpi from an initial infection (of 7000 pfu) leads to a  $\approx 96\%$  reduction in plaque count on subsequent infection using a standard dose of 1000 pfu, compared with untreated cells similarly infected.

We can test the stochastic model against these results. Using the model, the IFN concentration in the medium resulting from a 7000 pfu infection at 3 dpi was estimated ( $\approx 3.4$  units/cell); this quantity was then used to pre-treat 25 'virtual' monolayers for 12 hours, after which 1000 pfu infections were simulated. An average plaque count reduction to 2.4% of original counts (with confidence interval [1.3%, 3.4%]) was observed, in broad agreement with the experimental results presented in [21]. The results also indicated that priming is very effective in reducing the maximum size to which plaques grow over the infection (see the animation supplied on the accompanying CD).

### 4.3 Summary of qualitative plaque dynamics

These results suggest the existence of three distinct critical viral dosages, each an order of magnitude larger than the next (table 4.1 on the following page)<sup>1</sup>. The first,  $\nu_D \approx 0.9$  pfu/cell, defines the boundary between total eventual recovery and total destruction of the monolayer. Since virion production is directly proportional (ignoring stochastic variation) to the number of infected cells, this critical dose is also the one at which maximum virion production occurs (since all cells become infected). Increasing the dose above this point merely results in a shorter live

---

<sup>1</sup>It should be noted that even the smallest of these doses is still much larger than highest dose used in the experiments described in chapter 2: the 2500 pfu dose in a tissue culture dish containing roughly  $2.5 \times 10^6$  cells equates to around 0.001 pfu/cell

infection – the end result (total destruction) remains the same, as does (on average) the number of virions produced by the infection. It is perhaps surprising that  $\nu_D$  is so high: 0.9 pfu/cell indicates that, on average, 90% of the monolayer will be destroyed in the first round of infection, and yet, from these results, doses at or below this will still result in eventual monolayer recovery. In an experimental setting, however, this theoretical recovery time may well exceed the time for which such cultures can successfully be kept alive *in vitro* under infection conditions.

The second critical dose,  $\nu_I \approx 0.1$  pfu/cell, is that at which maximum final IFN concentration is reached. This result is less surprising: a delicate balance is struck at an intermediate dosage, between too small an infection which stimulates only a small number of cells to begin IFN- $\beta$  secretion, and too large an infection which results in the secreting cells being killed off too quickly. The large concentrations of IFN produced at intermediate doses are the result of cells exposed to virus (but not productively infected) at the 'turning point' of the infection, as an antiviral state is reached in the monolayer – of course, this result is sensitive to the specific assumptions made about IFN production; we return to this point in chapter 7.

### 4.3.1 Recovery times and boundary lengths.

The third threshold dose,  $\nu_R \approx 0.02$  pfu/cell, is perhaps the most interesting. As the dose  $\nu$  increases, one would expect the peak percentage plaque to increase also – and, indeed, both experimental data and model output reflect this expectation (figure 4.5a). One might also expect that, as peak percentage plaque increases, so too would the recovery time. However, while the time to recovery does initially

dose	size (pfu/cell)	description
$\nu_D$	0.9	total monolayer destruction vs. eventual recovery
$\nu_I$	0.1	maximum IFN- $\beta$ production
$\nu_R$	0.02	minimum recovery time

**Table 4.1:** Critical doses suggested by modelling results.

increase with dose (and hence peak plaque), this trend fails at around  $\nu = 10^{-4}$  pfu/cell; approaching  $\nu = \nu_R$ , a sharp decrease in recovery time is witnessed. Increasing  $\nu$  further results in a second increase in recovery time, which, at  $\nu = \nu_D$ , is undefined (since recovery can not occur after total destruction of the monolayer).

The reason for this non-monotonic dependence of recovery time on  $\nu$  becomes apparent when one considers *where* regrowth occurs, namely, at the boundary between healthy cells and plaque. It is here that healthy cells divide into unpopulated regions. Time to recovery is dependent not simply on the amount of plaque that must be recovered, but also on the length of the boundary at which this regrowth can take place. Figure 4.6a on the next page shows visual representations of model output for doses  $\nu = 10^{-1}\nu_R$ ,  $\nu_R$ , and  $10\nu_R$  (labelled ①–③). Each frame is a  $360 \times 360$  cell region of a complete plate, below which the boundary length is displayed, calculated to be the total number of healthy cells in contact with at least one infected or dead cell. Also in figure 4.6 is a plot of the hours to recovery against boundary length at peak percentage (scaled by a positive constant factor so that the two may easily be compared): the maximum boundary length at peak percentage plaque coincides with the minimum recovery time.

As  $\nu$  increases, the number of plaques increase, but, because of the infection-suppressing action of IFN- $\beta$ , each plaque is smaller, so that the resulting boundary is longer. Further increasing  $\nu$  leads to a corresponding further reduction in the size of each plaque, but now there are so many that overlapping of the plaques results in a greatly decreased boundary length – there are no longer enough healthy cells to promote a rapid recovery.

This relationship between the number and size of plaques in a dish and the total boundary length of the plaques is explored via a simple analytic model below.

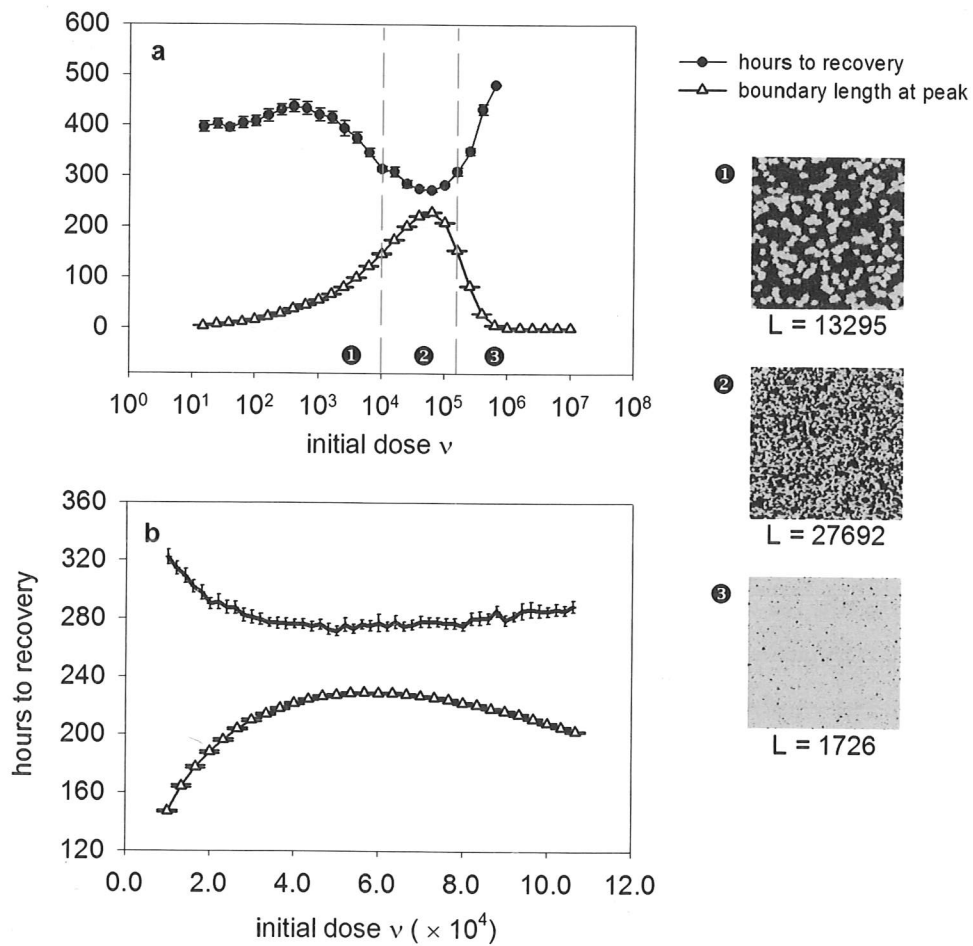


**Figure 4.6:** Recovery time against boundary length for infections of **a**  $10^1 - 10^7$  pfu; **b**  $10^5 - 10^6$  pfu. Shown to the right of **a**: visual representations of model output. Models were run until the percentage plaque peaked, at doses  $\nu = 10^{-1}\nu_R$  ①,  $\nu_R$  ②, and  $10\nu_R$  ③. Below each is the boundary length  $L$ , calculated to be the total number of healthy cells in contact with at least one infected or dead cell.

## 4.4 Scattering discs and boundary lengths

We have just seen that the time taken for a monolayer to completely recover from infection is *smallest* at the dose where the plaque boundary length at peak percentage plaque is *largest*. This is because it is at the boundary that healthy cells (in the model) can divide and repopulate the regions of dead cells next to them.

To investigate how expected plaque boundary length varies with plaque size and number, we can abstract the problem to one of overlapping discs in the plane. Consider scattering  $n$  discs of radius  $r$  into an area  $A$ , so that the coordinates of the centre of each are uniformly distributed in their respective ranges. This is analogous to the random way that viable virions in the inoculum 'land' on the cell monolayer and begin the first round of infections which become the (approximate) centres of the resulting plaques.

Now consider a point  $x$  on the circumference of one of the discs. Ignoring interactions with the boundary of the area  $A$  (that is, ignoring the fact that portions of the circumference of scattered discs may lie outside the area), the probability that  $x$  is covered by another disc (when only one other has been placed) is equal to the probability that the centre of that second disc lies in a circle of radius  $r$  about  $x$ , i.e.

$$\frac{\pi r^2}{A}$$

Hence the probability that none of the  $n - 1$  other discs cover  $x$  is

$$\left(1 - \frac{\pi r^2}{A}\right)^{n-1}$$

This is the same for any point on the circumference, so that we can calculate the expected effective circumference (i.e. circumference of this disc not covered by any other disc) by multiplying this probability by the actual circumference,  $2\pi r$ ; finally, multiplying this by  $n$  gives us the expected total effective circumference

$$C_e(r, n) = 2\pi r n \left(1 - \frac{\pi r^2}{A}\right)^{n-1} \quad (4.1)$$

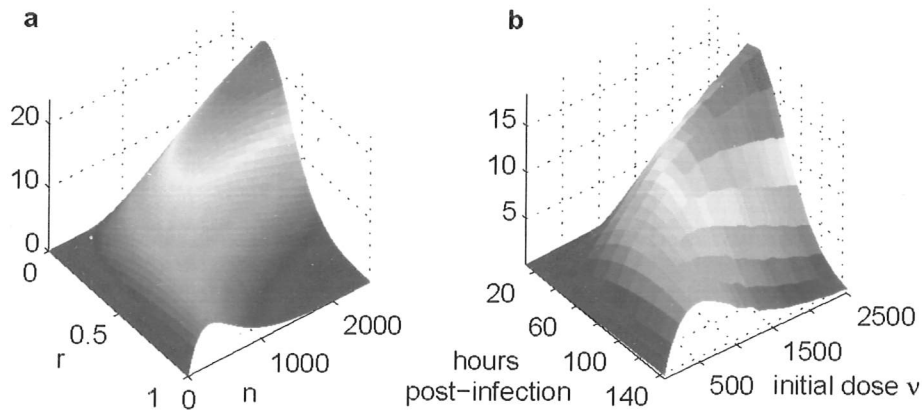


**Figure 4.7:** Analytically derived effective circumference compared against stochastic simulations of plaque boundary length. In **a**, the total effective circumference of  $n$  discs of radius  $r$  scattered in an area  $A$  has been plotted (scaled so that its form can be more easily compared with the stochastic results). In **b**, the model was used to calculate the plaque boundary area (that is, the number of cells multiplied by the area of a cell) of infection in Vero cells, in which infection progresses approximately linearly with time, at a range of pfu.

This analytic derivation can be compared against stochastically generated results (figure 4.7). The model was used to compute the total plaque boundary in Vero cells at regular time intervals and for various pfu up to 2500. The strong similarity between the analytic and stochastic results supports the analysis undertaken, and justifies the assumption that boundary effects can be ignored.

Equation 4.1 allows us to calculate the critical values of  $r$  and  $n$  at which  $C_e$  is maximal.

$$\begin{aligned} \left(\frac{\partial}{\partial r}\right)_n C_e(r, n) = 0 &\Rightarrow r_{crit}(n) = \sqrt{\frac{A}{(2n-1)\pi}} \\ \left(\frac{\partial}{\partial n}\right)_r C_e(r, n) = 0 &\Rightarrow n_{crit}(r) = -\frac{1}{\log\left(1 - \frac{\pi r^2}{A}\right)} \end{aligned}$$

These equations give the critical values for  $r$  given  $n$ , and  $n$  given  $r$ , respectively; the maximum value for  $C_e$  (allowing both  $n$  and  $r$  to vary) is unbounded as  $n \rightarrow \infty$  and  $r \rightarrow 0$ .

We can equate the number of plaques  $n$  with the dose  $\nu$ . In contrast with the analytic approximation, the plaque radius  $r$  does not vary freely, but grows in time at a rate sensitive to the IFN concentration, which is in turn affected by the dose  $\nu$ . Though this additional dependence alters the quantitative behaviour, there exists still a critical dose,  $\nu_C$  (c.f.  $n_{crit}$ ) for which the boundary length is maximal.

## 4.5 Discussion and conclusions

We have demonstrated that it is possible to capture the early dynamics of the IFN- $\beta$  response to viral infection – at least in the case of HSV-1 infection of MDBK cells – even after many simplifications and assumptions. No within-cell modelling was undertaken, so that heterogeneities in cell behaviour, such as progression of infection, were not considered. Instead, cells were treated as ‘black boxes’ onto which virions and IFN- $\beta$  bind, from which IFN- $\beta$  is secreted, and out of which new virions emerge on infection-mediated cytolysis. In addition, we assumed instantaneous diffusion of IFN- $\beta$  molecules, whereas in reality they would diffuse at finite speed according (presumably) to local concentration gradients. These limitations are discussed in more detail in chapter 7.

Despite the simplicity of the model, the results highlight a number of interesting biological issues, which prompt further study.

### 4.5.1 Behaviour of epithelial cell monolayers in vivo

This work tentatively suggests that, in the absence of the cellular components of immunity, epithelial cell monolayers recover fastest from multiplicities of infection of up to around  $10^{-2}$  (i.e. an initial dose of  $10^{-2}$  pfu/cell). At this dose, recovery time is shortest, though total IFN production has not yet peaked. From the perspective of host health, attempting to minimise recovery time and cytokine production simultaneously may be a primary consideration, as cytokines are responsible for many

of the clinical symptoms of viral infections [2, 38, 97, 106].

For intermediate virus inocula, high concentrations of IFN are produced as a result of infection, though recovery may eventually take place. In these situations *in vivo*, patches of epithelial cells suffering such widespread infection may act more as IFN producers than barriers to further infection, stimulating both the transition to antiviral states elsewhere, and a response from the cellular innate (and, later, adaptive) immune response. For high doses, total destruction is inevitable, as all cells become infected before an antiviral state can be achieved. It has been suggested that this depletion of susceptible cells itself may prove to be a major limitation for primary *in vivo* infections on epithelial monolayers, such as infection of mucosal surfaces by influenza [18, 86, 209].

The anomalous result in the MDBK 500 pfu data set (i.e. the apparent lack of antiviral state establishment and monolayer regrowth by 6 dpi – see figure 2.7) might not be an artefact of data analysis, but may instead suggest that infection can occasionally escape regulation by IFNs. To investigate this, infection in a cell monolayer must be quantified throughout its course. This would require experiments making use of non-destructive monitoring of plaques over time (rather than fixing and staining at daily intervals), such as green fluorescent protein (GFP) expression [55].

#### **4.5.2 Priming cells *in vivo***

Experimental and model results highlight the potential importance of priming of cells (that is, pre-exposure to IFN) in viral infections – greatly reduced plaque counts following IFN treatment exemplify its antiviral function (see section 4.2.4). In a host, the presence of cellular immune system components would likely increase the efficacy of priming, through amplification of IFN production, and the marshalling of leukocytes to combat virus-infected cells. For example, dendritic cells have been shown to be potent producers of IFN- $\alpha$  in response to viral infection [37, 60]; their presence would result in increased IFN concentrations throughout infection, and

therefore increased suppression of infection.

### 4.5.3 Future work

This work illustrates the dynamic nature of the interaction between viruses and the innate immune system. There is considerable scope for more work in this area, integrating laboratory approaches with theory.

The existence of (theoretical) critical dosages may prove useful in establishing the optimal dose for maximum IFN production. This technique may also be used to study other phenomenon in viral infections, such as latent infections and recrudescence of HSV. The employment of non-destructive techniques for monitoring of plaques, such as the GFP expression technique mentioned above, would capture the dynamics of plaque formation in a single tissue culture over the entire course of infection. These data sets would in turn allow more extensive parameterization and testing of the model.

One could easily adapt this work to other viruses, such as influenza; it would also provide a mechanistic spatial component for within-host models (see section 1.3). Extensions to models of this kind would require the inclusion of elements to capture the cellular and perhaps even structural responses of innate immunity (e.g. the enhanced signalling and cytokine secretion capabilities of dendritic cells, or the ciliary escalator and mucosal secretions of the upper respiratory tract); the effects of non-local virion dispersal, diffusion, and advection (which might lead to virions 'jumping' to form distinct secondary plaques) would have to be considered, and would likely have significant impact on model dynamics and the course of infection. The clearance of IFN by host mechanisms during *in vivo* infections would also effect model dynamics.

This work may be used to further explore the use of IFN in drug therapy: extensions to this work might look at viral spread in solid tissue (3 dimensions) or well-mixed

tissue<sup>2</sup> (e.g. blood), where the aforementioned 'walling off' of infection by antiviral cells becomes much harder to achieve.

Within-host models are often used to inform treatment regimens [43, 67, 86, 168]. During infection, cytokines are both crucial to the immune response, yet responsible for many of the infection's symptoms (e.g. [90]). Therefore, minimisation of cytokine production coupled with effective combating of infection would be a primary objective, and cytokine-aware within-host models may highlight courses of treatment that would best fulfil this.

Regarding the choice of model type, it is interesting to note that if spatial models of virus-immune dynamics were to be scaled up to an entire organ or host body, events taking place at the cellular level would become less important [52]. Discrete individual-based models (like that developed here) might then be dropped in favour of more course-grained ones – e.g. the analytic spatial diffusion models discussed in section 3.1. This change in approach might in any case be forced by computational necessity, as the modelling of *each cell* in a host body (or merely an entire organ) over the course of an infection would most likely require formidable computational resources.

The limit placed upon us by the power of our computers stresses an important point: at present, models at one length scale can not possibly include the complete dynamics of all the processes occurring at smaller length scales. This means that we must obtain good approximations for them instead. For example, in this modelling work, cells were treated as 'black boxes', and all processes going on at the intra-cellular level were replaced by a set of assumptions. This is often seen in epidemiological modelling, where within-host dynamics are commonly distilled down to set of discrete states (susceptible, infected, recovered).

---

<sup>2</sup>Of course, in well-mixed tissue, where all cells are essentially in contact with all other cells, the need for a spatial model is circumvented.

tissue<sup>2</sup> (e.g. blood), where the aforementioned 'walling off' of infection by antiviral cells becomes much harder to achieve.

Within-host models are often used to inform treatment regimens [43, 67, 86, 168]. During infection, cytokines are both crucial to the immune response, yet responsible for many of the infection's symptoms (e.g. [90]). Therefore, minimisation of cytokine production coupled with effective combating of infection would be a primary objective, and cytokine-aware within-host models may highlight courses of treatment that would best fulfil this.

Regarding the choice of model type, it is interesting to note that if spatial models of virus-immune dynamics were to be scaled up to an entire organ or host body, events taking place at the cellular level would become less important [52]. Discrete individual-based models (like that developed here) might then be dropped in favour of more course-grained ones – e.g. the analytic spatial diffusion models discussed in section 3.1. This change in approach might in any case be forced by computational necessity, as the modelling of *each cell* in a host body (or merely an entire organ) over the course of an infection would most likely require formidable computational resources.

The limit placed upon us by the power of our computers stresses an important point: at present, models at one length scale can not possibly include the complete dynamics of all the processes occurring at smaller length scales. This means that we must obtain good approximations for them instead. For example, in this modelling work, cells were treated as 'black boxes', and all processes going on at the intra-cellular level were replaced by a set of assumptions. This is often seen in epidemiological modelling, where within-host dynamics are commonly distilled down to set of discrete states (susceptible, infected, recovered).

---

<sup>2</sup>Of course, in well-mixed tissue, where all cells are essentially in contact with all other cells, the need for a spatial model is circumvented.

#### 4.5.4 Understanding plaque assays

The data upon which this model is built come from plaque assays of HSV infection of Vero and MDBK cells. In these experiments, using the materials and methods described in [21], it seems that plaques form in qualitatively the same way. However, in some systems plaques form in dramatically different ways, sensitive to the experimental setup. The following chapters look at one such system – plaque assays of influenza A – and attempts to identify the causes for these disparate results.

## Chapter 5

# Comet formation in plaque assays of influenza

### 5.1 Introduction

In chapter 3 we constructed a spatial stochastic model of Herpes simplex virus spread in tissue culture monolayers of Vero and MDBK cells. This model was parameterized using data collected from plaque assays. In these experiments, a layer of cells is inoculated with a suspension of virions, then incubated for several days. A viscous overlay is used to suppress long range spread of virions (by diffusion), so that, in theory, infection progresses locally. Following incubation, the regions of dead cells left behind the advancing wave fronts of infection, known as plaques, can be counted, giving a quantitative measure of the amount of infectivity in the original inoculum. More information about plaque assays can be found in section 1.4.1

However, other factors besides the properties of the virus itself may affect the dynamics of plaque formation, and it is critical to determine what these are. In the following chapters, plaque formation in *in vitro* infections of influenza A virus is studied in an attempt to understand and thereby control these non-virological factors.

This chapter begins by briefly introducing influenza, then moves on to describe the phenomenon of comet formation, and the means by which it can be quantified. The properties of comets are investigated. The existing hypotheses for cometing are described and tested; chapter 6 then moves on to look at the fluid dynamics of comet formation.

### 5.1.1 Influenza

The influenza virus is one of tremendous importance. It is an orthomyxovirus immunologically categorized by two surface proteins, haemagglutinin (H) and neuraminidase (N). Antigenic changes in these proteins give rise to new strains capable of infecting hosts previously exposed to sufficiently distantly related strains. Historically a very high profile virus, influenza has been responsible for some of the most famous and devastating epidemics in history, chief among them the pandemic of 1918.

There are three types of influenza virus: A, B, and C. Epidemics of influenza viruses A (particularly H3N2 and H1N1) and B occur most years, causing considerable mortality and morbidity, as well as being economically extremely costly: the World Health Organisation reports recent estimates of \$71–167 billion cost per year to the US economy [162]. These factors, coupled with the added threat of a reassortment between avian and human strains leading to a human pandemic of avian influenza, have resulted in influenza being the subject of intense research, from virology through to epidemiology.

In the following work, however, influenza A is not studied for its effects on public health; in fact, the virus itself is not studied at all. Rather, it is used to investigate how plaques in plaque assays form (see section 1.4.1). In particular, the focus of study will be the formation of *comets*.

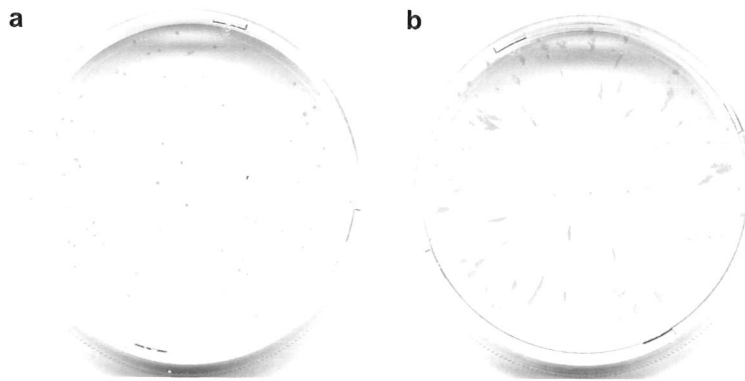


**Figure 5.1:** **a** circular plaques and **b** comets. These photographs were taken at the same time post-infection, of infections using the same viral stocks (at the same dilution), cells, materials, and basic methods. One experimental parameter was changed to move from a circular plaque regime to a cometing regime (which will be described later).

### 5.1.2 Comets

Plaque geometry (that is, the shape of plaques) varies from virus to virus and even from individual experiment to experiment. In the case of influenza, as well as many other viruses, these plaque shapes can be loosely grouped into two types: *circular plaques* and *comets*. Examples of these two types are shown in figure 5.1. Referring to this figure, we see that whereas circular plaques are the result of concentric outward growth from initial sites of infection, comets appear to streak along radii of the tissue culture dish.

While it is useful to understand the causes of and mechanisms behind comet formation, there are practical applications of immediate value for such knowledge as well. Firstly, circular plaques are much easier to count than comets (see section 2.2.2 and figure 2.6), and so it follows that the accuracy of plaque assays can be increased if comet formation can be reliably and consistently avoided<sup>1</sup>.

Secondly, and more importantly, presence and size of comets has been used to draw biological conclusions in experiments. For example, the vaccinia virus produces four

---

<sup>1</sup>Recall that plaque assays are routinely used to estimate the concentration of viable infectious units in a sample (section 1.4.1): a more easily counted set of plaques will result in a more easily acquired and more accurate estimate.

different types of virion: intracellular mature virus (IMV), intracellular enveloped virus (IEV), cell-associated enveloped virus (CEV), and extracellular enveloped virus (EEV) [190]. Extent of cometing in plaque assays of vaccinia virus has been used to quantify production of EEV [180]. If other potentially non-virological factors contribute to the presence or size of comets, these must be identified so that they can be controlled for.

### 5.1.3 Comets and modelling

More important to the field of modelling is the apparent variation in plaque size that cometing induces. It appears that not only are comets (obviously) wildly different in shape from normal plaques, but they cover a larger area. If a model of an *in vitro* or *in vivo* infection, such as that detailed in the previous chapters, is being parameterized on plaque growth data (such as percentage of monolayer covered in plaque), then we must ensure that the dynamics of plaque formation are dictated by purely virological (and immunological) factors. Without this precaution, one might incorrectly conclude (on the basis of percentage plaque coverage alone) that the virus used in figure 5.1b is more potent than that in a.

### 5.1.4 Historical suggestions for comet aetiology

Several possible explanations for comet formation have been posited (e.g. [121]): the shape or envelope of the virions; the quantity of extracellular virions being produced; convection currents in the medium moving extracellular virions; shaking, vibration, or disturbance of the cultures during incubation; or the protocols or procedures used during infection.

In this chapter we investigate the phenomenon of comet formation, its causes, and its properties. Many of the hypotheses proposed elsewhere are tested, and an attempt to identify the correct mechanism is made.

### 5.1.5 Experimental materials and methods

The materials used and methods followed for experiments performed during this work can be found in appendix B on page 135. In brief, Madin-Darby Canine Kidney cells (MDCKs) were infected with influenza A/PR/8/34 (PR8) and incubated under a medium:CMC viscous overlay.

## 5.2 Properties of comets

### 5.2.1 Direction and axisymmetry

It is natural to ask whether the size and shape of tissue culture dishes has an effect on the shape or distribution of comets. Figure 5.2 on the next page shows comets that have formed in a variety of dishes, from **a** a 6 cm dish down to **c** a 24-well cluster dish of diameter of 1.54 cm. In each of these circular geometries, comets can be seen to streak in the radial direction. Even in non-circular dishes (**d,e**), comets appear to form along lines joining the central 'spine' of the base to its edges.

The direction in which comets grow is also an important question. The answer is suggested by observation: most easily witnessed in **c**, but evident also in **a** and **b**, is the 'splaying out' of what could be termed the comet's tail as distance from the centre increases. This would suggest that infection starts in the comet nucleus (nearest the centre of the dish) and spreads (for the most part) away from the centre to form the tail. (The alternative answer, wherein widespread infection in the tail somehow converges on the nucleus over time, seems implausible.)

To test this hypothesis, comets were examined using immunofluorescent microscopy. Figure 5.3 on page 75 shows a comet photographed through a microscope and using an immunofluorescent stain for an abundant influenza virus protein, nucleoprotein (NP) – see section B.3.3 on page 137. The images have been reproduced here as negatives for clarity. Infected and healthy cells show up clearly under white light

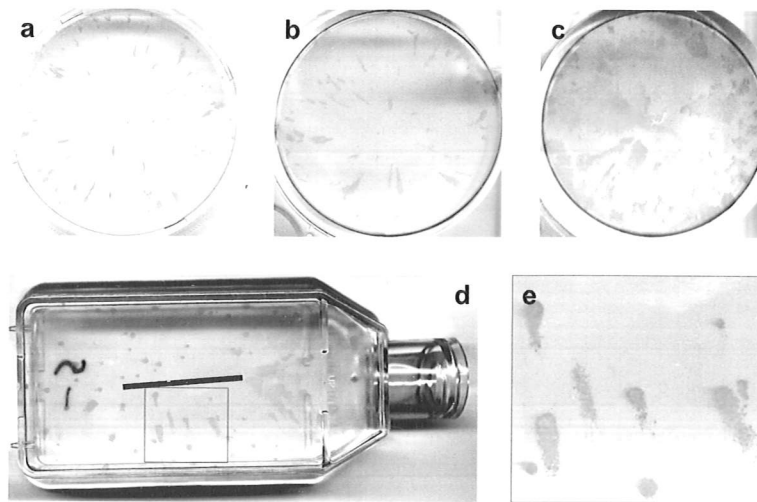


**Figure 5.2:** Comets in a variety of dishes: **a** 6 cm dish; **b** 3.37cm 6-well cluster dish; **c** 1.54 cm 24-well cluster dish; **d** T25 flask; **e** close-up (boxed in **d**) of comets in the T25 flask. In the circular wells, comets can be seen streaking in the radial direction. In **c**, the small size of the dish means that the comets appear more diffuse, since they are seen at a higher magnification. In **d**, comets appear to radiate from a line centred on the base of the flask (marked in black).

in **a**. The comet tail can be seen lying along a radius in the 6-well dish from which the image was taken, with the centre beyond the lower right corner. The immunofluorescent nucleoprotein (NP) stain in **b** shows a greater presence of NP nearer the lower right, toward the centre of the well, suggesting more advanced (i.e. older) infection there, so that comet tails must streak away from the well centre.

### 5.2.2 Extent of plaques

Looking again at figure 5.1 on page 71, it appears that when cometing occurs, a larger area of monolayer has been infected and turned to plaque: for the same initial inoculum, more cells appear to have become infected.

There are several ways to quantify this observation, and determine whether more cells are indeed infected, or whether they are simply more sparsely spread in the monolayer.

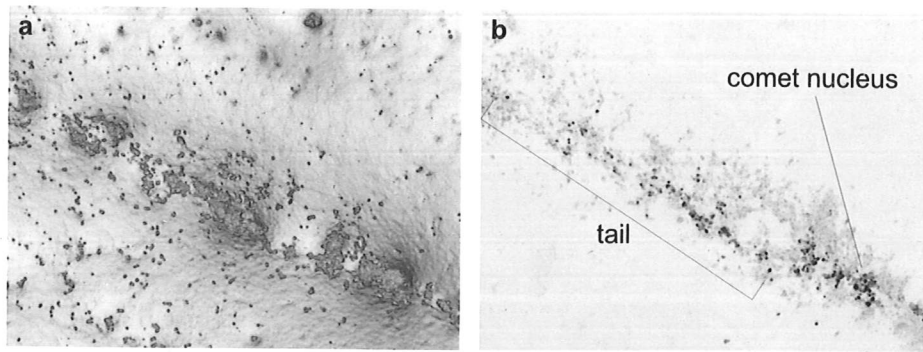


**Figure 5.3:** Microscopy of a comet. The images are shown as negatives for clarity. In **a**, healthy and infected cells are visible under white light. In **b**, an immunofluorescent nucleoprotein stain suggests older sites of infection (darker spots) in the comet nucleus compared with newer ones in the tail.

Infectious centres assays are used to approximate the number of infected (but still living) cells in a culture: that is, the number of *infectious centres*. The cells are harvested, pelleted by centrifugation, and resuspended; the suspension is then serially diluted and used to infect new monolayers in a series of plaque assays. The resulting numbers of plaques can be used to determine the concentration of infectious centres in the original cell sample, and consequently the number of infected cells (in pfu/ml).

Similarly, supernatant assays are used to approximate the number of viable virions in the medium which have been produced during infection of the underlying cell culture. The cells are harvested and centrifuged; the cells are then discarded (or used for an infectious centres assay), and the supernatant (i.e. the fluid left after centrifugation) is serially diluted and used to infect new monolayers in a series of plaque assays. As above, the resulting numbers of plaques can be used to determine the concentration of viable virions in the original overlay sample (in pfu/ml), and therefore the quantity of viable virions produced during infection.

Monolayers were infected with 500 pfu and incubated for 2 days; the cells, half of which exhibited circular plaques and the other half comets<sup>2</sup>, were then harvested,

<sup>2</sup>These experiments were performed after methodological regimes for consistent comet formation had been identified, so that comets or circular plaques could be created on demand – see section 6.5.6.

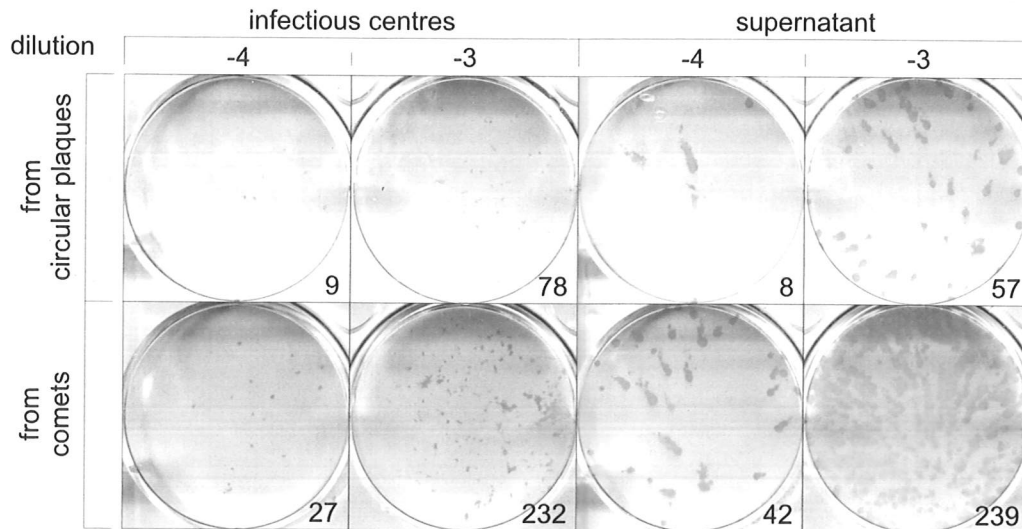


**Figure 5.4:** The plaques resulting from infectious centres and supernatant assays, showing the increased numbers of virus-infected cells and consequent increased production of virions in wells exhibiting cometing.

and infectious centres and supernatant assays performed. The results can be seen in figure 5.4 and figure 5.5. The results show that cells harvested from monolayers exhibiting comets show a roughly 3-fold increase in infected cell numbers, compared with cells from circular plaque monolayers. The supernatant assay results roughly support this conclusion, with an approximate 4-fold increase in viable virion concentration in the overlay above comets compared with that above circular plaques.

We can conclude from these experiments that cometing in plaque assays results in a greater number of cells being infected (i.e. a greater spread of virus), and hence a greater concentration of virions being released into the overlay (which itself increases the extent of infection).

### 5.2.3 Image analysis – circular plaques vs. comets

As an aside, it is perhaps natural to wonder whether the visual differences in plaque coverage between circular plaques and comets correlates with the biological differences as measured by the infectious centres assays. That is, if we measure the

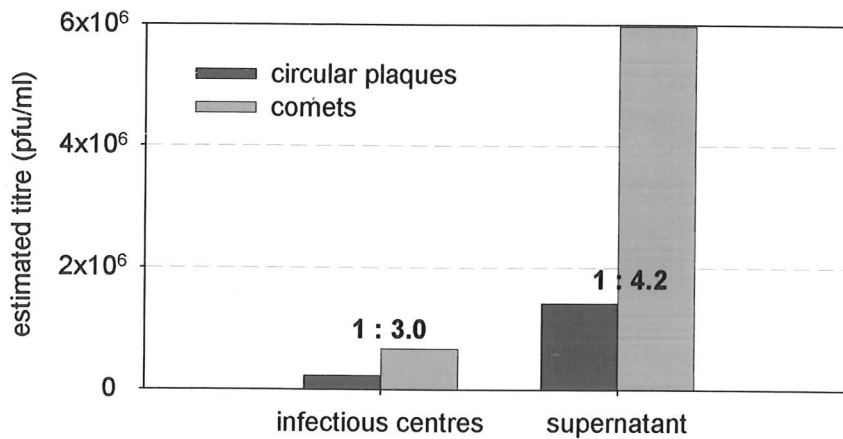


**Figure 5.5:** Estimated titre from infectious centres and supernatant assays. The estimated number of infectious cells per ml of harvested cell monolayer and estimated number of viable virions per ml of harvested supernatant were calculated from the plaque counts in figure 5.4. The ratios of the assay results for comets compared with circular plaques are also shown.

surface area of plaque for a well with circular plaques, and compare it with that for comets, will the ratio be similar to that observed in the infectious centres assay results?

The techniques developed in chapter 2 for calculating percentage plaque coverage in HSV-1 plaque assays were adapted to accommodate the transition from white-on-purple plaques to blue-on-white plaques (figure 5.6 on the next page). Thus adapted, the percentage plaque coverage for the wells shown in figure 5.4 were measured; the measurements are shown in figure 5.7 on page 79.

We see a 5-fold increase in percentage area of the dish occupied by plaque in the transition from circular plaques to comets. This is slightly greater than both the 3-fold increase in infectious centres titre and the 4-fold increase in supernatant titre witnessed in the virological assays.

This discrepancy can be explained: referring back to figure 5.3, we can see that comet tails are not homogeneously comprised of infected cells – there are many

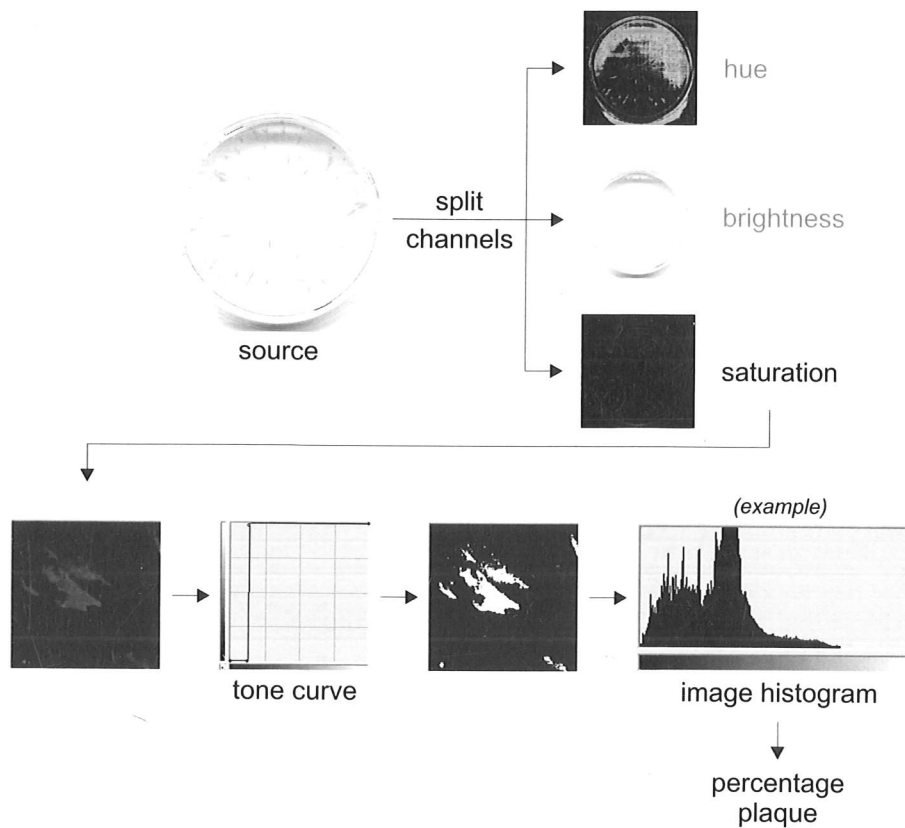


**Figure 5.6:** Image transformation technique employed to compare monolayer plaque coverage for circular plaques and comets. In contrast to the method used for the HSV data sets (figure 2.5 on page 28), the image was split into its hue, brightness, and saturation channels; the saturation channel was then tone-curve transformed and the image histogram calculated. As before, the image histogram was then used to calculate the percentage plaque in the monolayer.

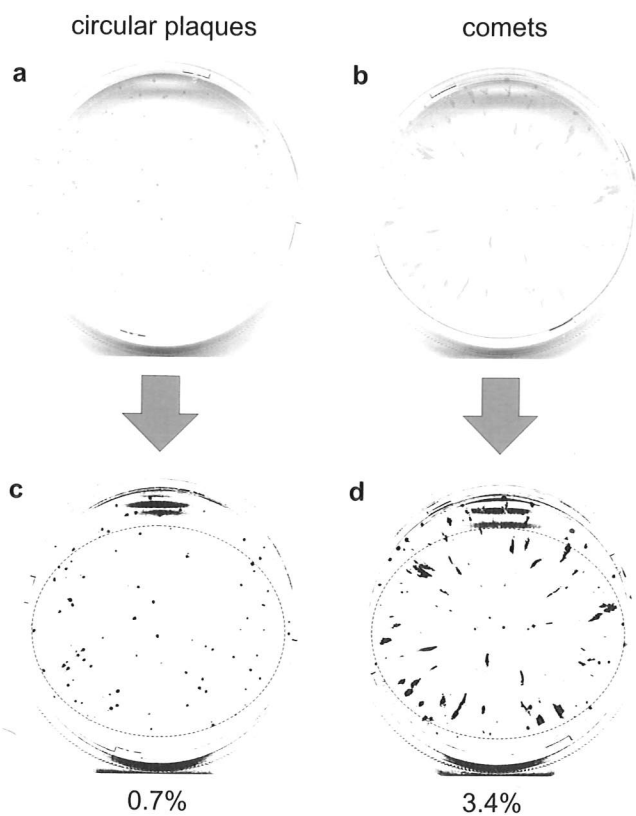


**Figure 5.7:** Image transformation results: **a** circular plaques and **c** its transform; **b** comets and **d** its transform. **c** and **d** have been shown as negatives for clarity. The ellipses in **c** and **d** denote the regions for which the image histograms were generated and plaque percentages calculated; these regions are identical in size and position, and were chosen to exclude parts of the images tainted by shadow or containing dish edges. The calculated percentages of elliptical area covered by plaque are shown under their respective images.

gaps containing uninfected cells. However, these gaps are invisible at the resolution of the images used in the image analysis technique (comet tails appear solid black after transformation – see figure 5.7d), so that the number of infected cells has been overestimated.

It is also important to note that this technique has been applied only once, so that the three computed ratios (from the infectious centres assay, supernatant assay, and image transformation results) are not statistically different from one another. However, this work demonstrates the general idea that biological conclusions (in this case the outcome of an infectious centres assay) can be drawn from photographic data of the original plates. This analysis is presented more as an idea than as a concrete technique: it must be repeated and more thoroughly tested before any firm conclusions as to its validity and wider use can be drawn.

## 5.3 Testing candidate mechanisms for comet formation

In this section we will test some of the hypotheses for comet formation, suggested either informally in discussion in the laboratory or in the literature.

### 5.3.1 Well base curvature

**Hypothesis: The curvature of the bases of the wells used for plaque assays results in the formation of radial comets.**

The radial nature of comets may suggest that a slight curvature in the base of the wells (i.e. the surface on which the cells grow) used is responsible for the extent and direction of comet formation. If the base is curved or bowed in an axisymmetric fashion, perhaps as a result of the manufacturing process (e.g. during the cooling of the plastic following injection moulding), this would give direction to whatever

process is responsible for comet formation. For example, if the well base rises toward the centre (imagine a flattened upturned bowl), then gravity might cause the remnants of dead cells which detach from the monolayer to drift downward (in the same way that epithelial cells left in suspension after seeding settle and stick to the growth surface), away from the raised centre of the well. This material may bring new virions with it, leading to the formation of comet tails that radiate outward from nuclei centred on initial sites of infection, as is observed experimentally.

### **Measuring well base curvature**

A dial gauge was used to measure the variation in 6-well depth (that is, well floor height) at fixed distances of 5 mm, 10 mm, 15 mm, and 20 mm along a pair of perpendicular diameters. Several wells, taken from several different 6-well dish clusters, were measured. The mean difference between the well depth at the edge and at these various distances is shown in figure 5.8 on the next page. From this, we can conclude that the bases of the wells are not flat, and do indeed resemble the up-turned bowls hypothesized above.

The variation in well depth, of just over 0.1 mm across a radius of  $\approx 17$  mm, is very small, so it seems unlikely that curvature is responsible for comet formation. Two further experiments were performed to rule out this hypothesis more substantively.

### **Tilting the wells**

If gravity is playing a role in the formation of comets, acting through the gradients created by well base curvature, then tilting the wells should change the 'focus' of the comets, i.e. the apparent centre from which they radiate (see figure 5.9 on page 83).

By inputting the base deviation measurements into mathematics software [208] and fitting a smooth curve to the data<sup>3</sup>, contour maps of the well base can be generated.

---

<sup>3</sup>In this case, a zero-order Bessel function was used – however, any smooth curve would have

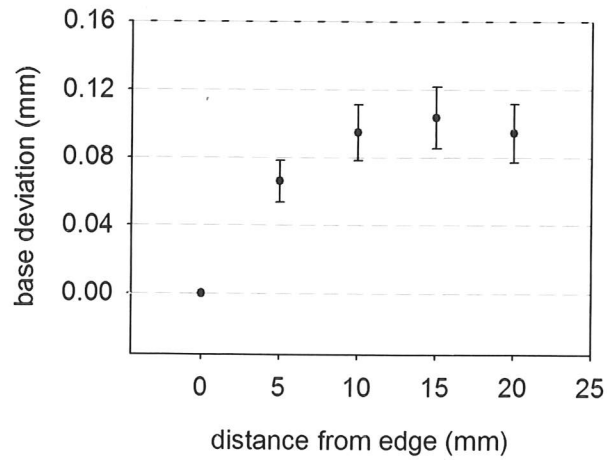


**Figure 5.8:** Variations in 6-well depth. A positive deviation indicates that the well has become shallower, i.e. that the base has risen. The graph therefore shows a (stretched) representation of the cross section of the growth surface of a well. Mean values were calculated from 4 measurements in each of 6 dishes (2 dishes taken from each of 3 different 6-well clusters). Error bars are 95% confidence intervals for the mean.

Contour maps for a well placed horizontally (**a**), as well as for those tilted at various angles (**b-d**), can be seen in figure 5.10 on the next page.

---

sufficed.

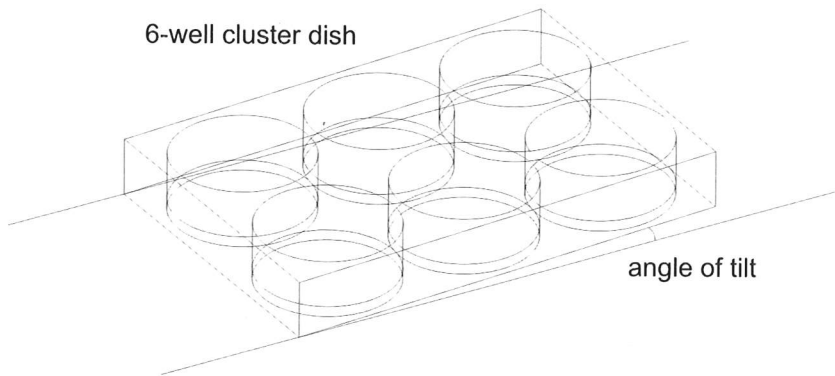


**Figure 5.9:** 6-well clusters may be tilted for the duration of incubation.

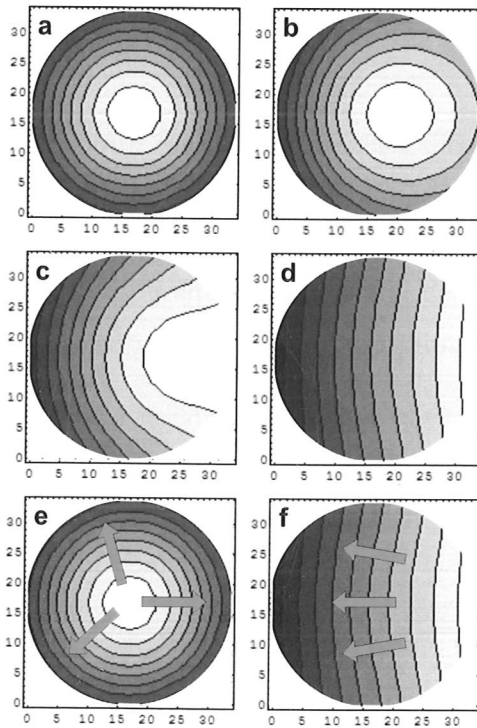


**Figure 5.10:** Contour plots of the base of a well tilted at an angle of **a**  $0^\circ$ ; **b**  $0.2^\circ$ ; **c**  $0.5^\circ$ ; and **d**  $2.7^\circ$ . In **e** and **f**, orange arrows indicate paths of steepest descent in a flat well and one tilted at  $2.7^\circ$  respectively. The right hand edge of each well is uppermost.

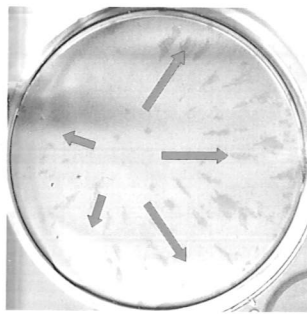


**Figure 5.11:** Resulting plaques after tilting a 6-well cluster by  $2.7^\circ$  throughout incubation. The right hand edge of the well was uppermost during incubation. The orange arrows indicate the apparent local direction of comet tail formation.

The orange arrows in figure 5.10 on the preceding page indicate steepest descent paths for **e** the growth surface of a flat well, and **f** a tilted well<sup>4</sup>. The radially outward paths of the flat well correspond to the radially outward formation of comets. If this is indeed the mechanism behind comet formation, then a well tilted as in **f** should exhibit comets forming in that direction.

Experiments were performed with 6-well cluster dishes tilted at  $2.7^\circ$  during incubation (but not infection, as that would have lead to a markedly uneven distribution of plaques which may have obscured the outcome). This tilt is small enough that the depth of the medium is not greatly altered, and is still deep enough at the 'shallow end' to maintain cell vitality. An example of the resulting plaques can be seen in figure 5.11.

These results are at odds with predictions based on the tilted contour map in figure 5.10e, suggesting that base curvature, at least through the action of gravity, is not responsible for the direction of comet formation.

(While not supporting the hypothesis that dish curvature dictates the radial formation of comets, figure 5.11 does suggest that the focus of the comets has moved (slightly leftward of centre). Further work indicated that this is a result of the overlay depth changes precipitated by tilting; such overlay depth effects are investigated

<sup>4</sup>The angle of tilt,  $2.7^\circ$ , may seem somewhat arbitrary, but it in fact corresponds to raising one end of the 6-well cluster by 5 mm.

in the next chapter.)

It is important to note that these results are not at odds with those reported in [121], where tissue culture dishes were tilted at  $10^\circ$  during the 2-day incubation period in vaccinia virus infection of RK<sub>13</sub> cells and the resulting plaques streaked upward against gravity: we have only ruled out well-base curvature effects in the formation of comets.

### Plaque assays on cover slips

If not through the action of gravity, where matter containing or entraining new virions is 'dragged' down slopes by gravity, then how might base curvature effect comet formation? Alternatively, how could surface curvature be completely ruled out as a mechanism?

To attempt to answer this, glass cover slips, found to be absolutely flat (to within the accuracy of the dial gauges used), were overlaid on the growth surfaces of 24-well clusters prior to seeding. These clusters were chosen (rather than the more usual 6-wells) as cover slips of the required size were available, i.e. such that they almost covered the bottom of each well. In this way, the growth surfaces are rendered effectively flat. Plaque assays were then performed as normal. An example of the results is shown in figure 5.12.

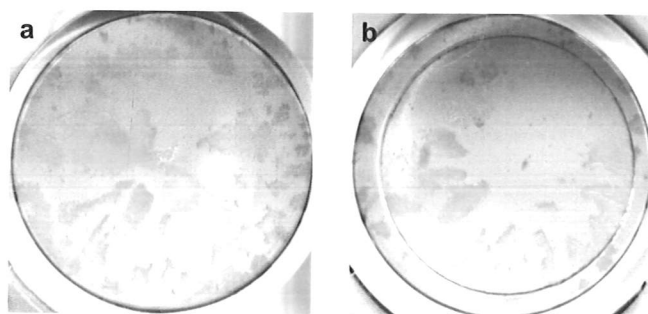


**Figure 5.12:** Plaque assays in 24-well clusters: **a** without a cover slip; **b** with a cover slip. In each case, radial comets can be seen.

## Conclusion

The presence of radial comets on the cover slip essentially the same as those on uncovered well bottoms, together with the results from the tilting experiments, strongly suggests we reject the hypothesis that well surface curvature results in radial comet formation.

### 5.3.2 Concentration gradients

**Hypothesis: a concentration gradient of an infection promoter or inhibitor in the overlay results in radial comet formation.**

The spontaneous formation of patterns in microbial cell cultures, such as that seen in figure 5.13, has been widely studied (for example [68, 130]).

The formation of such patterns in this case relies on:

- the presence of gradients in concentration of nutrients (or other promoters or

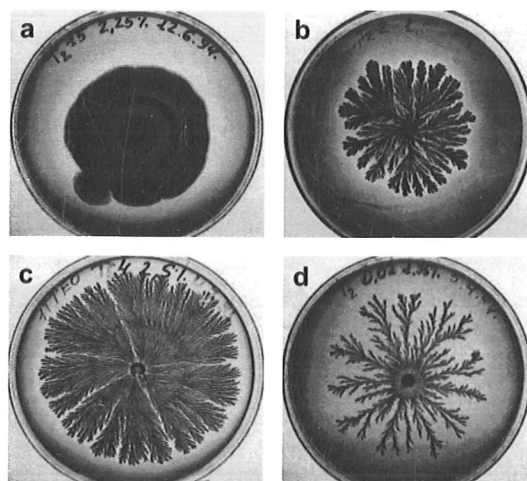


**Figure 5.13:** Pattern formation in bacterial colonies (photographs from [24] via [65]). Gradients in nutrient and substrate concentrations result in colonies branching in mathematically well-defined ways. Nutrient concentration starts at a high of 15 g/l in **a**, and decreases to 0.01 g/l in **d**.

inhibitors of growth);

- the ability of bacterial cells to sense these gradients and move along them (a process known as *chemotaxis*).

The patterns observed in figure 5.13 on the preceding page are generated by bacterial colonies spreading from a single point of infection near the middle of the dish. As local supplies of nutrient are depleted the bacterial cells will move outward, dividing as they do so. For high nutrient concentrations, bacteria need not chemotax far to find resources, resulting in dense (even contiguous) colonies (seen in **a**). For decreasing nutrient concentrations, the resulting patterns becoming increasingly sparse as the colony must spread out more to support a given number of cells (**b-d**).

While this may initially seem to be a plausible explanation for comet formation in plaque assays, the following points suggest that it not be accepted:

- i. **Virions do not exhibit motility.** Unlike the bacteria mentioned above, virions are unable to exert control over their motion – they can not move in response to a concentration gradient, or indeed any other stimulus. (There is, however, evidence that viruses can induce motion in the cells they infect: specifically, vaccinia virus has been shown to possess this ability [183].)
- ii. **Radial symmetry, overlap of comets implies no local concentration gradient.** The radial symmetry seen in the bacterial colonies of figure 5.13 is a direct result of the placement of the single initial point of infection in the centre of the well (the founding bacterium or bacteria of the colony). Conversely, in the plaque assays under study here, initial infection foci are randomly distributed, and yet comets still streak away from the middle of the well, rather than away from the nearest comet nucleus. In addition, if comet tails are streaking away from some substance (or towards it) along a concentration gradient, one would expect nearby comet tails to behave likewise i.e. a tail of one comet would not grow through the head of another – yet comets are routinely seen to merge with or overlap other comets.

iii. **No global concentration gradient.** The low viscosity of the overlay makes it impossible to maintain steep gradients in the concentration of any promoter or inhibitor of infection. Inhibitors or suppressors of viral infection (such as IFN) could be produced locally, but such substances would likely diffuse much too quickly to sustain the steep local gradients required for the pronounced streaking of plaques observed in experiments. Indeed, one of the assumptions of the HSV stochastic modelling work covered in the previous chapters was that IFN diffusion in plaque assays can be approximated as instantaneous over the time scales being considered (hours).

## **Conclusion**

For the reasons detailed above, it seems that infection promoter/inhibitor concentration gradients are an unlikely explanation for comet formation.

### **5.3.3 Environmental disturbance**

**Hypothesis: physical disturbance or vibration of wells during incubation results in comet formation.**

For the duration of infection, cells are kept in incubators. In most laboratories, including the one in which the experiments detailed in this work were undertaken, incubators are in constant use by many researchers concurrently.

Environmental factors, such as disturbance of wells inside the incubator, jolting or shaking caused by the opening of the incubator door, or vibration from incubator machinery, may play a role in comet formation. Such disturbance may give rise to axisymmetric standing waves. These have been documented in the literature (see, for example, the numerical solutions for inviscid flows presented in [200]); a simple schematic of these waves is shown in figure 5.14 on the next page.

While it may be possible to initiate such waves in the overlay for short periods of time through accidental disturbance or environmental vibration, virion spread by an alternating inward-outward flow of this kind does not appear to account for the unidirectional formation of the comet tail.

A series of experiments were performed to more thoroughly test the hypothesis: a water bath was employed to incubate cells throughout infection, rather than a standard incubator. After seeding and infection, wells were placed in a sealed container, which was then gassed to contain a 5% CO<sub>2</sub> atmosphere. The container was submerged in a water bath at 37°C for the 2-day incubation period. This water bath was set aside specifically for these experiments, so that the physical disturbances and large water temperature variations that may have resulted from the opening of, removal from, or addition to the water bath could be excluded. All other experimental parameters were kept constant. Figure 5.15 on the following page shows the resulting plaques, shown alongside ones developed inside a standard incubator.

### High frequency low amplitude vibration

Environmental disturbance may drive comet formation in another way: high frequency low amplitude vibration of the wells (caused by, for example, ventilation fans or other electrical components inside the incubator) might give rise to flows in the overlay. Let us assume that such vibrations of the well may be approximated by

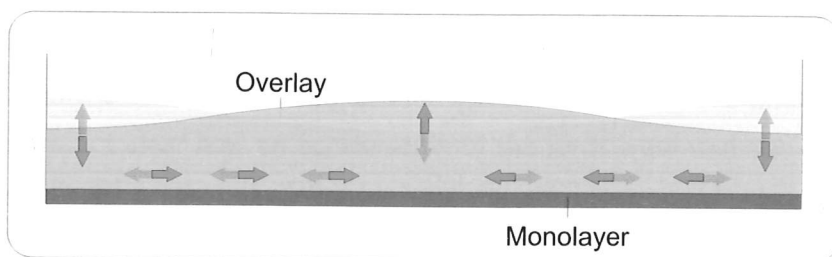


**Figure 5.14:** A schematic of axisymmetric standing waves in a well. Such waves would result in radially outward and inward flow immediately above the monolayer, which would lead to the spreading virions in a radial direction.

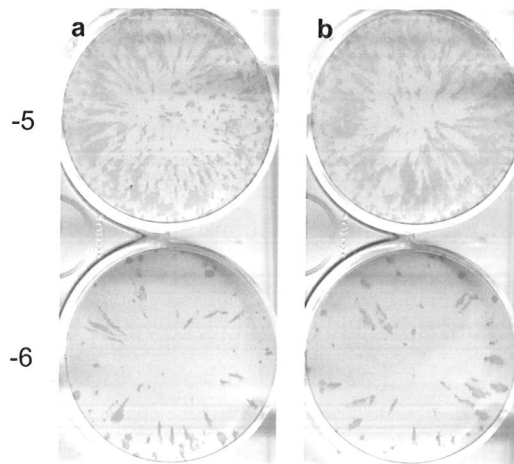


**Figure 5.15:** Comets in plaque assays performed in **a** a dedicated water bath compared with **b** those performed in an incubator.

rigid vertical displacement  $a \cos(\omega t)$ . Then the  $y$  coordinate of a point in the well in the incubator's reference frame,  $y_{inc}$ , is given by

$$y_{inc} = y_{well} + a \cos(\omega t)$$

The corresponding acceleration is

$$\ddot{y}_{inc} = \ddot{y}_{well} + a\omega^2 \cos(\omega t)$$

so that we have introduced an acceleration of magnitude  $a\omega^2$  into the system. This nonlinear dependence of acceleration on frequency means that for high frequencies (such as the  $\omega = 50\text{Hz}$  of mains electrical equipment), even very small amplitude vibrations could result in overlay motion, which may in turn lead to comet formation.

This argument is clearly very simple, and leaves many questions unanswered. For example, it is not clear how an acceleration of the form presented above would lead to rectified flow i.e. sustained flow in a preferred direction, which appears to be required for the formation of comets. More detailed mathematical and experimental investigation would be required to rule out or confirm this effect as the cause of comet formation.

## **Conclusion**

Comets of similar lengths and shapes were observed (and this observation confirmed by comet measurement), independent of choice between incubator and water bath, indicating that low frequency environmental disturbances (at least those introduced by use of an incubator) are not a factor in the formation of comets. High frequency vibration of the wells may, however, play a role: this possibility warrants further mathematical and experimental investigation.

## **5.4 Conclusion**

In this chapter we have tested several hypotheses for the mechanism underlying comet formation. While none of them have been accepted, the investigation, and in particular the notion that overlay flow may lead to cometing, has suggested the next avenue of study. In the following chapter, the idea that cometing is driven by fluid flows in the overlay is investigated more thoroughly.

## Chapter 6

# A fluid dynamic mechanism for comet formation

### 6.1 Introduction

In this chapter we will investigate the hypothesis that comet formation is driven by overlay flow during incubation.

Looking at typical comets, such as those in figure 6.1 on the next page, it appears that virions are being 'smeared' across the monolayer by a flow in the overlay: picked up after release in the comet nucleus and deposited a short distance away to form the tail. These secondary infections give rise to new releases of virions, which themselves are carried downstream to continue tail formation. The strong radial nature of comet formation noted in the last chapter suggests that the flow must be radially outward just above the monolayer, and, to conserve overlay volume, radially inward at the surface of the overlay – figure 6.2 on page 94 shows a schematic of this flow.

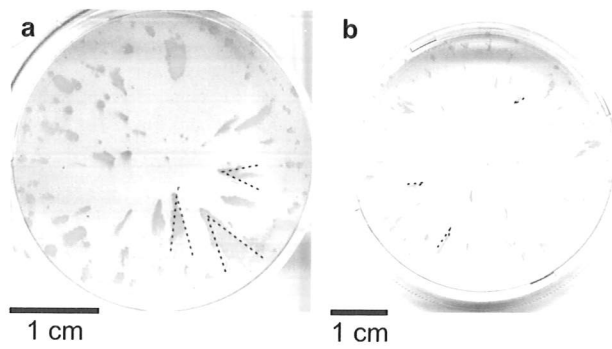


**Figure 6.1:** Spreading of comet tails with distance from the nucleus. The overlay spreads out as it leaves the centre, widening the comet tail as it goes. This effect is not observed to the same extent in **b**, as the dish has a larger radius than that in **a** (26.5 mm instead of 16.85 mm), so that the widening along the length of a comet is reduced.

### 6.1.1 Further evidence of radial flow

#### Widening of comet tails

Two pieces of further evidence for such a flow can be gleaned from the images, without performing additional experiments: firstly, comet tails widen as they lengthen, which is consistent with a radial flow spreading outward from the centre of the well (see the dotted wedges drawn in figure 6.1).

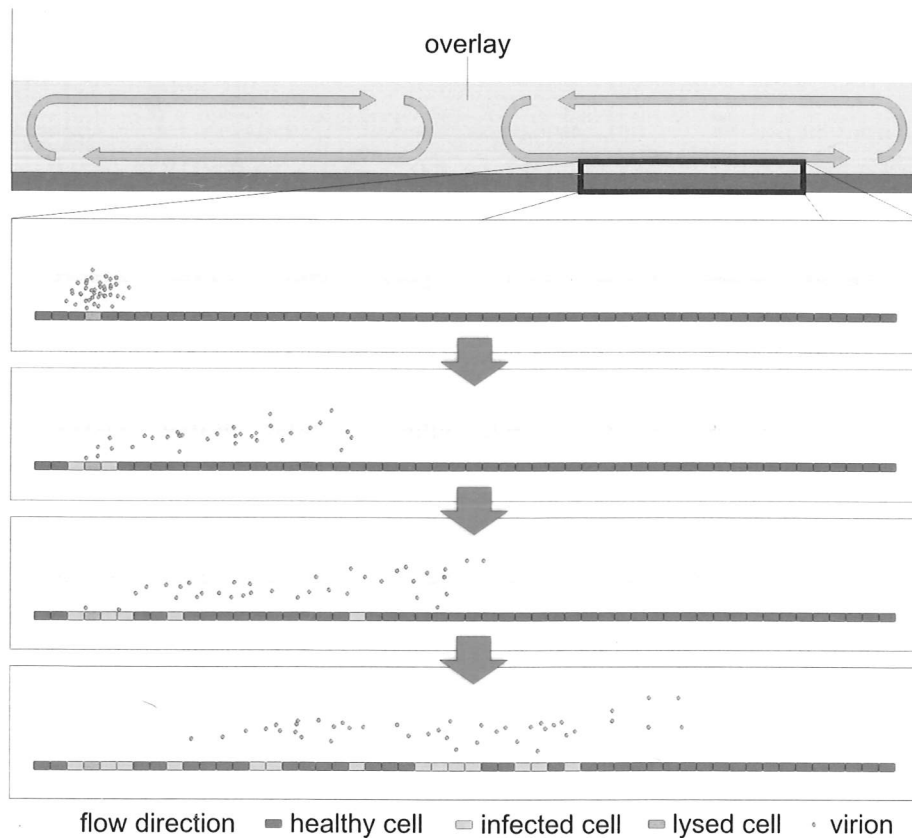


**Figure 6.2:** Fluid dynamic mechanism for comet formation. A flow in the overlay which is radially outward at the monolayer picks up virions from above newly lysed cells. These virions travel downstream and are deposited to create new 'islands' of infection in what will develop into the comet tail. The aspect ratio is not drawn to scale: 6-well dishes are approximately 33 mm wide, and the overlay depth varies between 2 and 5 mm.

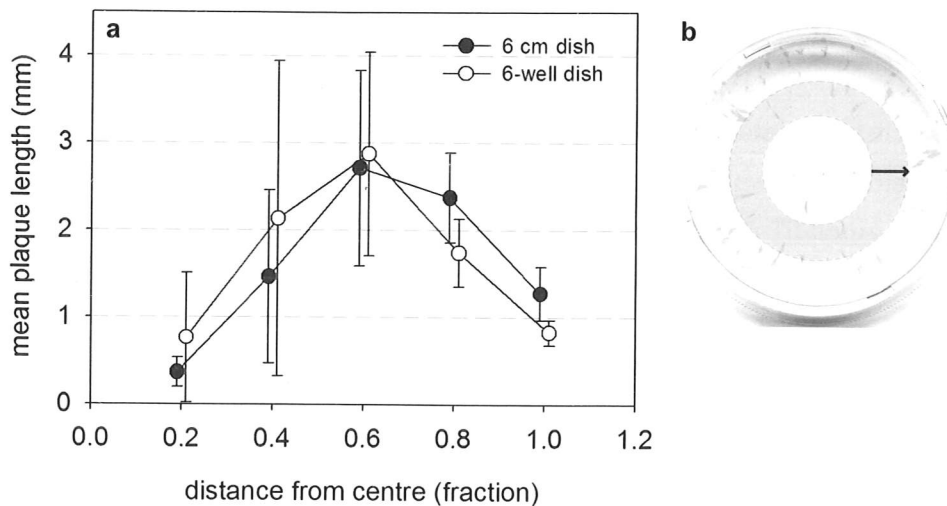


**Figure 6.3:** Mean plaque length against radial position. The mean plaque length was calculated for comets originating in progressively wider annuli (see **b**) centred on the middle of the well for 6 cm dishes and 6-well dishes. The images were taken from experiments that exhibited similar maximum comet lengths. Mean values were calculated from measurements of all comets in each of the 5 defined annuli for two dishes of each size. Error bars are 95% confidence intervals for the mean. For each of the two dish sizes, the error bars for the measurements at radii of 0.2 and 1 (either end) do not overlap with those at a proportional radius of 0.6. This indicates that there is a statistical difference (at the 0.05 level) between the lengths of comets that form near the edge or centre of a dish and those that form at intermediate radii.

### Radial dependence

The second piece of evidence is the dependence of comet length on the distance of the nucleus from the centre of the well. If a fluid flow of the form sketched in figure 6.2 is responsible for comet formation, one would expect that the horizontal flow is fastest furthest away from the turning points in the flow, i.e. away from the centre of the well and the edge of the well, at intermediate radii. The graph in figure 6.3 shows the dependence of comet length on distance of comet nucleus from well centre, calculated from measurements taken from several different experiments. It is clear from this that the longest comets do indeed form at intermediate radii.

### 6.1.2 Speed of the flow

In the experiments performed for this work, the longest comets grew to around 1.5 cm long (see figure 5.2) in 48 hours of incubation. Even allowing for the length of the virus life cycle (which for PR8 in MDCK cells is between 6-10 hours [201]), this results in a maximum average flow speed of  $\approx 10^{-7} \text{ ms}^{-1}$ .

### 6.1.3 Assumptions, boundary conditions, and the flow profile

There are three boundaries to the overlay flow hypothesized for comet formation: the bottom of the well, the sides of the well, and the (essentially) free surface where the overlay meets the atmosphere of the incubator. The medium used in these experiments is considerably more viscous than water, and, importantly, can certainly *not* be regarded as inviscid. Therefore, at the bottom and sides of the well (which are rigid), the *no-slip condition* applies: tangential and normal components of the flow field  $\mathbf{u}$  are zero i.e.  $\mathbf{u} = \mathbf{0}$  on the boundaries of the flow.

Like many liquids, the overlay can be thought of as incompressible, so that  $\nabla \cdot \mathbf{u} = 0$ . The free surface is flat except for meniscus effects at the edge, which suggests that surface tension does not play a role in the boundary conditions at the liquid-gas interface. Therefore, at the free surface (with normal and tangential unit vectors  $\hat{\mathbf{n}}$  and  $\hat{\mathbf{t}}$  respectively), the boundary conditions are

$$\begin{aligned} e_{ij} \hat{\mathbf{t}}_i \hat{\mathbf{n}}_j &= 0 \\ p - 2\mu (e_{ij} \hat{\mathbf{n}}_i \hat{\mathbf{n}}_j) &= p_0 \end{aligned} \quad (6.1)$$

where  $e_{ij} = \frac{1}{2} \left( \frac{\partial u_i}{\partial x_j} + \frac{\partial u_j}{\partial x_i} \right)$  is the strain tensor for the flow  $\mathbf{u}$ . In cylindrical polar coordinates, the first of the conditions in equation 6.1 becomes

$$\frac{\partial u_r}{\partial z} = 0 \quad \text{at } z = h \quad (6.2)$$

These conditions lead to the *qualitative* profile suggested in figure 6.4.

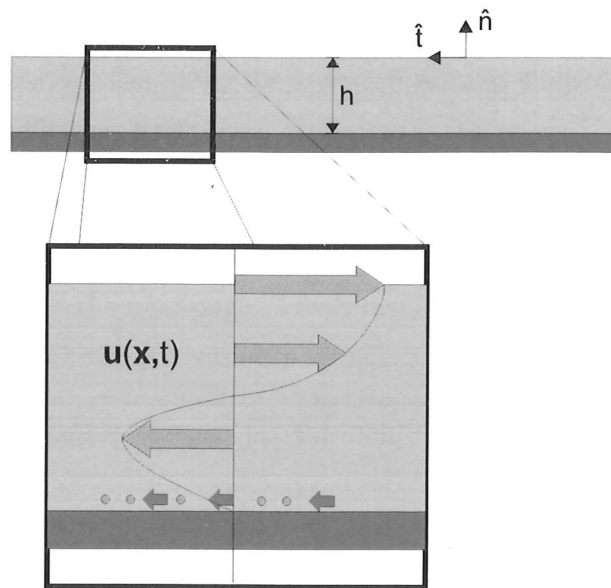


**Figure 6.4:** Hypothetical comet-forming flow profile suggested by boundary conditions and experimental evidence.

### 6.1.4 Conclusions

If this hypothesis is correct, and a radial flow in the overlay is behind comet formation, changing the bulk properties and extent of the overlay should alter the properties of the flow, and concomitantly the characteristics of the observed comets.

## 6.2 Investigating the flow

In this section we investigate the fluid dynamic hypothesis described above.

### 6.2.1 Overlay depth

The first overlay property to be investigated was the depth. After seeding and infection, inoculum was aspirated off, and the overlay added to varying depths: 2 mm, 3 mm, 3.5 mm, 4 mm, 4.5 mm and 5 mm. A depth of 2.2 mm corresponds

to an overlay volume of 2 ml (the standard quantity used in all other experiments). After 2 days incubation, the monolayers were fixed and stained, and are shown in figure 6.5 on the following page.

The length of each plaque or comet (i.e. diameter of the smallest circumscribed circle containing the plaque) was calculated for each of the wells; these are also shown in figure 6.5 on the next page. These results indicate that overlay depth has a significant impact on the formation of comets.

There are several possible reasons for the depth dependence witnessed in comet formation.

- The flow profile outlined in figure 6.6 on page 100 may be 'stretched' as the depth increases. Altering the overlay depth changes the aspect ratio of the flow, in turn changing the height above the monolayer at which the maximum outward flow speed occurs (see figure 6.6 on page 100).
- The velocity of the comet-forming flow is constrained by the balance between the energy input into the system<sup>1</sup>, and that lost through (among other things) viscous dissipation in the fluid motion. For a given motive force responsible for maintaining overlay flow, a greater volume of fluid will necessarily result in a lower average flow velocity.

These will be further discussed later in the chapter.

### 6.2.2 Overlay viscosity

In the same vein as the energy conservation argument proposed above, it should follow that as viscosity increases, so too does the viscous dissipation of energy, thereby decreasing the maximum flow velocity. Put simply: a thicker overlay will flow more slowly, resulting in shorter comets.

---

<sup>1</sup>Of course, it remains to be determined precisely the mechanism driving the flow, i.e. what the source of energy is.

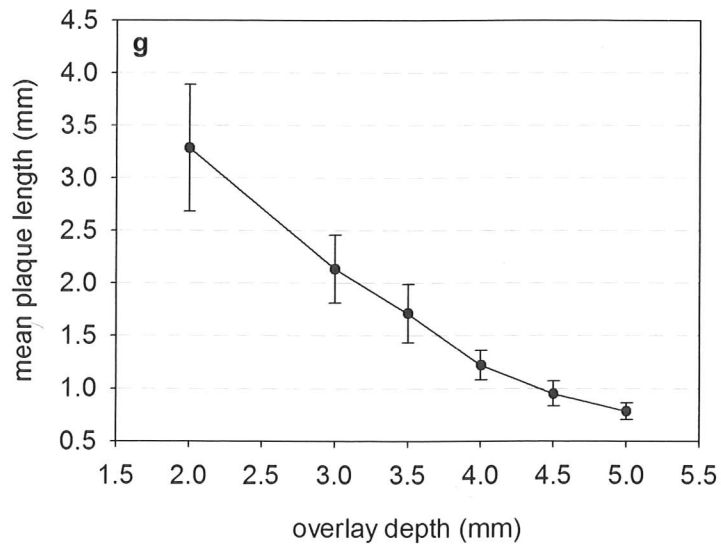
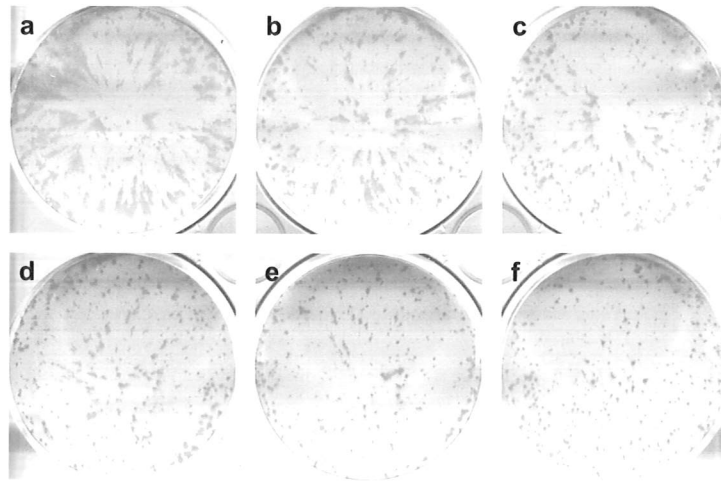


**Figure 6.5:** Results of varying overlay depth. An inoculum titre of 500 pfu was used. Overlay depths of **a** 2 mm; **b** 3 mm; **c** 3.5 mm; **d** 4 mm; **e** 4.5 mm; and **f** 5 mm. The resulting graph of mean plaque length against overlay depth is shown in **g**. Mean values were calculated from measurements of all comets in a dish (or randomly determined half-dish for large plaque counts) from each dish in two experiments. Error bars are 95% confidence intervals for the mean.

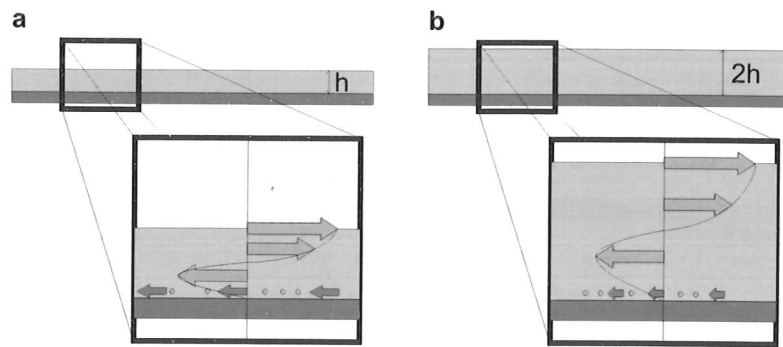


**Figure 6.6:** Hypothetical comet-forming flow profiles at different overlay depths. The flow profile for an overlay depth  $h$  in **a** is stretched to a depth  $2h$  in **b**. Consequently the virions are swept up in a slower flow, leading to shorter comets.

Carboxymethyl cellulose (CMC) is routinely included in the overlay for plaque assays to suppress long range diffusion of virions, allowing more clearly defined plaques to form (an understandable requirement in plaque assays, which usually rely on being able to identify and count each one). At typical concentrations it is a viscous thermo-reversible gel, and, because of its universal non-toxicity, is widely used as a gelling and thickening agent (for example, as food additive E466 [1]).

In the laboratory it is prepared by adding equal quantities of so-called 'high viscosity' and 'low viscosity' powders (Sigma Co., Surrey, UK) to a combination of phosphate-buffered saline (PBS) and reverse osmosis (RO) water<sup>2</sup> (see section B.3.4 on page 138). To make CMC preparations of different viscosities, the ratio of high to low viscosity powders was changed. CMC using ratios of 5:1, 2:1, 1:1, 1:2, and 1:5 were made using the above method. Overlays made with these CMC preparations were used in place of the standard one (to a depth of 3 mm); as a control a sixth well was overlaid with the laboratory-prepared CMC used in all other plaque assays. The resulting plaques (after infection, incubation, fixing, and staining as normal) can be seen in figure 6.7 on page 102. As before, the mean plaque length was calculated for each of the wells; the specific viscosity<sup>3</sup> of each of the overlay preparations was

<sup>2</sup>Reverse osmosis is a process by which contaminants are removed from water, resulting in a sufficiently high purity for use in sterile laboratory environments.

<sup>3</sup>The specific viscosity of a liquid is a normalised comparison between the viscosity of the liquid and that of water (or some other solvent) – see figure B.1 on page 139 for more information.

measured using an Oswald's viscometer (see figure B.1 in appendix B on page 139), and mean plaque length has been plotted against these measurements (also shown in figure 6.7).

These results support the theory of a fluid dynamic mechanism underpinning comet formation: a higher viscosity leads to reduced flow speed and therefore shorter comets.

### 6.2.3 Baffles

In the hypothetical comet-forming flow (figure 6.2 on page 94), fluid moving radially outward in the lower half of the monolayer must return in the upper half. Inserting a baffle into the upper half of the overlay (figure 6.8a on page 103) should disrupt the flow while still allowing diffusion of compounds and motion of virions throughout the overlay, ensuring that the baffle is affecting only fluid dynamic properties of the overlay.

Small polystyrene blocks were affixed to the lid of a 6-well cluster above each well. Slits were made in each block so that glass cover slips, cut to the appropriate width and height, could be inserted and held in place. The slips were adjusted in their holding blocks so that their lower edge rested 1 mm above the well base on replacement of the 6-well cluster lid (figure 6.8b). In a parallel series of experiments, cover slips were fixed across a chord of each well, positioned 1 mm above the base of the well as before (figure 6.8c).

The wells and cover slips were thoroughly washed in 70% ethanol (to minimize the risk of contamination) and allowed to dry. Plaque assays were then performed as normal, with the overlay added to a depth of 2 mm for incubation, so that the baffles disrupted only the upper half of the overlay.

Results from these experiments can be seen in figure 6.9 on page 104. The presence of the baffles is represented by the dashed lines – it is clear that their presence has had a significant effect on comet placement in all cases. A comparison between

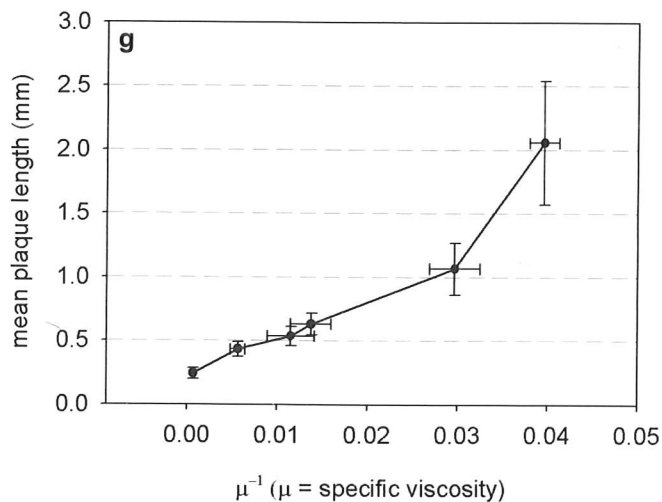
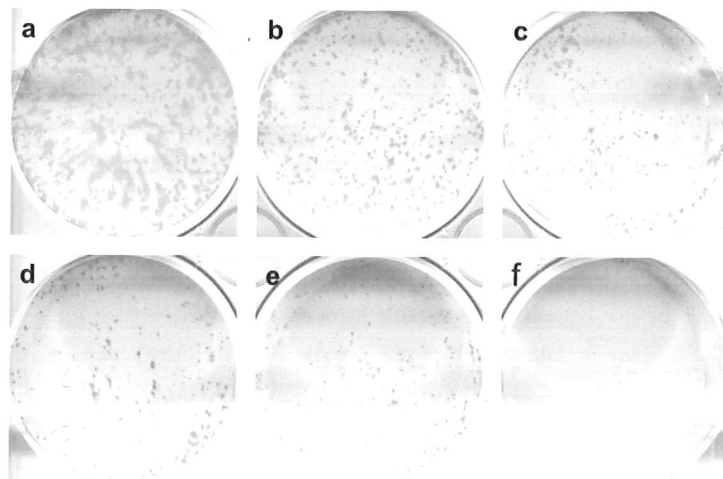


**Figure 6.7:** Results of varying overlay viscosity. An inoculum titre of 500 pfu was used. Overlays using CMC prepared with high:low viscosity powder ratio of **a** 1:5; **b** 1:2; **c** 1:1; **e** 2:1; **f** 5:1; **d** used pre-prepared CMC. The resulting graph of mean plaque length against overlay specific viscosity is shown in **g**. Mean values were calculated from measurements of all comets in a dish (or randomly determined half-dish for large plaque counts) from each dish in two experiments. Error bars are 95% confidence intervals for the mean.

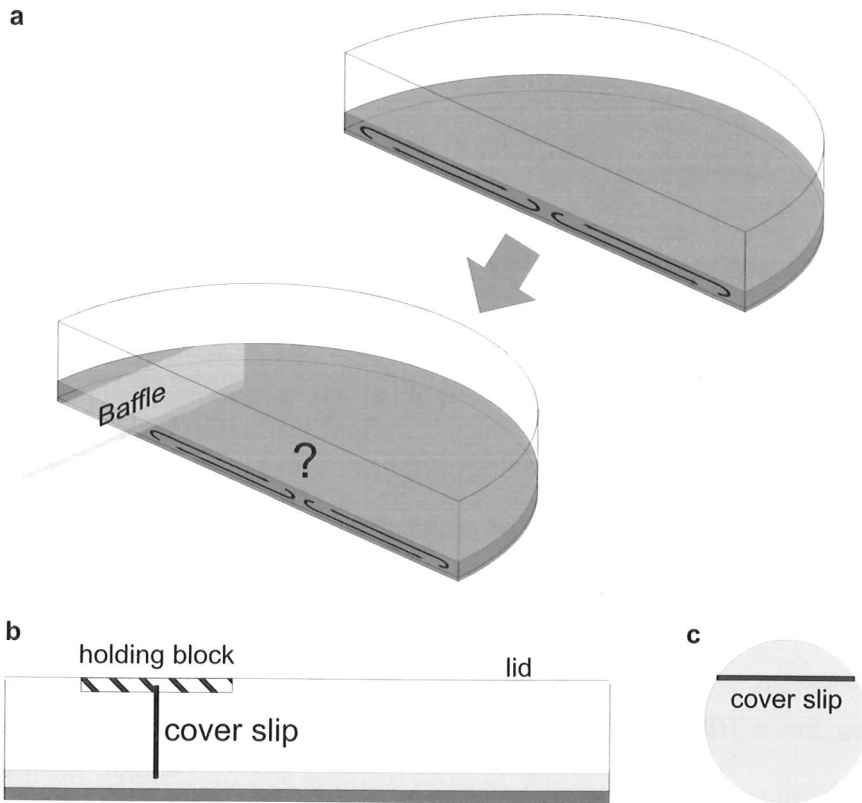


**Figure 6.8:** Insertion of a baffle into the overlay. **a** inserting a baffle into the overlay should disrupt the comet-forming flow. In a range of experiments, baffles were affixed to **b** the lid, or **c** the sides of the well.

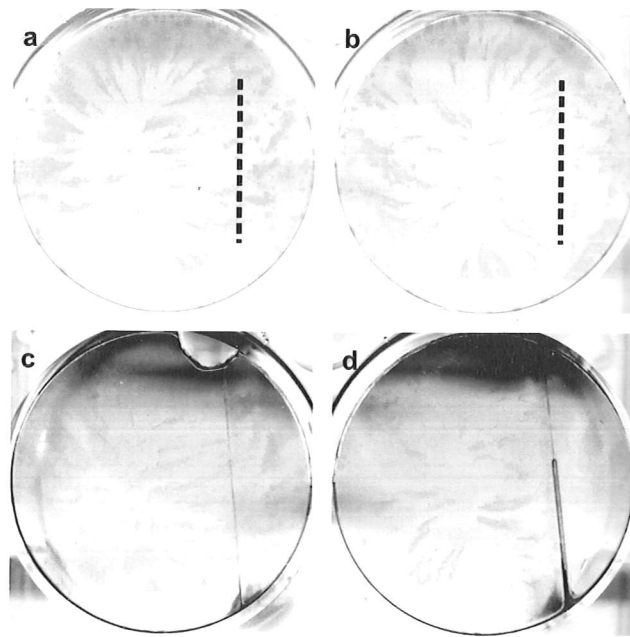


**Figure 6.9:** Results of the baffle experiments. The dashed lines in **a** and **b** indicate the intersection between overlay and baffle (cover slip) during incubation. Results from chord experiments are shown in **c** and **d**.

comets in a normal plaque assay and those formed in the presence of a baffle is made in figure 6.10 on the next page. Without a baffle (**a**), comets streak radially outward from the centre; with a baffle, the apparent centre from which comets radiate has been shifted – marked with ellipses in **b**. The comets appear to form in region ① as if the part of the well behind the baffle (region ②) is not present; in region ② itself, comets do not seem to form at all.

This supports the idea that the insertion of a baffle disrupts a comet-forming flow in the overlay, as depicted in figure 6.8. This experimental evidence also strongly supports the rejection of any concentration gradient-based hypothesis, since the baffle does not cleave the overlay into two disjoint regions – it merely disrupts flow in the *upper* half of the fluid.

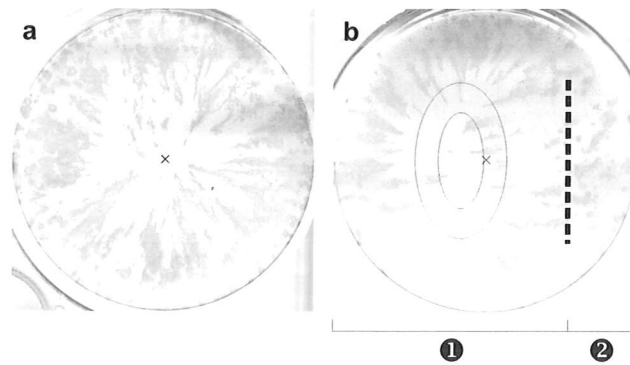


**Figure 6.10:** Comets in: **a** a normal plaque assay experiment; **b** a well with a baffle (placement indicated by the dashed line). The centre of each well is marked with a  $\times$ .

### 6.2.4 Conclusion

Much of the experimental evidence gathered above supports the existence of a comet-forming flow in the overlay during incubation. The important question as to its origin (that is, what force is driving the flow) is addressed in the next section.

## 6.3 A mechanism for the flow

In this section we will discuss the fluid dynamic mechanisms for comet formation that have been proposed in the literature, and propose an explanation for the driving force behind the overlay flow.

### 6.3.1 Convection

Spatially non-uniform heating of a fluid often results in the formation of convection currents: warmer, less dense fluid rises above cooler, more dense fluid.

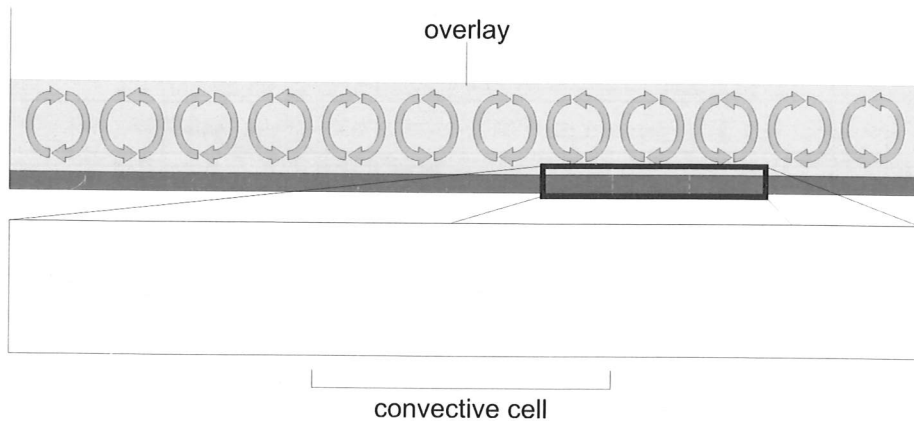


**Figure 6.11:** Comet formation in convective cells. Cells (or rolls) arising from Rayleigh-Bénard convection are roughly as wide as the depth of the liquid. Such cells in this setting would create adjacent regions in which short comets streak in opposing directions, contrary to experimental observation. The aspect ratio is not drawn to scale.

### Rayleigh-Bénard convection

Past work encountering comet formation in plaque assays has suggested that convection currents in the overlay lead to the formation of comets [121]. Convection currents caused by heating from *below* (by, say, the metal rack of the incubator, which may be warmer than the atmosphere in the incubator) might lead to Rayleigh-Bénard convection. In such convection, however, cells or rolls of fluid flow tend to form, the width of each being of the same order as the depth of the fluid [75]. In the case of an overlay depth of 2 mm, there would be around 17 cells spanning a 6-well dish. Very small comets may be able to form in each of these cells, but large-scale unidirectional (radial) comets spanning several such cells could not be formed in this manner – see figure 6.11.

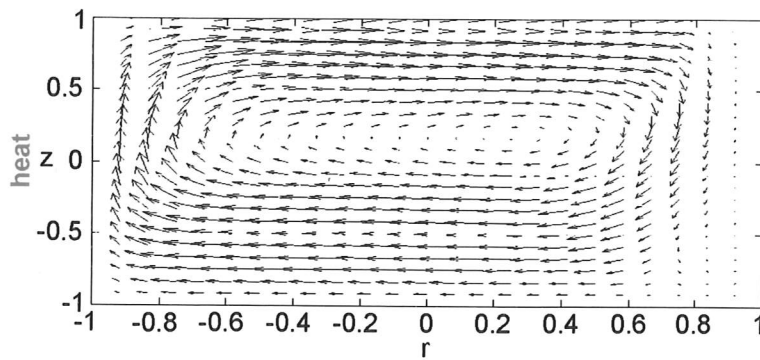


**Figure 6.12:** Convection currents caused by lateral heating. Adapted from [101].

### Other types of convection current

Convection currents driven by lateral heating are of the correct form (see figure 6.12), but usually require significantly steeper temperature gradients and significantly smaller aspect ratios than those present in this setup (see, for example, [101]). Here, heating of the medium during incubation should in theory be roughly steady, both in time and in space (across the dimensions of the well), so that convection currents of this type would appear highly unlikely.

### 6.3.2 The Marangoni effect

The Marangoni effect is the name given to the phenomenon of flow driven by gradients in surface tension. Where a gradient in surface tension exists, the surface fluid is pulled toward regions of higher tension, entraining underlying fluid in the process.

The best known example of this effect is the 'tears of wine' phenomenon, first explained by James Thomson [196], caused by evaporation of alcohol (ethanol) from wine. At the meniscus on the sides of the glass, the increased surface area per unit volume results in an increased local evaporation rate of ethanol. This local change in ethanol concentration raises the surface tension, dragging the surface of the wine up the sides of the glass. As the wine spreads up the sides of the

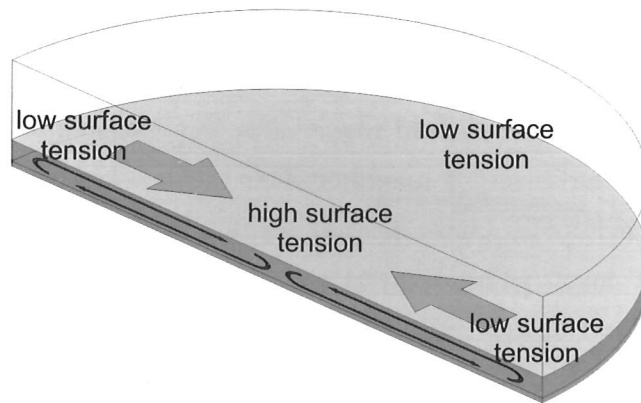


**Figure 6.13:** A surface tension gradient might be driving the comet-forming flow. As fluid is dragged over the surface, it entrains fluid in the bulk beneath, setting up a flow like that depicted in figure 6.2.

glass and its the surface area increases, so too does the evaporation rate of the ethanol, leading to greater increases in surface tension and further motion up the glass. Droplets of wine form on the sides of the glass, which the fall back down under gravity, forming the 'tears'. The Marangoni effect has been studied widely, in such fields as surface chemistry [59], industry [149], fluid dynamics [146], and geophysics [3].

Surface tension is a factor of both chemistry and temperature. The surface tension of water at 20°C is 72.8 dynes/cm (the amount of force, measured in dynes, required to break a film of length 1 cm); this drops to roughly 69 dynes/cm at 37°C [66]. Spatial variations in temperature, therefore, lead to gradients in surface tension. In the above example of wine crawling up a glass, evaporation of ethanol leads to increased surface tension: the surface tension of ethanol at 20°C is only 22.3 dynes/cm, so that as the concentration of ethanol in the wine decreases the surface tension increases toward that of water, its major constituent.

Gradients in surface tension, whether they are caused by temperature or chemistry, can lead to surface flows. In the case of these experiments, it is possible that a surface tension gradient may be driving the flow (figure 6.13). Surface tension-driven flows in shallow liquid layers have been observed before – see, for example, [108] – though not in such pronounced aspect ratios as those found here.

### 6.3.3 Varying surface tension

Whilst turning to the question of *what* might be inducing a gradient in the surface tension of the overlay in 6-well dishes, experiments were also performed to determine whether changing the overlay surface tension would affect comet formation. If surface tension gradients are driving the comet-forming flows, then reducing the surface tension may reduce the strength of the flow, and so the length of observed comets.

Two surfactants were used to alter the surface tension of the overlay: lecithin and Pluronic F68. Both are considered non-toxic at the concentrations used here, and so are suitable for use in organic systems. Lecithin, or phosphatidylcholine, is a phospholipid required for the construction of all bilayer lipid membranes in organic cells [25], and is widely used in foods and in experimental science. Pluronic F68 is a non-ionic surfactant, and has been used in *in vitro* and *in vivo* experiments throughout the biological sciences (e.g. [81, 164, 211]).

L- $\alpha$ -phosphatidylcholine (Sigma Co., Surrey, UK) was added to overlay in final concentrations of 0.025%, 0.0125%, 0.0025%, and 0.00125%; Pluronic F68 (Sigma Co., Surrey, UK) was added in final concentrations of 0.3%, 0.1%, 0.03%, and 0.01%.

The surfactants' effects on the surface tension of overlay were measured using pendant drop tensiometry. In this technique, a computer-controlled syringe is used to pump out drop of liquid a few microlitres in volume (figure 6.14 on the next page). This drop deforms under gravity, the shape of which is dictated by (among other things) the surface tension of the liquid. A profile of the drop is captured by digital video camera, and analysed by computer, which uses shape of the profile (as well as physical properties of the liquid, e.g. density) to calculate the surface tension. All measurements were taken at room temperature. Evaporation of substances from the pendant drop (which would result in a change in surfactant concentration with time) was minimized by surrounding the drop with a transparent cuvette containing a small quantity of water to increase local humidity.

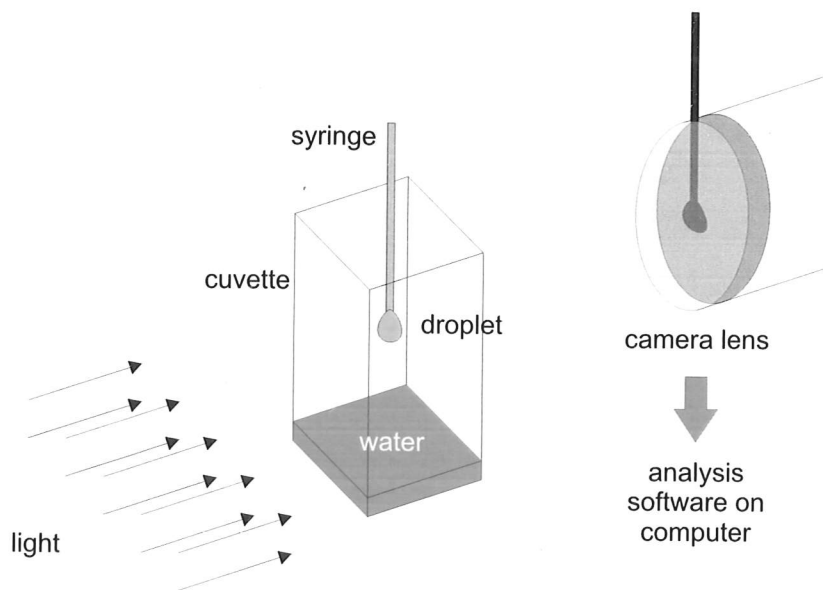


**Figure 6.14:** Experimental setup for pendant drop tensiometry. Light shining on a microlitre drop of liquid casts a shadow profile captured by a digital camera connected to a computer. Software on the computer then uses the shape of the profile to compute the surface tension of the liquid.

Surface tension measurements can be seen in figure 6.15 on the following page – overlay surface tension decreased monotonically with increasing surfactant concentration. The surface tension of overlay ( $\approx 61$  dynes/cm) in the absence of surfactant was also measured.

Wells were seeded and infected as normal and overlay treated with the concentrations of lecithin used above was added to a depth of 2 or 4 mm. From the overlay depth experiments outlined in section 6.2.1, we expect comets to form at 2 mm depth, but no comets to form at 4 mm depth; this setup hence allows us to assess the effects of surfactant concentration on comet formation (2 mm), and control for any biochemical effects that lecithin might have on infection (4 mm).

The effects of lecithin-mediated changes in overlay surface tension on comet formation can be seen in figure 6.16 on page 112, from which it appears that decreased surface tension results in the formation of shorter comets at the 2 mm overlay depth. Biochemical suppression of infection can be discounted, as there is no dependence

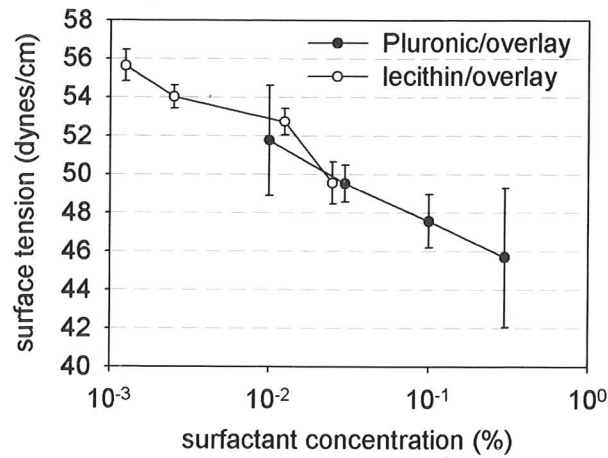


**Figure 6.15:** Measurements of the overlay surface tension with varying concentrations of Pluronic F68 and lecithin. Mean values were calculated from measurements taken from 3 separate droplets. Error bars are 95% confidence intervals for the mean.

of plaque length on lecithin concentration at the 4 mm overlay depth – were the comets shorter because of some biological action of lecithin, we would expect the growth of circular plaques to have been similarly reduced.

However, when the experiments were repeated with Pluronic F68, the results were not entirely in line with expectation (also shown in figure 6.16). Despite reaching lower surface tensions, the use of Pluronic-treated overlay does not shorten comets to the same degree: for a given lowered surface tension, lecithin treatment shortens comets more than does Pluronic.

It appears that reducing overlay surface tension does result in a reduction of mean plaque length, which supports the Marangoni flow hypothesis. However, surface tension is clearly not the whole story: the consistent disparity between the lecithin and Pluronic results must be accounted for. If not through surface tension changes directly, how might the surfactants lecithin and Pluronic F68 be impeding flow? The answer may lie in the physical properties of the surfactant monolayers created as the surfactants absorb to the surface.

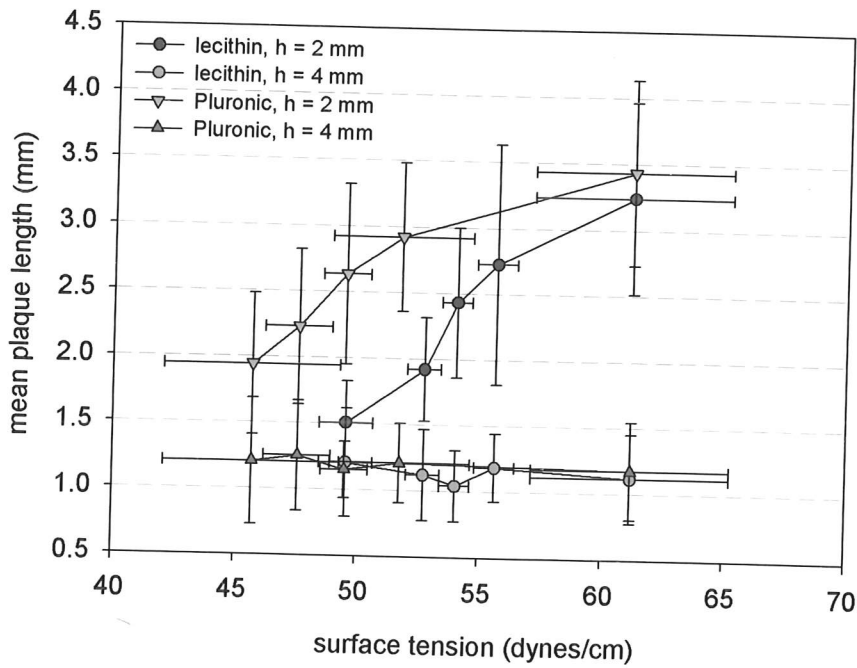


**Figure 6.16:** Mean plaque length against overlay surface tension using lecithin or Pluronic F68 (as indicated). The two highest surface tension data points correspond to untreated overlay (i.e. 0% concentration). Mean values and error bars (horizontal) for the surface tensions are the same as those in figure 6.15. Mean values for the plaque length were calculated as for the overlay depth and viscosity experiments. Error bars are 95% confidence intervals for the mean. The non-overlapping of the error bars for the measurements at the lowest and highest surface tensions indicate a statistically significant difference between the comet lengths (at the 0.05 level).

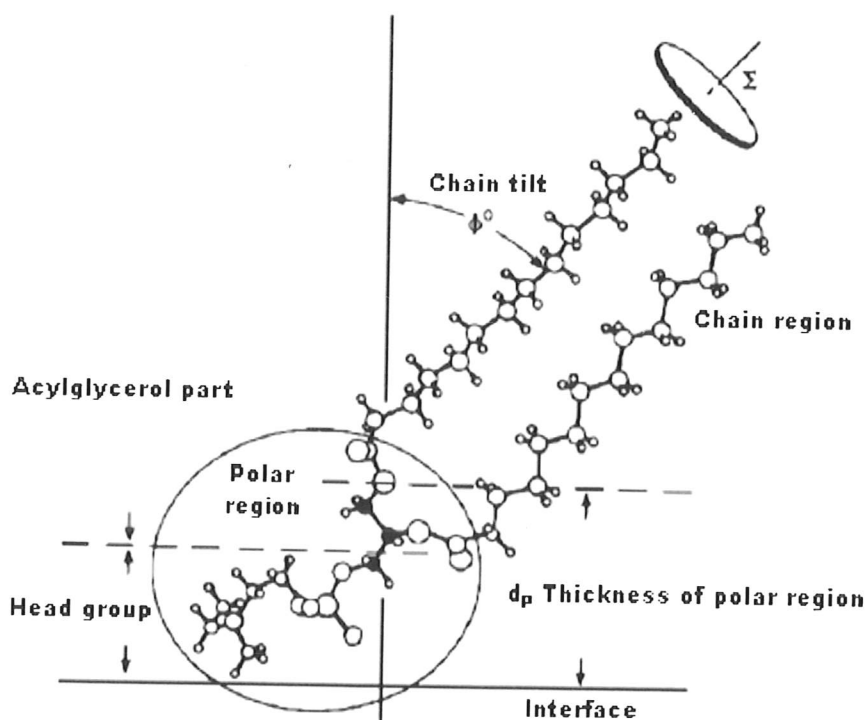


**Figure 6.17:** The chemical structure of lecithin (phosphatidylcholine), showing the polar head group and non-polar tail. Figure adapted from [74].

### 6.3.4 Viscoelasticity in Langmuir monolayers

Most surfactants are *amphiphilic* organic compounds: each molecule has a polar region (a hydrophilic or water-soluble head) and a non-polar region (a hydrophobic or water-insoluble tail) – e.g. figure 6.17, which shows the chemical structure of lecithin. Such molecules, when immersed in water with a water-air (or water-oil) interface, will naturally arrange themselves so that their polar heads are in contact with water and their non-polar tails in contact with air (or oil) i.e. they will seek out surfaces or interfaces. Hence 'surfactant': their action is generally confined to liquid surfaces or interfaces.

As surfactants adsorb onto the surfaces of water-based liquids, they form a very thin film ( $\approx 1$  molecule in depth) on the surface called a Langmuir monolayer. These monolayers behave as gases, liquids, or even solid 'crusts', depending on the

physical properties and concentration of the surfactant; these properties, namely the viscosity and elasticity of the monolayer, can be measured (see, for example, [40]).

In the context of the comet formation experiments, it is possible that the monolayers formed by lecithin on the overlay surface have a higher viscosity or elasticity than those formed by Pluronic F68. A more viscous, elastic film would act more like a solid barrier than a free surface, and, just as the no-slip condition forces the flow to slow near the bottom of the well, so would such a viscous monolayer slow the flow near the surface. The dissipation of energy caused by this effect, and by the entraining of surface monolayer into the flow, might reduce the overall flow speed, and in turn the lengths of comets formed.

Unfortunately, constraints of time and equipment prevented the measurement of the viscous and elastic moduli of overlays treated with these surfactants, and such study in any case falls outside the scope of this thesis.

### **6.3.5 Conclusions**

The reduction in comet length observed when lowering the surface tension with surfactant suggests that surface tension plays a significant role, which lend weights to the Marangoni argument. The subsequent discovery that lowering the surface tension to the same (or lower) levels with a different surfactant (Pluronic F68) has a less pronounced effect on comet length appears to indicate that there are other factors besides surface tension at work. Here, the surfactants may be acting to physically suppress the flow, by forming a visco-elastic monolayer at the overlay surface. It is not immediately apparent how an experiment could be designed which would extricate these two effects.

If the Marangoni effect is driving mechanism for the comet-forming flow, it still remains to discover how the requisite gradient in surface tension arises. In the next section we will examine possible causes for these gradients in surface tension.

## 6.4 Possible gradients driving the flow

As previously argued, the average speed of the comet-forming flow must be very low, since comets rarely grow above 1.5 cm in length over the 48 hour incubation period. In addition, the growth of the comets appears to be generally uniform, with smooth tails or regularly spaced secondary plaques in the tail. These two observations lead us to conclude that the driving force behind the flow is (a) very small and (b) roughly continuous in time.

The comet-forming flow is likely to be driven by a gradient of some kind (since we have ruled out alternatives such as environmental disturbance). For a slow flow, and correspondingly a small driving force, the gradients involved would not have to be very steep, be they gradients in temperature (i.e. convection), chemistry (rejected in section 5.3.2), or surface tension (i.e. a Marangoni flow).

### 6.4.1 Temperature gradients

The water bath experiments, in addition to ruling out environmental disturbance as a factor in comet formation, also rule out large changes in incubator temperature as a result of door opening and closure (since the water baths used were dedicated exclusively to these experiments, and remained undisturbed throughout incubation).

Referring to the operating specifications of the incubators and water bath used in this series of experiments, it was discovered that the temperature of 37°C is maintained in incubators with an accuracy of 0.5°C spatially (variation in temperature throughout the incubator interior), and 0.1°C temporally (variation with time), and in the water bath with an accuracy of 0.3°C temporally (spatial variations in the water bath are negligible). As these variations occur, it is possible that the thermally more stable plastic of the dishes, in contact with the metal trays of the incubator (or the container in the water bath), may remain warmer than the faster-cooling atmosphere above the surface. Though these variations would be very small (less than 0.1°C), they may provide sufficient impulse to drive a fluid flow over the 2

days of the experiment.

## 6.4.2 Surface tension gradients

Any temperature gradients that exist may lead to convection currents in the overlay, which would then be responsible for comet formation. Alternatively, or concurrently, such temperature gradients may give rise to surface tension gradients, leading to Marangoni flows in the overlay.

### Estimation of the magnitude of the surface tension gradient

We may estimate the magnitude of the surface tension gradient required to generate flows of the observed speed ( $10^{-7} \text{ ms}^{-1}$ ) by estimating the relevant parameters from the experimental results. These parameters and their estimates are shown in table 6.1.

<i>parameter</i>	<i>description</i>	<i>value</i>
$\gamma$	surface tension of overlay	$6 \times 10^3 \text{ Nm}^{-1}$
$\frac{d\gamma}{dr}$	surface tension gradient	to be estimated
$\mu_{\text{water}}$	dynamic viscosity of water	$8.9 \times 10^{-4} \text{ kg m}^2\text{s}^{-1}$
$\mu$	dynamic viscosity of overlay	$\approx 30 \times \mu_{\text{water}}$
$h, R$	fluid depth, radius	$h = 3 \text{ mm}, R = 16 \text{ mm}$
$V$	characteristic flow speed	$10^{-7} \text{ ms}^{-1}$

**Table 6.1:** Parameters for surface tension gradient estimation.

- Overlay viscosity  $\mu$  was estimated from the graph in figure 6.7.
- Overlay density was estimated to be roughly the same as that of water.

By conservation of energy, assuming a steady Stokes flow, the work done by the surface tension must balance the energy lost through viscous dissipation:

$$\int_S u \cdot \sigma \cdot ndS = \int_V 2\mu e_{ij} e_{ij} dV \quad (6.3)$$

Assuming the fluid to be a thin layer, with  $h \ll R$ , the strain tensor is dominated by the horizontal strain rate:  $e \sim \frac{V}{h}$ . Therefore,

$$\begin{aligned} D &= \int_V 2\mu e_{ij} e_{ij} dV \sim \mu \frac{V^2}{h^2} R^2 h \\ &= \frac{\mu V^2 R^2}{h} \end{aligned}$$

The work done on the surface is dominated by the surface tension gradient:

$$E = \int_S u \cdot \sigma \cdot ndS \sim V \frac{d\gamma}{dr} R^2$$

Using these approximations in equation 6.3 gives a relationship between the surface tension gradient and the other parameters in the system:

$$\frac{d\gamma}{dr} \sim \frac{\mu V}{h}$$

Substituting in the values from table 6.1 gives an order of magnitude estimate for the surface tension gradient required to drive a flow of the observed velocity  $V$ .

$$\begin{aligned} \frac{d\gamma}{dr} &\sim \frac{\mu V}{h} \\ &\approx \frac{(30 \times 8.9 \times 10^{-4}) \times 10^{-7}}{3 \times 10^{-3}} \\ &\approx 10^{-6} \text{ Nm}^{-2} \\ &\approx 10^{-10} \text{ N cm}^{-2} \end{aligned}$$

## Generating the surface tension gradient

The above calculation suggests that the surface tension gradient required to drive a  $10^{-7} \text{ ms}^{-1}$  flow in the overlay is very small indeed. Such a gradient might arise from minute gradients in temperature across the surface of the overlay, or tiny variations in the concentration of one or more of the chemical compounds in the overlay.

## 6.5 Discussion and conclusions

### 6.5.1 Summary of experimental results

In this chapter we have investigated the hypothesis that a flow in the overlay during incubation is the mechanism responsible for comet formation in plaque assays of influenza A. The following summarises the experimental results in support of this theory.

- **Overlay depth** (section 6.2.1) – we have shown that mean comet lengths decrease as overlay depth increases, and proposed explanations for how this might result from the existence of a comet-forming flow.
- **Overlay viscosity** (section 6.2.2) – we have shown that mean comet lengths decrease as overlay viscosity increases.
- **Insertion of baffles** (section 6.2.3) – we have demonstrated that the insertion of baffles into the overlay disrupts the local formation of comets, strongly indicating that a comet-forming flow is indeed being impeded.
- **Axisymmetry and shape** (sections 5.2.1 and 6.1.1 – we have highlighted the axisymmetric properties of comets.
- **Radial dependence** (section 6.1.1 – we have demonstrated that comet length is dependent on the radial position of the comet nucleus.

When investigating the possibility that the flow is being driven by gradients in overlay surface tension (a Marangoni flow), we have gathered the following results.

- **Reduction in surface tension** (section 6.3.3) – reducing the overlay surface tension with surfactant results in the formation of shorter comets; however
- **Disparity between surfactants** – compared with lecithin, reducing the overlay surface tension to the same (and in fact lower) value with Pluronic F68 yields a less pronounced shortening of comets. We have suggested reasons why this might be the case.
- **Gradient of some kind driving flow** (sections 5.3.3 and 6.4) – we have discussed possible driving forces behind the flow, including those of temperature and surface tension (mediated by temperature or some other agent).

### 6.5.2 Conclusion: the origin of comets

Comets are formed by flows in the overlay during incubation (figure 6.2). The dependence on the radial position of the comet nucleus (figure 6.3), overlay depth (figure 6.5), viscosity (figure 6.7), and surfactant concentration (figure 6.16), as well as the marked changes in pattern observed on insertion of baffles into the overlay (figure 6.9), all point toward this conclusion. However, the precise mechanism behind the flow has yet to be pinned down. There is a great deal of scope for more detailed study of the fluid dynamics of this system: a slow, viscous, surface-driven flow in a highly skewed aspect ratio.

### 6.5.3 Open questions

This work has necessarily left some open questions. Chief among them are:

- What is providing the driving force to initiate and maintain comet-forming flow in the overlay?

- How can the flow be directly visualised?

#### 6.5.4 Further experiments

The following experiments would allow many of the unanswered questions raised in the preceding work to be addressed.

**Existence of temperature gradients.** Affixing sensitive temperature probes to various positions on a dish for the duration of incubation, and recording the minute-by-minute or hour-by-hour temperature variations would settle the question as to the existence of temperature gradients. Unfortunately such equipment was unavailable for use during this work.

**Direct flow visualisation.** Flows in transparent liquids have previously been visualised by the suspension of small beads (of e.g. Teflon-coated polystyrene) or drops (of e.g. silicone oil) [175]. Time-lapse photography is used to capture the streak lines of these particles as they move through the fluid. Matters are complicated here by biological considerations:

- The silicone oil must not prove toxic to the cells, or remove virions or other substances from the overlay. This problem may be overcome by removing the cells and virus from the system: unless the gradients responsible for driving the flow are a result of some biochemical process associated with the presence of the cell monolayer or viral infection (which has been effectively ruled out in this work), they should not be necessary for the flow formation. This would result in a completely inorganic series of experiments which could be performed in a fluid dynamics laboratory.
- The entire experiment, including photographic equipment and lighting, must be performed inside an incubator, to reflect the conditions under which comets are observed.

Various attempts were made to visualise flow in sterile dishes (containing overlay only) incubated at 37°C for 48 hours as normal. Aniline blue dye and aluminium powder were used to mark the overlay surface, so that movement of the surface could be detected by comparing photographs taken before and after incubation. However, these experiments were unsuccessful: the dye diffused across the surface and into the bulk of the liquid, and the aluminium powder spread out on application and subsequently sank, rendering both methods ineffective for flow visualisation.

It could be argued that in plaque assays the virions *themselves* are acting as a flow visualisation tool, so that comets are nothing more than path lines of virions moving in the flow. However, this reasoning is circular: using the existence of comets as a proof of a theory behind their formation.

**Removal of the free surface.** To test whether a surface tension gradient is driving the flow, it may be possible to remove the free surface entirely. Here, too, biological considerations complicate the experimental design:

- The atmosphere inside the incubators used is not only heated to 37°C, but is also kept at 5% CO<sub>2</sub>. The overlay in experiments must be in contact with this atmosphere to allow the gas exchange necessary for cell monolayer vitality. The use of a gas-permeable membrane may solve this problem, allowing removal of the free surface without cutting off gas exchange.
- This difficulty could be circumvented if it is established (by inorganic flow visualisation) that comet-forming flows appear in the absence of a cell monolayer and viral infection.

### 6.5.5 Implications for modelling

This work has important implications for modelling work like that carried out in the earlier chapters of this thesis (see also section 5.1.3). If we are to build models of virus spread, either *in vitro* or *in vivo*, and we are to parameterize these models using

data gathered from experiments like plaque assays, we must take great care when duplicating the physical properties of the environment where infection takes place. As we have seen here, seemingly mundane changes in non-biological properties (like overlay depth or viscosity) have consistent effects on the observed results.

### **6.5.6 Control of cometing**

At a more practical level, this work has shown that comets are a non-biological phenomenon. They are a result of experimental method or protocol, and can be controlled for. As we saw in section 5.1.2, comet formation makes counting of plaques more difficult, and so makes plaque assays less accurate. Here we have identified simple steps to avoid comet formation, at least in the case where a viscous overlay is employed. Specifically, increasing the depth or viscosity of the overlay should eliminate cometing in plaque assays.

# Chapter 7

## Discussion and conclusions

This thesis is concerned with the spatial dynamics of *in vitro* viral infection, and has approached this topic from two distinct but related directions. In this, the final chapter, I summarize briefly the work undertaken, and address the questions raised in the introduction. As is often true, more questions and issues have been uncovered over the course of this research; these issues are presented here. The thesis ends with a look at future directions for research.

### 7.1 Overview of thesis

#### 7.1.1 Motivation

In chapter 1 we explored the importance of within-host and immune modelling, particularly in its application to the development of drug therapies and population-level epidemiological models. A need was identified to study the small-scale, spatial dynamics of innate immunity as a basis for the construction of more advanced within-host models.

### **7.1.2 Experimental data**

Chapter 2 introduced an experimental system, the *in vitro* infection of epithelial cell monolayers with HSV-1. This system exemplifies one of the simplest and most important innate responses to viral infection: the secretion of IFN. Data on the growth of plaques obtained from such experiments were analysed to yield a quantitative measure of viral spread, illustrating the interplay between the progression of infection and the antiviral effects of the induced interferon response.

### **7.1.3 Model development and simulation results**

A stochastic model of *in vitro* HSV-1 infection was designed and implemented in chapter 3, employing the data from chapter 2 in its parameterization. In chapter 4 this model was then used to simulate infections at a huge range of doses, to answer some of the questions raised in the introduction. These results tentatively suggest the existence of critical doses: for minimum monolayer recovery time, maximum IFN production, and the threshold beyond which recovery becomes impossible. The work also suggests that priming of susceptible cells is accessible to modelling of this kind, allowing us to study the effects of pre-exposure to IFN in the context of vaccine and drug therapy.

### **7.1.4 Factors affecting plaque growth**

Next, we investigated *in vitro* viral infection from a second direction, looking at plaque assays generally. Chapter 5 began by emphasizing the importance of understanding the various factors involved in plaque formation: if plaque assay data is to be reliably used in the parameterization of spatial models of infection, we must be able to distinguish between the biological and non-biological factors contributing to the growth of plaques. Following this, the phenomenon of competing in plaque assays of influenza A was introduced. This constitutes an ideal system for the study of plaque formation, given the marked differences in outcomes of seemingly similar

experiments. The chapter tested the various hypotheses explaining cometing which had been suggested in the literature and elsewhere.

### **7.1.5 Comets: a fluid dynamic phenomenon**

Chapter 6 moved on to explore the fluid dynamic hypothesis, contending that comets form as a result of axisymmetric overlay flow during incubation. The following conclusions were drawn:

- Comets are formed when virions released by infected cells are picked up by an axisymmetric flow in the overlay and deposited downstream of the initial site of infection ('nucleus'), leading to a string of second infections ('tail'). Crucially, this means that comet formation is the result of environmental, rather than biological, forces.
- This flow is sensitive to physical properties of the overlay: cometing can be suppressed by increasing the overlay depth or viscosity.
- The mechanism by which the overlay flow is driven has not been determined, though several possibilities have been identified. Experiments have been proposed which would enable further investigation of this problem.

## **7.2 General conclusions**

A goal central to this dissertation was the construction of a simple model to investigate an important aspect of innate immunity, the IFN response to viral infection. After setting out the motivation behind such work, and investigating the various types of model design open to us, a spatial, stochastic, individual-based model was developed and parameterized to data from experiments. This model successfully captured the dose dependence in the plaque growth dynamics seen in the data, and

was also able to replicate (approximately) the results of experiments in which cells were primed with IFN prior to infection.

While it is important to acknowledge that this is a simple model of a greatly simplified (even artificial) system, it serves as a proof-of-concept in spatial immune modelling at the cell-to-cell scale, and a starting point for more advanced work in this vein (see below). The model was employed to answer some of the dose-dependence questions in *in vitro* infections that were raised in chapter 1. Simulation results suggested the existence of critical doses at which the properties of infection change, and reasons for their existence were proposed (sections 4.2 and 4.5).

The second half of this thesis looked at the growth of plaques from an experimental angle. The formation of comets in plaque assays of influenza A was investigated, and was concluded to be a purely fluid dynamic effect. The implications for modelling have already been stated (sections 5.1.3 and 6.5.5): parameterizing a spatial model of viral infection to data from plaque assays without understanding the non-biological factors that play a role in *in vitro* plaque formation may result in a model which behaves in unrealistic ways.

### 7.3 Limitations and future work

This point leads us on to one of the most important limitations of this work. As I have said above, the model developed here is one of great simplicity, and it is a model of an already greatly simplified system. We discussed some of the limitations in chapter 4, but the overriding problem is this: the unquestionable merits of studying an *in vitro* system – the simplicity inherent in the lack of a cellular immune response, full range of cytokines, and 3D structure – are also its chief failing. All *in vitro* models are artificial in this sense<sup>1</sup>.

---

<sup>1</sup>This does not stop them from being an indispensable tool throughout biology, particularly when focusing on the function or action of specific cell types or pathogens. It should also be noted that it is possible to study 3D structures *in vitro*, e.g. organ culture.

Particularly relevant to the work in chapters 5 and 6 is that, even though no comets were seen in the plaque assays of HSV infection of MDBK monolayers, it is almost certain that *some* property of the experimental system (besides the biological ones – cell line and virus strain) is impacting on the spread of virus. Simply put, changing the experimental protocols used will alter the observed plaque dynamics. This leads to an obvious but important point: a model parameterized to specific empirically-derived sets of data can only be relied upon to quantitatively reflect the dynamics in the same experiments as those which provided the data. However, it is imperative to note that this does not detract from the model's usefulness: qualitative behaviour can be studied, general questions addressed, and others uncovered, just as we have seen in this work.

### 7.3.1 Within-cell modelling

In section 4.5 we highlighted the simplicity with which cells in the model were treated: 'black boxes' onto which virions and IFN- $\beta$  bind, from which IFN- $\beta$  is secreted, and out of which new virions emerge on infection-mediated cytolysis. Necessarily, the assumptions made here about the dynamics of cell-level mechanisms impact on model behaviour. To justify or improve upon these assumptions (e.g. the assumption that once stimulated, interferon production continues *ad infinitum*), we may turn to within-*cell* modelling.

Analogous to the move from epidemiological to within-host models, dropping down to the cellular level allows us to study some of the issues raised in within-host modelling. Specific to the work here, for example:

- How does IFN concentration affect the rate at which a cell becomes antiviral?
- Is it some sort of time-integral, and is there a minimum time?
- For how long is the antiviral state maintained?
- Is it indefinite in the continued presence of IFN?

Just as the shift to within-host modelling introduced many aspects of immunology and virology, so within-cell modelling will place a greater emphasis on biochemistry. Instead of considering the spatial spread of virions throughout a domain, within-cell modelling might consider the production rate of interferon regulatory factors (IRFs) or antiviral proteins, or the speed with which invading virions establish an infection.

### 7.3.2 The 'virtual' host

As we saw in section 4.5, spatial immune modelling of the kind set out in this thesis has a wide range of potential applications. It can easily be extended to other virus types and cell lines, likely requiring only slight modification to the underlying assumptions (e.g. whether the virus is lytic or not) and reparameterization. Much more importantly, it marks a step in the development of a more fully fledged spatial within-host model.

The ultimate aim of within-host modelling must surely be the construction of a 'virtual' host, an *in silico* recreation of an organism in which endless infections can be simulated. Such a model would be invaluable in the understanding of the pathology of disease and the invasion of new pathogens, and in the testing of drug therapies and vaccines, as well as allowing us to improve the assumptions made about within-host dynamics in epidemiological models.

The development of a virtual host requires understanding of the dynamics across many scales: from within-cell modelling, through local spatial effects, to the biology of a complete organism. En route to this full within-host model there are many waypoints, introducing successively more complex aspects of the full vertebrate immune system. Starting at the smallest scales, we might consider the subtleties of IFN production and action (within-cell modelling); local spatial spread of infection (like the modelling detailed in this document); advection or diffusion of virions (seen *in vitro* in cometting); the wave-like beating of ciliated epithelial cells (important in respiratory tract infections such as influenza); the cellular components of the innate immune system; the adaptive response – the list continues. Progress toward this end

is limited only by our knowledge of the host biology, by our quantitative methods for grasping the underlying dynamics, and by our computational resources, and it seems most likely that, in time, these obstacles will be overcome.

# Appendix A

## HSV data sets

This appendix contains the data sets for the Vero 50 pfu and MDBK 10, 50, and 500 pfu experiments – each a series of 6 photographs of plates left post-infection for 1–6 days.

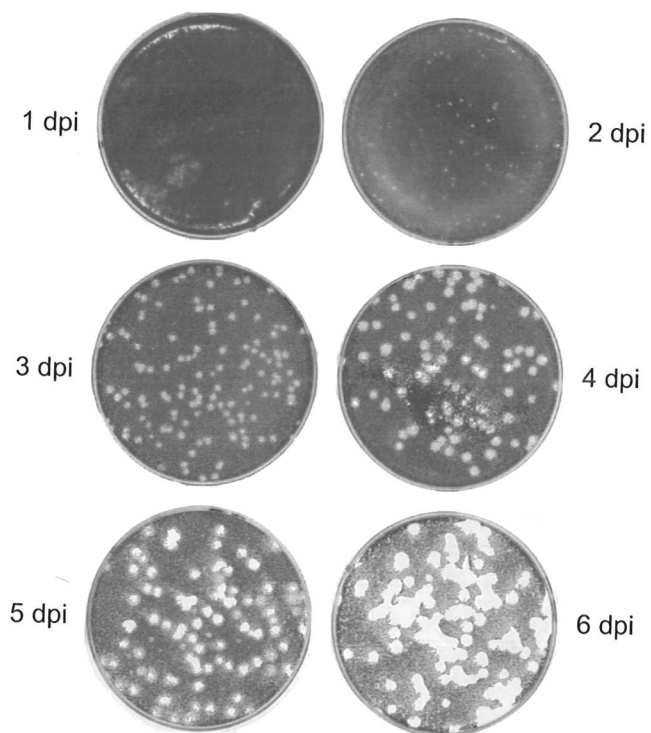


**Figure A.1:** Data set from Vero cells infected with 50 pfu.

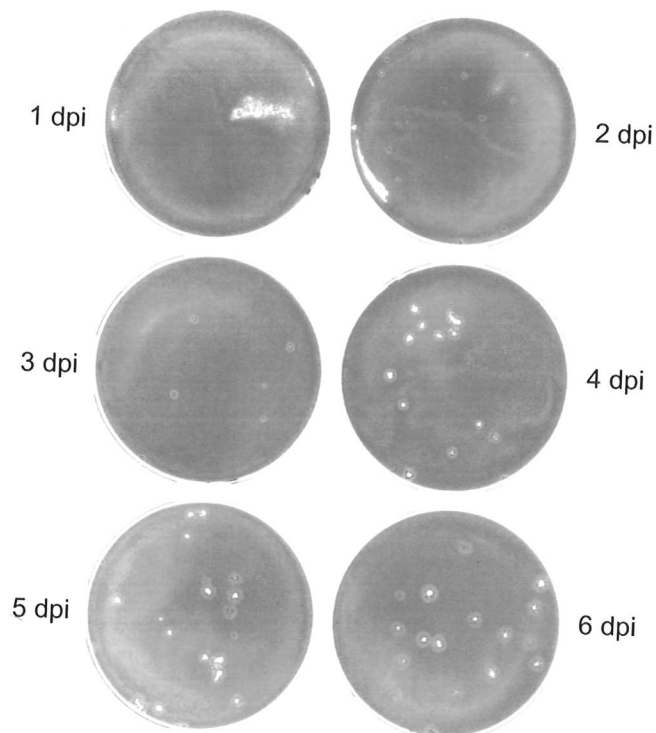


**Figure A.2:** Data set from MDBK cells infected with 10 pfu. The white patches visible in the first and second days post infection (and in the first dpi for the 50 pfu data set in figure A.3) are not plaques, but are in fact regions where the photograph has been overexposed (most likely by reflection from external light sources).

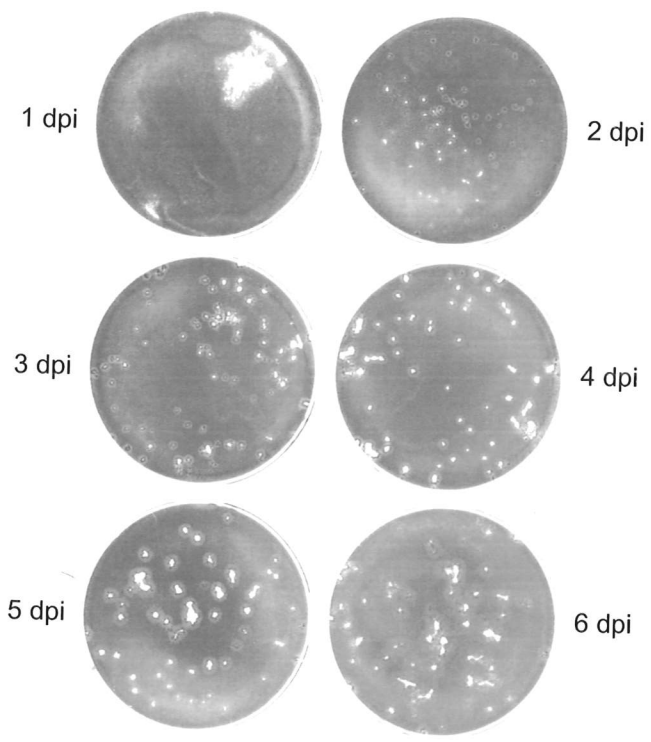


**Figure A.3:** Data set from MDBK cells infected with 50 pfu.

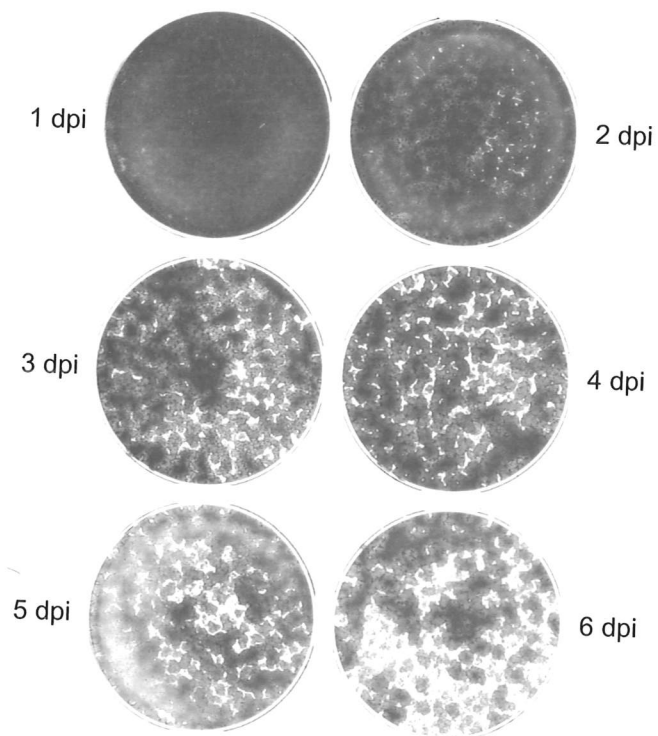


**Figure A.4:** Data set from MDBK cells infected with 500 pfu.

## Appendix B

### Materials and methods for comet experiments

The materials and methods used to perform the experiments described in chapters 5 and 6 starting on page 69 are detailed below.

#### B.1 Cells and viruses

Epithelial MDCK (Madin-Darby canine kidney) cells [73] were grown in Dulbecco's modified eagle's medium (DMEM; Sigma Co., Surrey, UK) supplemented (and referred to as 'complete' DMEM) with 2 mM glutamine, 100 U/ml penicillin, 100  $\mu$ g/ml streptomycin, and 10% (v/v) foetal calf serum (FCS). Influenza virus PR8 (A/Puerto Rico/8/34) stock was grown in embryonated eggs, and titred by plaque assay on MDCK cells.

## B.2 Plaque assays

### Seeding and infection

MDCK cells were seeded in 6-well cluster dishes (TPP, Switzerland) at a density of  $1.2 \times 10^6$  cells per well in 2 ml of complete DMEM so that monolayers were confluent after 24 hours incubation at 37°C in an atmosphere with 5% CO<sub>2</sub>. Virus stocks (PR8 unless otherwise indicated) were serially diluted in DMEM supplemented with 2mM glutamine and 100 U/ml penicillin (serum-free-, or SF-DMEM). After aspiration of growth medium, the monolayers were washed with SF-DMEM. 0.4 ml of inoculum was added and the cells incubated for 45 min to allow infection to establish. The inoculum was then aspirated off and a CMC:SF-DMEM (in ratio 1:1; CMC, carboxymethyl cellulose, Sigma Co., Surrey, UK) overlay added to inhibit long range diffusion of virions in the medium. This overlay was supplemented with 5% (v/v) of 7% bovine serum albumin (BSA) and 0.1% (v/v) Worthington's trypsin. The dishes were then incubated for 2 days.

### Fixing and staining

Following incubation, the cells were washed with PBS, fixed with 4% formaldehyde in phosphate buffered saline (PBS) for 20 min, then washed with PBS containing 2% newborn calf serum (NCS). The monolayers were probed with 0.2% rabbit anti-PR8 antibody (spun out of blood taken from rabbits inoculated with inactivated whole PR8) in PBS/NCS for 1 hr, followed by washing with PBS/NCS, and subsequent probing with 0.3% horse radish peroxidase (HRP) linked anti-rabbit (Amersham Biosciences, Buckinghamshire, UK) in PBS/NCS for 1 hr. Then, after a final wash with PBS/NCS, a TMB (3,3',5,5'-tetramethylbenzidine) stabilized substrate for HRP (Promega Corp., Madison, WI, USA) was added, and washed off with water once plaques became clearly visible to the naked eye.

## **B.3 Other assays**

### **B.3.1 Infectious centres assays**

Cells were seeded, infected, and incubated as for plaque assays. After incubation, the overlay was aspirated off, the monolayers trypsinised in 1 ml PBS, the monolayers scraped to dislodge cells, and the resulting suspension centrifuged at 2.2K rpm in a microcentrifuge for 3 minutes to pellet the cells. The supernatant was removed, 1 ml of PBS added, and the cells washed by re-centrifuging (oriented so as to reform the pellet in a different location). This pellet was then resuspended in 1 ml complete DMEM, and serial dilutions to  $10^{-5}$  performed. 0.4 ml of each dilution was added to 2ml of complete DMEM with fresh MDCKs at a density of  $1.2 \times 10^6$  cells/ml and 0.1% (v/v) Worthington's trypsin. The resulting suspensions were left to incubate for 3 hours to allow the cells to settle and attach to the base of wells, and for the infection to establish, after which the medium was aspirated off and the protocol for plaque assays followed.

### **B.3.2 Supernatant assays**

Cells were seeded, infected, and incubated as for the plaque assays. After incubation, 1 ml of the overlay was removed, centrifuged at 2.2K rpm in a microcentrifuge for 3 minutes to remove suspended cells, and the supernatant removed and serially diluted to  $10^{-5}$  in SFDMEM, before being used in the place of virus stock serial dilutions in the plaque assays, the protocol for which was followed thereafter.

### **B.3.3 Immunofluorescence assays**

Cells were seeded, infected, incubated, and fixed as for the plaque assays. After fixing and washing with PBS/NCS, cells were permeabilised by addition of 0.2% Triton-X 100 (Sigma Co., Surrey, UK) and rocking for 5 minutes. Following washing,

monolayers were probed with 0.4% anti-NP (anti-nucleoprotein; spun out of blood taken from rabbits inoculated with NP) in PBS/NCS for 1 hr, then with 0.5% FITC-linked anti-rabbit (DakoCytomation A/S, Denmark)-0.05% DAPI (4'-6-diamidino-2-phenylindole; Sigma Co., Surrey, UK) in PBS/NCS for 1 hr. FITC (fluorescein isothiocyanate) fluoresces green under UV light; DAPI fluoresces blue under UV light.

### **B.3.4 Preparation of CMC**

To make 50 ml of standard concentration CMC, 0.75 g of high viscosity powder is sprinkled on to the surface of 50 ml of PBS:RO (in the ratio 6:4), followed by 0.75 g of low viscosity powder, after which the mixture is incubated overnight at 37°C, before being autoclaved and homogenized. The viscosity of the CMC was varied by altering the ratio of high to low viscosity powders used.

### **B.3.5 Oswald viscometer**

A diagram of an Oswald viscometer, as well as a brief overview of its operation, is given in figure B.1.

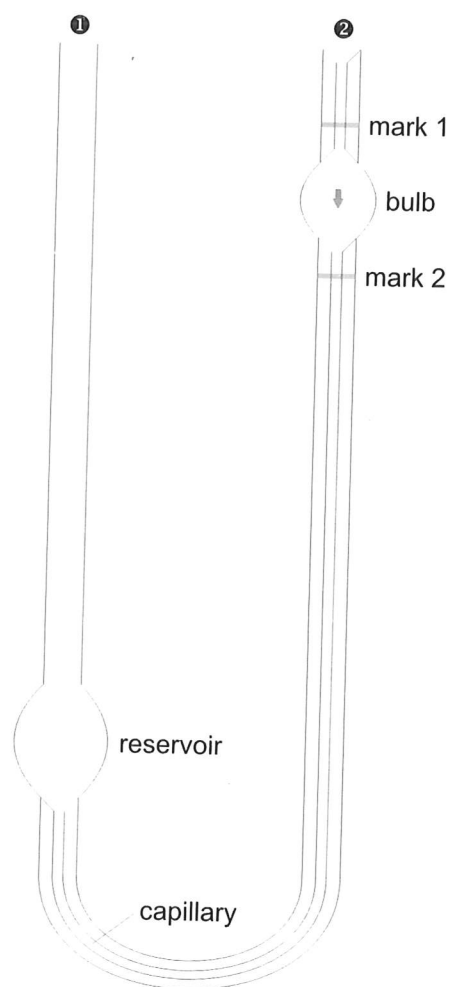


**Figure B.1:** The Oswald viscometer is used to measure specific viscosity. Firstly, a reference measurement is taken: a sample of water (or other solvent being used) is added via aperture ① and fills the reservoir. A vacuum is then applied to aperture ② until the water level rises above mark 1. The vacuum is then removed and the water level allowed to fall. The time taken for the level to drop from mark 1 to mark 2 is recorded. This is the reference measurement  $t_r$ . After rinsing and drying the viscometer (by again applying a vacuum to aperture ② until all water droplets have disappeared), the process is repeated for the sample under study, resulting in a second time measurement,  $t_s$ . The specific viscosity  $\mu$  of the sample compared with the solvent is then  $(t_s - t_r)/t_r$ .

## Bibliography

- [1] UK Food Standards Agency. List of current European Union-approved additives and their E Numbers. <http://www.food.gov.uk/safereating/chemsafe/additivesbranch/enumberlist> (accessed 2006-08-07), September 2002.
- [2] K Alheim, Z Chai, G Fantuzzi, H Hasanvan, D Malinowsky, E Di Santo, P Ghezzi, C A Dinarello, and T Bartfai. Hyperresponsive febrile reactions to interleukin (IL)  $1\alpha$  and IL- $1\beta$ , and altered brain cytokine mRNA and serum cytokine levels, in IL- $1\beta$ -deficient mice. *Proceedings of the National Academy of Sciences USA*, 94:2681–2686, March 1997.
- [3] W Alpers and H Hühnerfuss. Radar signatures of oil films floating on the sea surface and the Marangoni effect. *Journal of Geophysical Research*, 93:3642–3648, April 1988.
- [4] R M Anderson, H C Jackson, R M May, and A M Smith. Population dynamics of fox rabies in Europe. *Nature*, 289:765–771, February 1981.
- [5] R M Anderson and R M May. Population biology of infectious diseases: Part I. *Nature*, 280:361–367, August 1979.
- [6] R M Anderson and R M May. Population biology of infectious diseases: Part II. *Nature*, 280:455–461, August 1979.
- [7] R M Anderson and R M May. Directly transmitted infectious diseases: control by vaccination. *Science*, 215(4536):1053–1060, 1981.
- [8] R M Anderson and R M May. Vaccination and herd immunity to infectious diseases. *Nature*, 318:323–329, November 1985.
- [9] R M Anderson and R M May. Epidemiology parameters of HIV transmission. *Nature*, 333:514–519, 1988.

- [10] R M Anderson and R M May. Possible demographic consequences of AIDS in developing countries. *Nature*, 332:228–234, March 1988.
- [11] R M Anderson and R M May. Immunisation and herd immunity. *The Lancet*, 335(8690):641–645, March 1990.
- [12] R M Anderson and R M May. *Infectious diseases of humans*. Oxford University Press, 1991.
- [13] V Andreasen, J Lin, and S A Levin. The dynamics of cocirculating influenza strains conferring partial cross-immunity. *Journal of Mathematical Biology*, 35:825–842, 1997.
- [14] H Ankel, D F Westra, S Welling-Wester, and P Lebon. Induction of interferon-alpha by glycoprotein D of herpes simplex virus: a possible role of chemokine receptors. *Virology*, 251(2):317–326, November 1998.
- [15] R Antia, B R Levin, and R M May. Within-host population dynamics and the evolution and maintenance of microparasite virulence. *American Naturalist*, 144(3):457–472, 1994.
- [16] R Antia and M Lipsitch. Mathematical models of parasite responses to host immune defences. *Parasitology*, 115:S155–S167, 1997.
- [17] R Antia, M A Nowak, and R M Anderson. Antigenic variation and the within-host dynamics of parasites. *Proceedings of the National Academy of Sciences USA*, 93:985–989, 1996.
- [18] P Baccam, C Beauchemin, C A Macken, F G Hayden, and A S Perelson. Kinetics of Influenza A Virus Infection in Humans. *Journal of Virology*, 80(15):7590–7599, May 2006.
- [19] C T H Baker, G A Bocharov, J M Ford, P M Lumb, S J Norton, C A H Paul, T Junt, P Krebs, and B Ludewig. Computational approaches to parameter estimation and model selection in immunology. *Journal of Computational and Applied Mathematics*, 184(1):50–76, December 2005.
- [20] C Barreca. Personal communication., 2006.
- [21] C Barreca and P O'Hare. Suppression of Herpes Simplex Virus 1 in MDBK Cells via the Interferon Pathway. *Journal of Virology*, 78(16):8641–8653, August 2004.

- [22] R Barrington, M Zhang, M Fischer, and M C Carroll. The role of complement in inflammation and adaptive immunity. *Immunological Reviews*, 180:5–15, April 2001.
- [23] C Beauchemin, J Samuel, and J Tuszynski. A simple cellular automaton model for influenza A viral infections. *Journal of Theoretical Biology*, 232:223–234, 2005.
- [24] E Ben-Jacob, O Shochet, I Cohen, A Tenenbaum, A Czirok, and T Vicsek. Cooperative strategies in formation of complex bacterial patterns. *Fractals*, 4:849–868, 1995.
- [25] J M Berg, J L Tymoczko, and L Stryer. *Biochemistry*. W H Freeman, 5th edition, 2002.
- [26] D Bernoulli. Essai d'une nouvelle analyse de la mortalité causée par la petite vérole et des avantages de l'inoculation pour la prévenir. *Mémoires de Mathématiques et de Physique, Académie Royale des Sciences, Paris*, pages 1–45, 1760.
- [27] C A Biron, K B Nguyen, G C Pien, L P Cousens, and T P Salazar-Mather. Natural killer cells in antiviral defense: Function and Regulation by Innate Cytokines. *Annual Review of Immunology*, 17:189–220, April 1999.
- [28] S M Blower, D Hartel, H Dowlatabadi, R M Anderson, and R M May. Drugs, Sex and HIV: A Mathematical Model for New York City. *Philosophical Transactions of the Royal Society B: Biological Sciences*, 331:171–187, February 1991.
- [29] G Bocharov, P Klenerman, and S Ehl. Modelling the dynamics of LCMV infection in mice: II. Compartmental structure and immunopathology. *Journal of Theoretical Biology*, 221(3):349–378, April 2003.
- [30] G Bocharov, B Ludewig, A Bertoletti, P Klenerman, T Junt, P Krebs, T Luzyanina, C Fraser, and R M Anderson. Underwhelming the Immune Response: Effect of Slow Virus Growth on CD8<sup>+</sup>-T-Lymphocyte Responses. *Journal of Virology*, 78(5):2247–2254, March 2004.
- [31] G A Bocharov. Modelling the Dynamics of LCMV Infection in Mice: Conventional and Exhaustive CTL Responses. *Journal of Theoretical Biology*, 192(3):283–308, June 1998.

- [32] G A Bocharov and A A Romanyukha. Mathematical Model of Antiviral Immune Response III. Influenza A Virus Infection. *Journal of Theoretical Biology*, 167:323–360, 1994.
- [33] B S Bochner and R P Schleimer. Mast cells, basophils, and eosinophils: distinct but overlapping pathways for recruitment. *Immunological Reviews*, 179:5–15, February 2001.
- [34] S Bonhoeffer and M A Nowak. Pre-existence and emergence of drug resistance in HIV-1 infection. *Proceedings of the Royal Society B: Biological Sciences*, 264:631–637, 1997.
- [35] M F Boni, J R Gog, V Andreasen, and F B Christiansen. Influenza drift and epidemic size: the race between generating and escaping immunity. *Theoretical Population Biology*, 65:179–191, 2004.
- [36] G Brehm and H Kirchner. Analysis of the interferons induced in mice *in vivo* and in macrophages *in vitro* by Newcastle disease virus and by polyinosinic-polycytidylic acid. *Journal of Interferon Research*, 6(1):21–28, February 1986.
- [37] M Cella, M Salio, Y Sakakibara, H Langen, I Julkunen, and A Lanzavecchia. Maturation, Activation, and Protection of Dendritic Cells Induced by Double-stranded RNA. *Journal of Experimental Medicine*, 189(5):821–829, March 1999.
- [38] Z Chai, S Gatti, C Toniatti, V Poli, and T Bartfai. Interleukin (IL)-6 gene expression in the central nervous system is necessary for fever response to lipopolysaccharide or IL-1 beta: a study on IL-6-deficient mice. *Journal of Experimental Medicine*, 183:311–316, 1996.
- [39] J Chinsangaram, M P Moraes, M Koster, and M J Grubman. Novel Viral Disease Control Strategy: Adenovirus Expressing Alpha Interferon Rapidly Protects Swine from Foot-and-Mouth Disease. *Journal of Virology*, 77(2):1621–1625, January 2003.
- [40] P Cicuta and E M Terentjev. Viscoelasticity of a protein monolayer from anisotropic surface pressure measurements. *European Physical Journal E – Soft Matter*, 16:147–158, February 2005.
- [41] J M Coffin. HIV Population Dynamics *In Vivo*: Implications for Genetic Variation, Pathogenesis, and Therapy. *Science*, 267:483–489, January 1995.

- [42] D S Cohen and J D Murray. A generalized diffusion model for growth and dispersal in a population. *Journal of Mathematical Biology*, 12(2):237–249, June 1981.
- [43] R V Culshaw, S Ruan, and R J Spiteri. Optimal HIV treatment by maximising immune response. *Journal of Mathematical Biology*, October 2003.
- [44] H Dahari, M Major, X Zhang, K Mihalik, C M Rice, A S Perelson, S M Feinstone, and A U Neumann. Mathematical modeling of primary hepatitis C infection: noncytolytic clearance and early blockage of virion production. *Gastroenterology*, 128(4):1056–1066, April 2005.
- [45] J M Daly, A C Lai, M M Binns, T M Chambers, M Barrandeguy, and J A Mumford. Antigenic and genetic evolution of equine H3N8 influenza A viruses. *Journal of General Virology*, 77:661–671, 1996.
- [46] J H P Dawes and J R Gog. The onset of oscillatory dynamics in models of multiple disease strains. *Journal of Mathematical Biology*, 45(6):471–510, December 2002.
- [47] B Deal, C Farello, M Lancaster, T Kompare, and B Hannon. A dynamic model of the spatial spread of an infectious disease: the case of fox rabies in Illinois. *Environmental Modeling and Assessment*, 5(1):47–62, January 2000.
- [48] J Desmyter, J L Melnick, and W E Rawls. Defectiveness of interferon production and of rubella virus interference in a line of African green monkey kidney cells (Vero). *Journal of Virology*, 2(10):955–961, October 1968.
- [49] E Dieperink, M Willenbring, and S B Ho. Neuropsychiatric Symptoms Associated With Hepatitis C and Interferon Alpha: A Review. *American Journal of Psychiatry*, 157:867–876, June 2000.
- [50] N M Dixit, J E Layden-Almer, T J Layden, and A S Perelson. Modelling how ribavirin improves interferon response rates in hepatitis C virus infection. *Nature*, 432:922–924, December 2004.
- [51] R Durrett. Stochastic Spatial Models. *SIAM Review*, 41(4):677–718, 1999.
- [52] R Durrett and S Levin. The Importance of Being Discrete (and Spatial). *Theoretical Population Biology*, 46:363–394, 1994.
- [53] R Durrett and S A Levin. Stochastic spatial models: a user's guide to ecological applications. *Philosophical Transactions of the Royal Society B: Biological Sciences*, 343:329–350, 1994.

- [54] C Dye, S Scheele, P Dolin, V Pathania, and M C Raviglione. Consensus statement. Global burden of tuberculosis: estimated incidence, prevalence, and mortality by country. WHO Global Surveillance and Monitoring Project. *Journal of the American Medical Association*, 282(7):677–686, August 1999.
- [55] G Elliott and P O'Hare. Live-Cell Analysis of a Green Fluorescent Protein-Tagged Herpes Simplex Virus Infection. *Journal of Virology*, 73(5):4110–4119, May 1999.
- [56] J M Emeny and M J Morgan. Regulation of the interferon system: evidence that Vero cells have a genetic defect in interferon production. *Journal of General Virology*, 43(1):247–252, April 1979.
- [57] P Essunger and A S Perelson. Modeling of HIV infection of CD4<sup>+</sup> T-cell subpopulations. *Journal of Theoretical Biology*, 170:367–391, 1994.
- [58] J Fan, C Zhang, and J Zhang. Generalized Likelihood Ratio Statistics and Wilks Phenomenon. *Annals of Statistics*, 29(1):153–193, 2001.
- [59] X Fanton and A M Cazabat. Spreading and Instabilities Induced by a Solutal Marangoni Effect. *Langmuir*, 14(9):2554–2561, April 1998.
- [60] J J Ferbas, J F Toso, A J Logar, J S Navratil, and C R Rinaldo Jr. CD4<sup>+</sup> blood dendritic cells are potent producers of IFN-alpha in response to *in vitro* HIV-1 infection. *Journal of Immunology*, 152(9):4649–4662, 1994.
- [61] N Ferguson and V Andreasen. *Mathematical Approaches for Emerging and Reemerging Infections: Models, Methods and Theory. IMA Volumes in Mathematics and its Applications*, chapter The influence of different forms of cross-protective immunity on the population dynamics of antigenically diverse pathogens, pages 157–169. Springer, New York, 1999.
- [62] N M Ferguson, F deWolf, A C Ghani, C Fraser, C A Donnelly, P Reiss, J M A Lange, S A Danner, G P Garnett, J Goudsmit, and R M Anderson. Antigen-drive CD4<sup>+</sup> T cell and HIV-1 dynamics: Residual viral replication under highly active antiretroviral therapy. *Proceedings of the National Academy of Sciences USA*, 96(26):15167–15172, December 1999.
- [63] N M Ferguson and G P Garnett. More Realistic Models of Sexually Transmitted Disease Transmission Dynamics: Sexual Partnership Networks, Pair Models, and Moment Closure. *Sexually Transmitted Diseases*, 27(10):600–609, November 2000.

- [64] R A Fisher. *Statistical Methods, Experimental Design, and Scientific Inference*. Oxford Science Publications, 1990.
- [65] M Frame and B B Mandelbrot. A Panorama of Fractals and Their Uses. <http://classes.yale.edu/fractals/Panorama/Biology/Bacteria/Bacteria.html> (accessed 2006-08-07).
- [66] F Franks. *Water: A Matrix of Life*. Royal Society of Chemistry, 2nd edition, 2000.
- [67] S D W Frost, M Dumaurier, S Wain-Hobson, and A J Leigh Brown. Genetic drift and within-host metapopulation dynamics of HIV-1 infection. *Proceedings of the National Academy of Sciences USA*, 98(12):6975–6980, June 2001.
- [68] H Fujikawa and M Matsushita. Bacterial Fractal Growth in the Concentration Field of Nutrient. *Journal of the Physical Society of Japan*, 60(1):88–94, January 1991.
- [69] G A Funk, V A A Jansen, S Bonhoeffer, and T Killingback. Spatial models of virus-immune dynamics. *Journal of Theoretical Biology*, 223:221–236, 2005.
- [70] D Furlong, H Swift, and B Roizman. Arrangement of herpes-virus deoxyribonucleic acid in the core. *Journal of Virology*, 10:1071–1074, 1972.
- [71] V V Ganusov, C T Bergstrom, and R Antia. Within-host population dynamics and the evolution of microparasites in a heterogeneous host population. *Evolution*, 56:213–223, 2002.
- [72] R A Gatenby and E T Gawlinski. A reaction-diffusion model of cancer invasion. *Cancer Research*, 56(24):5745–5753, 1996.
- [73] C R Gauth, W L Hard, and T F Smith. Characterization of an established line of canine kidney cells (MDCK). *Proceedings of the Society of Experimental Biology and Medicine*, 122:931–935, 1966.
- [74] R B Gennis. *Biomembranes: Molecular Structure and Function*. Springer-Verlag, 1989.
- [75] A V Getling, editor. *Rayleigh-Benard Convection: Structure and Dynamics*. World Scientific Publishing, December 1996.

- [76] M A Gilchrist, D Coombs, and A S Perelson. Optimizing within-host viral fitness: infected cell lifespan and virion production rate. *Journal of Theoretical Biology*, 229:281–288, April 2004.
- [77] J R Gog and B T Grenfell. Dynamics and selection of many-strain pathogens. *Proceedings of the National Academy of Sciences USA*, 99(2):17209–17214, December 2002.
- [78] J R Gog, G F Rimmelzwaan, A D M E Osterhaus, and B T Grenfell. Population Dynamics of Rapid Fixation in CTL Escape Mutants of Influenza A. *Proceedings of the National Academy of Sciences USA*, 100(19):11143–11147, September 2003.
- [79] J R Gog and J Swinton. A status-based approach to multiple strain dynamics. *Journal of Mathematical Biology*, 44:169–184, February 2002.
- [80] S Goodbourn, L Didcock, and R E Randall. Interferons: cell signalling, immune modulation, antiviral responses and virus countermeasures. *Journal of General Virology*, 81:2341–2364, 2000.
- [81] A M Gosselin and G P Biro. The cardiovascular effects of the surfactant pluronic F68 in anesthetized dogs. *Advances in Experimental Medicine and Biology*, 227:291–299, 1990.
- [82] B T Grenfell, O N Bjørnstad, and J Kappey. Travelling waves and spatial hierarchies in measles epidemics. *Nature*, 414:716–723, December 2001.
- [83] S Gupta, N Ferguson, and R Anderson. Chaos, Persistence, and Evolution of Strain Structure in Antigenically Diverse Infectious Agents. *Science*, 280:912–915, May 1998.
- [84] S Gupta and A V S Hill. Dynamic interactions in malaria: host heterogeneity meets parasite polymorphism. *Proceedings of the Royal Society B: Biological Sciences*, 261:271–277, 1995.
- [85] W H Hamer. Epidemic disease in England. *The Lancet*, 1:733–739, 1906.
- [86] R B Hamilton. *From horse to herd: Linking within-host and population level epidemic dynamics*. PhD thesis, University of Cambridge, December 2002.
- [87] P Härle, B Sainz Jr, D J J Carr, and W P Halford. The Immediate-Early Protein, ICP0, Is Essential for the Resistance of Herpes Simplex Virus to Interferon- $\alpha/\beta$ . *Virology*, 293(2):295–304, 2002.

- [88] I M Hastings. A model for the origins and spread of drug-resistant malaria. *Parasitology*, 115:133–141, 1997.
- [89] A J Hay, V Gregory, A R Douglas, and Y P Lin. The evolution of human influenza viruses. *Philosophical Transactions of the Royal Society B: Biological Sciences*, 356:1861–1870, 2001.
- [90] F G Hayden, R S Fritz, M C Lobo, W G Alvord, W Strober, and S E Straus. Local and Systemic Cytokine Responses during Experimental Human Influenza A Virus Infection – Relation to Symptom Formation and Host Defense. *Journal of Clinical Investigation*, 101(3):643–649, February 1998.
- [91] A Hayman, S Comely, A Lackenby, S Murphy, J McCauley, S Goodbourn, and W Barclay. Variation in the ability of human influenza A viruses to induce and inhibit the IFN- $\beta$  pathway. *Virology*, 347:52–64, March 2006.
- [92] E Herrmann, J Lee, G Marinos, M Modi, and S Zeuzem. Effect of ribavirin on hepatitis C viral kinetics in patients treated with pegylated interferon. *Hepatology*, 37(6):1351–1358, December 2003.
- [93] A V M Herz, S Bonhoeffer, R M Anderson, R M May, and M A Nowak. Viral dynamics *in vivo*: Limitations on estimates of intracellular delay and virus decay. *Proceedings of the National Academy of Sciences USA*, 93(14):7247–7251, July 1996.
- [94] H W Hethcote. The Mathematics of Infectious Diseases. *SIAM Review*, 42(4), 2000.
- [95] C Hetzel and R M Anderson. The within-host cellular dynamics of bloodstage malaria: theoretical and experimental studies. *Parasitology*, 113(1):25–38, July 1996.
- [96] W S Hlavacek, C Wofsy, and A S Perelson. Dissociation of HIV-1 from follicular dendritic cells during HAART: Mathematical analysis. *Proceedings of the National Academy of Sciences USA*, 96(2):14681–14686, 1999.
- [97] D Hober, L Poli, B Roblin, P Gestas, E Chungue, G Granic, P Imbert JL Pecarere, R Vergez-Pascal, and P Wattre. Serum levels of tumor necrosis factor-alpha (TNF-alpha), interleukin-6 (IL-6), and interleukin-1 beta (IL-1 beta) in dengue-infected patients. *American Journal of Tropical Medicine and Hygiene*, 48(3):324–331, March 1993.

- [98] M B Hoshen, R Heinrich, W D Stein, and H Ginsburg. Mathematical modelling of the within-host dynamics of *Plasmodium falciparum*. *Parasitology*, 121:227–235, 2000.
- [99] A J Howat, A R Campbell, and D J Stewart. Generalized lymphadenopathy due to herpes simplex virus type I. *Histopathology*, 19(6):563–564, 1991.
- [100] T J Howat, C Barreca, P O'Hare, J Gog, and B T Grenfell. Modelling dynamics of the Type I Interferon response to *in vitro* viral infection. *Journal of the Royal Society Interface*, 3(10):699–709, October 2006.
- [101] S Hoyas, H Herrero, and A M Mancho. Thermal convection in a cylindrical annulus heated laterally. *Journal of Physics A: Mathematical and General*, 35:4067–4083, April 2002.
- [102] A Isaacs and J Lindenmann. Virus interference. I. The inteferon. *Proceedings of the Royal Society B: Biological Sciences*, 147:258–267, September 1957.
- [103] A Isaacs and J Lindenmann. Virus interference. II. Some properties of interferon. *Proceedings of the Royal Society B: Biological Sciences*, 147:268–279, September 1957.
- [104] V Isham. Mathematical Modelling of the Transmission Dynamics of HIV and Aids: a Review. *Journal of the Royal Statistical Society*, 151(1):5–30, 1988.
- [105] B L Jacobs and J O Langland. When Two Strands Are Better Than One: The Mediators and Modulators of the Cellular Responses to Double-Stranded RNA. *Virology*, 219:339–349, 1996.
- [106] C A Janeway, P Travers, M Walport, and M Shlomchik. *Immunobiology*. Garland, New York, 6th edition, 2005.
- [107] H L Janssen, J T Brouwer, R C van der Mast, and S W Schalm. Suicide associated with alfa-interferon therapy for chronic viral hepatitis. *Journal of Hepatology*, 21(2):241–243, August 1994.
- [108] A Juel, J M Burgess, W D McCormick, J B Swift, and Harry L Swinney. Surface tension-driven convection patterns in two liquid layers. *Physica D: Nonlinear Phenomena*, 143:169–186, 2000.
- [109] N Kadowaki, S Antonenko, J Yiu-Nam Lau, and Y Liu. Natural Interferon  $\alpha/\beta$ -producing Cells Link Innate and Adaptive Immunity. *Journal of Experimental Medicine*, 192(2):219–226, July 2000.

- [110] A Kallen, P Arcuri, and J D Murray. A simple model for the spatial spread and control of rabies. *Journal of Theoretical Biology*, 116(3):377–393, October 1985.
- [111] D V Kalvakolanu and E C Borden. An overview of the interferon system: signal transduction and mechanisms of action. *Cancer Investigation*, 14(1):25–53, 1996.
- [112] M J Keeling, M E J Woolhouse, D J Shaw, L Matthews, M Chase-Topping, D T Haydon, S J Cornell, J Kappey, J Wilesmith, and B T Grenfell. Dynamics of the 2001 UK Foot and Mouth Epidemic: Stochastic Dispersal in a Heterogeneous Landscape. *Science*, 294(5543):813–817, October 2001.
- [113] D Kirschner. Dynamics of Co-infection with *M. tuberculosis* and HIV-1. *Theoretical Population Biology*, 55:94–109, 1999.
- [114] D Kirschner and S Marino. Mycobacterium tuberculosis as viewed through a computer. *Trends in Microbiology*, 13(5):206–211, May 2005.
- [115] P Klenerman, R E Phillips, C R Rinaldo, L M Wahl, G Ogg, R M May, A J McMichael, and M A Nowak. Cytotoxic T lymphocytes and viral turnover in HIV type 1 infection. *Proceedings of the National Academy of Sciences USA*, 93:15323–15328, 1996.
- [116] J C Koella. On the use of mathematical models of malaria transmission. *Acta Tropica*, 49(1):1–25, April 1991.
- [117] J Kreft, G Booth, and J W T Wimpenny. BacSim, a simulator for individual-based modelling of bacterial colony growth. *Microbiology*, 144:3275–3287, 1998.
- [118] A Krug, G D Luker, W Barchet, D A Leib, S Akira, and M Colonna. Herpes simplex virus type 1 activates murine natural interferon-producing cells through toll-like receptor 9. *Blood*, 103(4):1433–1437, February 2004.
- [119] J O Langland, J M Cameron, M C Heck, J K Jancovich, and B L Jacobs. Inhibition of PKR by RNA and DNA viruses. *Virus Research*, 119(1):100–110, July 2006.
- [120] E W Larson, J W Dominik, A H Rowberg, and G A Higbee. Influenza Virus Population Dynamics in the Respiratory Tract of Experimentally Infected Mice. *Infection and Immunity*, 13(2):438–447, February 1976.

- [121] M Law, R Hollinshead, and G L Smith. Antibody-sensitive and antibody-resistant cell-to-cell spread by vaccinia virus: role of the A33R protein in antibody-resistant spread. *Journal of General Virology*, 83:209–222, 2002.
- [122] S H Lee and S M Vidal. Functional Diversity of Mx Proteins: Variations on a Theme of Host Resistance to Infection. *Genome Research*, 12(4):527–530, April 2002.
- [123] D A Leib. Counteraction of interferon-induced antiviral responses by herpes simplex viruses. *Current Topics in Microbiology and Immunology*, 269:171–185, 2002.
- [124] J Lin, V Andreasen, and S A Levin. Dynamics of influenza A drift: the linear three-strain model. *Mathematical Biosciences*, 162:33–51, 1999.
- [125] T Lipniacki, P Paszek, A R Brasier, B Luxon, and M Kimmel. Mathematical model of NF- $\kappa$ B regulatory module. *Journal of Theoretical Biology*, 228:195–215, 2004.
- [126] A D Luster. The role of chemokines in linking innate and adaptive immunity. *Current Opinion in Immunology*, 14(1):129–135, February 2002.
- [127] G I Marchuk, R V Petrov, A A Romanyukha, and G A Bocharov. Mathematical model of antiviral immune response. I. Data analysis, generalized picture construction and parameters evaluation for hepatitis B. *Journal of Theoretical Biology*, 151(1):1–40, July 1991.
- [128] G I Marchuk, A A Romanyukha, and G A Bocharov. Mathematical model of antiviral immune response. II. Parameters identification for acute viral hepatitis B. *Journal of Theoretical Biology*, 151(1):41–69, July 1991.
- [129] M Matsumoto and T Nishimura. Mersenne Twister: A 623-Dimensionally Equidistributed Uniform Pseudo-Random Number Generator. *ACM Transactions on Modeling and Computer Simulation*, 8(1):3–30, January 1998.
- [130] M Matsushita, J Wakita, H Itoh, I Ràfols, T Matsuyama, H Sakaguchi, and M Mimura. Interface growth and pattern formation in bacterial colonies. *Physica A: Statistical and Theoretical Physics*, pages 517–524, February 1998.
- [131] R M May and R M Anderson. Spatial heterogeneity and the design of immunization programs. *Mathematical Biosciences*, 72(1):83–111, 1984.

- [132] D J McGeoch, M A Dalrymple, A J Davidson, A Dolan, M C Frame, D McNab, L J Perry, J E Scott, and P Taylor. The complete DNA sequence of the long unique region in the genome of herpes simplex virus type 1. *Journal of General Virology*, 69:1531–1574, 1988.
- [133] F E McKenzie. Why Model Malaria? *Parasitology Today*, 16(12):511–516, December 2000.
- [134] F E McKenzie and W H Bossert. The Dynamics of Plasmodium falciparum Blood-stage Infection. *Journal of Theoretical Biology*, 188(1):127–140, September 1997.
- [135] F Ellis McKenzie and E M Samba. The role of mathematical modeling in evidence-based malaria control. *American Journal of Tropical Medicine and Hygiene*, 71(2 suppl):94–96, 2004.
- [136] A R McLean and T L B Kirkwood. A model of human immunodeficiency virus (HIV) infection in T-helper cell clones. *Journal of Theoretical Biology*, 147:177–203, 1990.
- [137] A R McLean and M A Nowak. Competition between zidovudine-sensitive and zidovudine-resistant strains of HIV. *AIDS*, 6(1):71–79, 1992.
- [138] A R McLean and M A Nowak. Models of interactions between HIV and other pathogens. *Journal of Theoretical Biology*, 155:69–86, 1992.
- [139] P G McQueen and F Ellis McKenzie. Age-structured red blood cell susceptibility and the dynamics of malaria infections. *Proceedings of the National Academy of Sciences USA*, 101(24):9161–9166, 2004.
- [140] R Medzhitov and C Janeway. Innate Immunity. *New England Journal of Medicine*, 343(5):338–344, August 2000.
- [141] R Medzhitov and C A Janeway. Innate immunity: impact on the adaptive immune response. *Current Opinion in Immunology*, 9:4–9, 1997.
- [142] R Medzhitov and C A Janeway. Innate Immunity: The Virtues of a Nonclonal System of Recognition. *Cell*, 91:295–298, October 1997.
- [143] Y A Mekori and D D Metcalfe. Mast cells in innate immunity. *Immunological Reviews*, 173:131–140, February 2000.
- [144] I Mellman and R M Steinman. Dendritic cells: specialized and regulated antigen processing machines. *Cell*, 106(3):255–258, August 2001.

- [145] D Mollison. Spatial Contact Models for Ecological and Epidemic Spread. *Journal of the Royal Statistical Society B*, 39(3):283–326, 1977.
- [146] R Monti, R Savino, and S Tempesta. Wetting prevention by thermal Marangoni effect. Experimental and numerical simulation. *European Journal of Mechanics – B/Fluids*, 17(1):51–77, January 1998.
- [147] M P Moraes, J Chinsangaram, M C S Brum, and M J Grubman. Immediate protection of swine from foot-and-mouth disease: a combination of adenoviruses expressing interferon alpha and a foot-and-mouth disease virus subunit vaccine. *Vaccine*, 22:268–279, 2003.
- [148] K L Mossman, H A Saffran, and J R Smiley. Herpes Simplex Virus ICP0 Mutants Are Hypersensitive to Interferon. *Journal of Virology*, 74(4):2052–2056, 2000.
- [149] K Mukai. Wetting and Marangoni Effect in Iron and Steelmaking Processes. *ISIJ International*, 32(1):19–25, January 1992.
- [150] J Müller and T Tjardes. Modeling the Cytokine Network In Vitro and In Vivo. *Journal of Theoretical Medicine*, 5(2):93–110, June 2003.
- [151] J D Murray. *Mathematical Biology*. Springer-Verlag, 1989.
- [152] K C Nadeau, H Azuma, and N L Tilney. Sequential cytokine dynamics in chronic rejection of rat renal allografts: Roles for cytokines RANTES and MCP-1. *Proceedings of the National Academy of Sciences USA*, 92:8729–8733, September 1995.
- [153] T Nagai and H Honda. A dynamic cell model for the formation of epithelial tissues. *Philosophical Magazine B*, 81(7):699–719, 2001.
- [154] J A Nelder and R Mead. A simplex method for function minimization. *The Computer Journal*, 7(4):308–313, 1965.
- [155] A U Neumann, N P Lam, H Dahari, D R Gretch, T E Wiley, T J Layden, and A S Perelson. Hepatitis C Viral Dynamics in Vivo and the Antiviral Efficacy of Interferon- $\alpha$  Therapy. *Science*, 282:103–107, October 1998.
- [156] P Newmark. Engineered E. coli produce interferon. *Nature*, 283(5745):323, January 1980.

- [157] M A Nowak, S Bonhoeffer, G M Shaw, and R M May. Anti-viral drug treatment: Dynamics of resistance in free virus and infected cell populations. *Journal of Theoretical Biology*, 184:205–219, 1997.
- [158] M A Nowak and R M May. Mathematical biology of HIV infections: Antigenic variation and diversity threshold. *Mathematical Biosciences*, 106:1–21, 1991.
- [159] M A Nowak and R M May. *Virus Dynamics: Mathematical Principles of Immunology and Virology*. Oxford University Press, 2000.
- [160] P O'Hare. Personal communication., 2004.
- [161] P O'Hare. Personal communication., 2006.
- [162] World Health Organization. <http://www.who.int/mediacentre/factsheets/2003/fs211/en/> (accessed 2006-08-07), April 2002.
- [163] J M Pacheco, M C S Brum, M P Moraes, W T Golde, and M J Grubman. Rapid protection of cattle from direct challenge with foot-and-mouth disease virus (FMDV) by a single inoculation with an adenovirus-vectored FMDV subunit vaccine. *Virology*, 337(2):205–209, July 2005.
- [164] G Parnaud, S Tache, G Peiffer, and D E Corpet. Pluronic F68 block polymer, a very potent suppressor of carcinogenesis in the colon of rats and mice. *British Journal of Cancer*, 84(1):90–93, January 2001.
- [165] D W Paty and D K Li. Interferon beta-1b is effective in relapsing-remitting multiple sclerosis. *Neurology*, 43(4):655–667, 1993.
- [166] A S Perelson. Immune network theory. *Immunological Reviews*, 110:5–36, August 1989.
- [167] A S Perelson. Modelling viral and immune system dynamics. *Nature Reviews Immunology*, 2(1):28–36, January 2002.
- [168] A S Perelson, P Essunger, Y Cao, M Vesanen, A Hurley, K Saksela, M Markowitz, and D D Ho. Decay characteristics of HIV-1-infected compartments during combination therapy. *Nature*, 387:188–191, May 1997.
- [169] A S Perelson, D E Kirschner, and R De Boer. Dynamics of HIV infection of CD4<sup>+</sup> T cells. *Mathematical Biosciences*, 114:81–125, 1993.
- [170] A S Perelson and P W Nelson. Mathematical Analysis of HIV-1 Dynamics in Vivo. *SIAM Review*, 41(1):3–44, January 1999.

- [171] A S Perelson, A U Neumann, M Markowitz, J M Leonard, and D D Ho. HIV-1 Dynamics in Vivo: Virion Clearance Rate, Infected Cell Life-Span, and Viral Generation Time. *Science*, 271:1582–1586, March 1996.
- [172] J B Plotkin and J Dushoff. Codon bias and frequency-dependent selection on the hemagglutinin epitopes of influenza A virus. *Proceedings of the National Academy of Sciences USA*, 100(12):7152–7157, June 2003.
- [173] W H Press, S A Teukolsky, W T Vetterling, and B P Flannery. *Numerical Recipes in C*. Cambridge University Press, 1992.
- [174] C L Raison, A S Borisov, S D Broadwell, L Capuron, B J Woolwine, I M Jacobson, C B Nemeroff, and A H Miller. Depression during pegylated interferon-alpha plus ribavirin therapy: prevalence and prediction. *Journal of Clinical Psychiatry*, 66(1):41–48, January 2005.
- [175] M L Ramón, D Maza, and H L Mancini. Patterns in small aspect ratio Bénard-Marangoni convection. *Physical Review E: Statistical, Nonlinear, and Soft Matter Physics*, 60(4):4193–4198, 1999.
- [176] R Rampling, G Cruickshank, V Papanastassiou, J Nicoll, D Hadley, D Brennan, R Petty, A MacLean, J Harland, E McKie, R Mabbs, and M Brown. Toxicity evaluation of replication-competent herpes simplex virus (ICP 34.5 null mutant 1716) in patients with recurrent malignant glioma. *Gene Therapy*, 7:859–866, 2000.
- [177] J S Rhim, K Schell, B Creasy, and W Case. Biological characteristics and viral susceptibility of an African green monkey kidney cell line (Vero). *Proceedings of the Society of Experimental Biology and Medicine*, 132(2):670–678, November 1969.
- [178] B Roizman, L E Carmichael, F Deinhardt, G de The, A J Nahmias, W Plowright, F Rapp, P Sheldrick, M Takahashi, and K Wolf. Herpesviridae: definition, provisional nomenclature and taxonomy. *Intervirology*, 16:201–217, 1981.
- [179] B Roizman and A E Sears. *Fundamental Virology*, chapter Herpes Simplex Viruses and Their Replication. Lippincott-Raven Publishers, Philadelphia, 1996.
- [180] R L Roper, E J Wolffe, A Weisberg, and B Moss. The Envelope Protein Encoded by the A33R Gene Is Required for Formation of Actin-Containing

Microvilli and Efficient Cell-to-Cell Spread of Vaccinia Virus. *Journal of Virology*, 72(5):4192–4204, May 1998.

- [181] R A Rudick, D E Goodkin, L D Jacobs, D L Cookfair, R M Herndon, J R Richert, A M Salazar, J S Fischer, C V Granger, J H Simon, J J Alam, N A Simonian, M K Champion, D M Bartoszak, D N Bourdette, J Braiman, C M Brownschidle, M E Coats, S L Cohan, D S Dougherty, R P Kinkel, M K Mass, F E Munschauer, R L Priore, and R H Whitham. Impact of interferon beta-1a on neurologic disability in relapsing multiple sclerosis. The Multiple Sclerosis Collaborative Research Group (MSCRG). *Neurology*, 49(2):358–363, 1997.
- [182] C E Samuel. Antiviral actions of interferon. Interferon-regulated cellular proteins and their surprisingly selective antiviral activities. *Virology*, 183(1):1–11, July 1991.
- [183] C M Sanderson, M Way, and G L Smith. Virus-Induced Cell Motility. *Journal of Virology*, 72(2):1235–1243, February 1998.
- [184] K E Schneeweiss. Serologische Untersuchungen zur Typendifferenzierung des Herpesvirus hominis. *Z. Immuno-Forsch.*, 124:24–28, 1962.
- [185] L A Segel and R Lev Bar-Or. On the role of feedback in promoting conflicting goals of the adaptive immune system. *Journal of Immunology*, 163:1342–1349, 1999.
- [186] J A Simpson, L Aarons, W E Collins, G M Jeffery, and N J White. Population dynamics of untreated *Plasmodium falciparum* malaria within the adult human host during the expansion phase of the infection. *Parasitology*, 124:247–263, 2002.
- [187] D J Smith, A S Lapedes, J C de Jong, T M Bestebroer, G F Rimmelzwaan, A D M E Osterhaus, and R A M Fouchier. Mapping the Antigenic and Genetic Evolution of Influenza Virus. *Science*, 2004.
- [188] D L Smith, B Lucey, L A Waller, J E Childs, and L A Real. Predicting the spatial dynamics of rabies epidemics on heterogeneous landscapes. *Proceedings of the National Academy of Sciences USA*, 99(6):3668–3672, March 2002.
- [189] D L Smith and F Ellis McKenzie. Statics and dynamics of malaria infection in *Anopheles* mosquitoes. *Malaria Journal*, 3(13):1–14, 2004.
- [190] G L Smith, A Vanderplassen, and M Law. The formation and function of extracellular enveloped vaccinia virus. *Journal of General Virology*, 83(12):2915–2931, 2002.

- [191] S Sockalingam and K Balderson. Major depressive episode with psychotic features induced by pegylated interferon-alpha-2b and ribavirin treatment. *International Clinical Psychopharmacology*, 20(5):289–290, September 2005.
- [192] G R Stark, I M Kerr, B R G Williams, R H Silverman, and R D Schreiber. How cells respond to interferons. *Annual Reviews of Biochemistry*, 67:227–264, July 1998.
- [193] R Sumpter Jr., C Wang, E Foy, Y Loo, and M Gale Jr. Viral Evolution and Interferon Resistance of Hepatitis C Virus RNA Replication in a Cell Culture Model. *Journal of Virology*, 78(21):11591–11604, November 2004.
- [194] C Svanborg, G Godaly, and M Hedlund. Cytokine responses during mucosal infections: role in disease pathogenesis and host defence. *Current Opinion in Microbiology*, 2(1):99–103, 1999.
- [195] H R Thieme. A model for the spatial spread of an epidemic. *Journal of Mathematical Biology*, 4(4):337–351, 1977.
- [196] J Thomson. On certain curious motions observable on the surfaces of wine and other alcoholic liquours. *Philosophical Magazine*, 10:330, 1855.
- [197] K To, P K S Chan, K Chan, W Lee, W Lam, K Wong, N L S Tang, D N C Tsang, R Y T Sung, T A Buckley, J S Tam, and A F Cheng. Pathology of Fatal Human Infection Associated With Avian Influenza A H5N1 Virus. *Journal of Medical Virology*, 63:242–246, 2001.
- [198] M Tognon, D Furlong, A J Conley, and B Roizman. Molecular genetics of herpes simplex virus. V. Characterization of a mutant defective in ability to form plaques at low temperatures and in a viral function which prevents accumulation of coreless capsids at nuclear pores late in infection. *Journal of Virology*, 40:870–880, 1981.
- [199] E H Tran, E N Prince, and T Owens. IFN- $\gamma$  Shapes Immune Invasion of the Central Nervous System Via Regulation of Chemokines. *Journal of Immunology*, 164:2759–2768, 2000.
- [200] W Tsai and D K P Yue. Numerical calculation of nonlinear axisymmetric standing waves in a circular basin. *Physical Fluids*, 30(11):3441–3447, November 1987.
- [201] F Uno. Scanning Immunoelectron Microscopy of Antigenic Alterations of MDCK Cells after Infection with Influenza Virus. *Journal of Electron Microscopy*, 28(2):83–92, 1979.

- [202] X Wang, M Li, H Zheng, T Muster, P Palese, A A Beg, and A García-Sastre. Influenza A Virus NS1 Protein Prevents Activation of NF- $\kappa$ B and Induction of Alpha/Beta Interferon. *Journal of Virology*, 74(24):11566–11573, 2000.
- [203] S Watts. *Epidemics and History: Disease, Power and Imperialism*. Yale University Press, 1997.
- [204] M Wilson, R Seymour, and B Henderson. Bacterial perturbation of cytokine networks. *Infection and Immunology*, 66:2401–2409, 1998.
- [205] D Wodarz and M A Nowak. Evolutionary dynamics of HIV-induced subversion of the immune response. *Immunological Reviews*, 168:75–89, April 1999.
- [206] D Wodarz and M A Nowak. Mathematical models of HIV pathogenesis and treatment. *BioEssays*, 24(12):1178–1187, November 2002.
- [207] M Wolfelschneider, M Schreiber, S Holthausen-Markou, U Gieler, and B Brosig. Psychological side effects during interferon-alpha therapy – a case study. *Psychiatrische Praxis*, 33(2):88–92, March 2006.
- [208] Wolfram Research, Inc. Mathematica 5.0, 2003.
- [209] J Wood. Personal communication., 2006.
- [210] H Wu, Y Huang, E P Acosta, S L Rosenkranz, D R Kuritzkes, J J Eron, A S Perelson, and J G Gerber. Modeling Long-Term HIV Dynamics and Antiretroviral Response: Effects of Drug Potency, Pharmacokinetics, Adherence, and Drug Resistance. *Journal of Acquired Immune Deficiency Syndromes*, 39(3):272–283, July 2005.
- [211] J Wu, Q Ruan, and H Y P Lam. Effects of surface-active medium additives on insect cell surface hydrophobicity relating to cell protection against bubble damage. *Enzyme and Microbial Technology*, 21(5):341–348, 1997.
- [212] A Yates, R Callard, and J Stark. Combining cytokine signalling with T-bet and GATA-3 regulation in Th1 and Th2 differentiation: a model for cellular decision-making. *Journal of Theoretical Biology*, 231(2):181–196, November 2004.
- [213] A Yates, C C W Chan, R E Callard, A J T George, and J Stark. An approach to modelling in immunology. *Briefings in Bioinformatics*, 2(3):245–257, September 2001.

- [214] W K Yung, M Prados, V A Levin, M R Fetell, J Bennett, M S Mahaley, M Salcman, and E Etcubanas. Intravenous recombinant interferon beta in patients with recurrent malignant gliomas: a phase I/II study. *Journal of Clinical Oncology*, 9:1945-1949, 1991.